2/12/91
E5955

NASA Technical Memorandum 103724

Low-Density, High-Strength Intermetallic Matrix Composites by XD^{TM} Synthesis

K.S. Kumar, M.S. DiPietro, and S.A. Brown
Martin Marietta Corporation
Baltimore, Maryland

and

J.D. Whittenberger
Lewis Research Center
Cleveland, Ohio

January 1991

NASA

CONTENTS

LOW-DENSITY, HIGH STRENGTH INTERMETALLIC MATRIX COMPOSITES BY XD™ SYNTHESIS

K.S. Kumar, M.S. DiPietro, and S.A. Brown
Martin Marietta Corporation
Baltimore, Maryland 21227

and

J.D. Whittenberger
National Aeronautics and Space Administration
Lewis Research Center
Cleveland, Ohio 44135

I. INTRODUCTION

There is an increasing need for lightweight high-performance materials in today's aerospace arena. High-temperature engine designs, for example, require engine materials with elevated-temperature strength, creep resistance, damage tolerance, oxidation resistance, and low density. Ordered intermetallics are considered potential alternatives to superalloys because they exhibit many of these properties.

A major problem with most ordered alloys is their tendency toward inherently low ductility. The reasons can be quite varied depending on the alloy system, and include poor grain-boundary cohesion, an insufficient number of available slip systems (primarily in non-cubic alloys), limited cross slip, and impurity locking of dislocations. However, intermetallics of high symmetry, such as the $L1_2$ structure, have a number of slip systems, which can provide some plasticity, at least at intermediate temperatures, thus enabling the matrix to accommodate some of the strain associated with the thermal stresses.

Intermetallic matrix composites (IMC) represent a class of materials that are suitable for high-temperature use and have potential for low-temperature damage resistance, features that can be exploited for advanced engine materials. A key element in designing an IMC for a particular application is tailoring the reinforcement and matrix to achieve both chemical compatibility and an acceptable thermal expansion coefficient mismatch. Compatibility is critical in the case of high-temperature materials because, at the projected use temperatures, the kinetics of possible reactions are extremely fast and can lead to severe reinforcement degradation. Similarly, the temperature range over which the materials are likely to be cycled is so large that differences in the thermal expansion coefficients between the reinforcement and matrix can lead to very large stresses, which often cause cracking.

Martin Marietta's patented approach to producing metal and intermetallic matrix composites, referred to as XD™ Technology, is an in situ precipitation technique which forms a discontinuous reinforcement directly in the matrix. XD™ Technology makes it possible to introduce a wide range of reinforcements in a given matrix, and, thereby, permits the design of the microstructure to meet a specific material need (e.g., fine particles for strength and/or whiskers for creep reduction).

In the program discussed here, we used XD™ Technology to reinforce the $L1_2$ intermetallics $Al_{22}Fe_3Ti_8$, $Al_{66}Mn_9Ti_{25}$, and $Al_{67}Cr_8Ti_{25}$ (tau) with TiB_2 particulates, and conducted a 1-year feasibility effort to identify the range of use temperatures for various reinforcement volume fractions. These ternary trialuminides are part of a particularly attractive family of $L1_2$ intermetallics, based on density and high-temperature strength. Our study included measurements of the mechanical properties of compressive yield, three-point bending, biaxial flexure, elastic modulus, and coefficient of thermal expansion (CTE) (courtesy of Dr. M. Nathal) as a function of temperature, as well as high-temperature compression creep tests Sufficient powders of the monolithic intermetallic and the composites were made available to NASA, Lewis Research Center, for preliminary fiber-reinforced composite studies.

II. LITERATURE REVIEW

A. $L1_2$ TRIALUMINIDES

The new class of ternary, aluminum-rich $L1_2$ compounds of interest includes $A1_{22}Fe_3Ti_8$, $Al_{67}Ni_8Ti_{25}$, Al_5CuTi_2, $Al_{66}Mn_9Ti_{25}$, and $Al_{67}Cr_8Ti_{25}$. The variation in compressive yield strength with temperature of polycrystals of some of these compounds has been reported.(1-4) Kumar and Pickens (1) showed a mild positive temperature dependence of strength for $Al_{22}Fe_3Ti_8$, with the peak strength occurring at ~700K. A bottom temperature, similar to that observed in Co_3Ti, (5,6) was also observed in $Al_{22}Fe_3Ti_8$ at ~400K. Below ambient temperature, the yield strength increased gradually with temperature. The substitution of 2 at.% V for Ti in this compound significantly influenced the warm-temperature strength without affecting strength at low temperatures.(1) Likewise, Winnicka and Varin (2) reported a positive temperature dependence of compressive yield strength for Al_5CuTi_2 although they performed no tests at cryogenic temperatures in their study.

A plot of compressive yield strength versus temperature for the compound $Al_{67}Cr_8Ti_{25}$, developed by Mabuchi et al., (3) showed bottom and peak temperatures at ~650K and ~925K, respectively, similar to those found for $Al_{22}Fe_3Ti_8$.(1) The authors, however, reported the density of the hot-pressed specimens as ~93%. It is not clear if and/or how lack of full density would influence the strength-temperature response. Once again, in this study, strengths were not measured below room temperature. The rate of increase of strength with decreasing temperature from 500K - 300K, however, suggests a Pt_3X - type behavior rather than the Co_3Ti-type behavior observed for $Al_{22}Fe_3Ti_8$ (if we assume that the observed rate is maintained for $Al_{67}Cr_8Ti_{25}$ at lower temperatures). If the observed peak at ~925K is in fact correct, then the strength-temperature profile of $Al_{67}Cr_8Ti_{25}$ is reminiscent of those for Pt_3Ga and Pt_3Sn rather than Pt_3Al. More recently, Zhang et al. (4) performed compression studies as a function of temperature from ambient to 1273K on cast, homogenized, and HIPed $Al_{67}Ti_{25}Cr_8$ and $Al_{67}Ti_{25}Mn_8$ ternary compounds. In contrast to the previous study, (3) they observed a mild peak in strength for the Al-Ti-Cr material at ~650K and for the Al-Ti-Mn material at ~800K.

Limited studies have been performed to characterize the dislocations and faults in these ternary compounds. Intrinsic stacking faults on {001} planes have been reported in the $L1_2$ compound $Al_{67}Ni_8Ti_{25}$, resulting from the dissociation of <001> {001} dislocations. (7) The authors claim that these faults do not participate directly in the deformation processes. (7) Turner et al. (8) reported compressive plastic deformation in polycrystalline $Al_{67}Ni_8Ti_{25}$ due to <110> {111} slip. They indicated that these dislocations were not dissociated by more than 2 nm. The observed brittle failure in tension at room temperature was attributed to an activation barrier for dislocation emission from crack tips.

Vasudevan et al., (9) examining the dislocation structures in $Al_{67}Ni_8Ti_{25}$ after compressive deformation at 573K and 873K, found that a major fraction of the <110> dislocations on the {111} planes existed as dipoles. These were speculated to cause rapid work hardening, (10) thus accounting for limited ductility and brittle failure. After the deformation at 573K, Vasudevan et al. discerned no dissociation of the dipole dislocations into 1/2<110> pairs, although a few <110> dislocations lying on the {001} planes dissociated into superpartial pairs. After the deformation at 873K, the dislocation structure was essentially the same, except that the density of dissociated <110> dislocations on {001} planes was higher. Many of the <110> dislocations on the {111} planes were still present as dipoles.

Schneibel and George, (11) reporting on the compression behavior of the binary $L1_2$ trialuminide Al_3Sc, found a strength-temperature profile resembling that of $Al_{22}Fe_3Ti_8$. They noted the similarity of this behavior to that of Pt_3Al at low temperatures and Ni_3Al at elevated temperatures, which is, in fact, a Co_3Ti-type behavior. However, Pt_3Al exhibits a much steeper strength-temperature gradient at low temperatures than that reported for Al_3Sc.

George et al. (12) substituted 5 at.% vanadium for titanium in $Al_{22}Fe_3Ti_8$ and reported on the dislocation structure after 1.5% ambient compressive deformation. They identified two types of dipoles: curved, discrete segments, and a type pulled out from a trailing superpartial. They also observed superpartial separation after ambient deformation, contrary to the reports by Vasudevan et al. (9) for $Al_{67}Ni_8Ti_{25}$.

Finally, George and Liu (13) reviewed the failure mode in these trialuminides. In spite of being soft, these compounds cleaved in an extremely brittle manner. All the commonly cited reasons for the brittleness of metals were ruled out and, by elimination, it was deduced that their brittleness was due to intrinsically poor cleavage strength. Consistent with this conclusion, first-principles quantum mechanical calculations (14) show that the cleavage strength of trialuminides is, in fact, significantly lower than that of a ductile $L1_2$ material like Ni_3Al.

This survey indicates that work done to date on these trialuminides is insufficient for a clear understanding of their deformation mechanisms. Further, even within this family of intermetallics, there are significant differences in deformation behavior between the individual compounds, for reasons that are not clear. Thus, these trialuminides must be treated individually with respect to their deformation characteristics rather than as a group. The effect of minor alloying additions on properties has been shown to be significant, although research in that direction has barely begun. These intermetallics, by virtue of their low density and potentially good oxidation resistance, are extremely attractive candidates for turbine engine applications, providing ample reasons for further research in this area.

B. PARTICULATE-REINFORCED INTERMETALLIC MATRIX COMPOSITES

Reinforcements in materials can be either continuous or discontinuous. Continuous reinforcements are typically fibers and occasionally laminates. Discontinuous reinforcements include particulates, short fibers, and whiskers. Discontinuous reinforcements are advantageous in that the composites are relatively easy to fabricate by P/M and I/M techniques and the resulting products exhibit isotropic behavior unless special efforts are made to align the reinforcement. Continuous reinforcement composites are more difficult to fabricate and exhibit anisotropic behavior; however, it is possible to obtain quasitropic materials by orientation of the various laminates in predetermined directions. Continuous reinforcements are usually more effective for reducing creep, as well as for enhancing ambient toughness, but the relative advantages of the two types of reinforcements are system and application dependent.

In intermetallic matrix composites, another major consideration is the mismatch in coefficient of thermal expansion (CTE) between the matrix and the reinforcing phase. Since these matrices are typically brittle, their ability to withstand the stresses generated during thermal cycling from CTE mismatch is not very high. In continuously reinforced composites, these stresses can lead to macroscopic cracking; in particulate composites, this may be less of a problem.

Reinforcements in intermetallics have been used for creep resistance improvement and/or ambient toughness enhancement. Although intermetallics are reported to be strong at high temperatures, this is not often the case (e.g., NiAl), particularly at slow strain rates that are representative of creep conditions. In such instances, reinforcing the intermetallic may enhance its high-temperature performance. Alternately, continuous and discontinuous ductile reinforcements have been used to enhance the toughness of intermetallics at low temperatures (300K). However, interfacial reactions during thermal cycling lead to the formation of brittle intermetallics at the interface, causing the crack to propagate along the interface rather than allowing it to be blunted by the reinforcing phase. Another approach that has been used to enhance toughness (and deter macroscopic failure) is reinforcing the intermetallic matrix with discontinuous fibers or continuous fibers that form "weak bonds" at the interface, leading to fiber pull-out during failure. Clearly, the selection of a matrix-reinforcement combination is dependent on the end use, because the characteristics required for enhancing creep resistance are not necessarily the same as those needed to improve toughness. In either event, matrix-reinforcement reactions, the thermal and metallurgical stability of the reinforcement, and the CTE mismatch must all be considered.

Several approaches have been documented to date to produce discontinuously reinforced intermetallic matrix composites. These range from traditional methods such as melt spinning (15) and mechanical alloying (16) to more novel techniques such as reaction sintering (17) and XD™ synthesis.(18) In the latter two processes, the exothermic reaction that accompanies the formation of an intermetallic compound is used to produce the composite. Since the focus of our research was particulate composites produced via the XD™ process, we present here recent results on intermetallic composites produced by this approach. The XD™ process can be used to produce a P/M product or an I/M product. The I/M route limits the reinforcement volume fraction to <10% due to melt viscosity problems, but the P/M process places no such limitation. However, P/M incorporates higher levels of impurities, such as oxides, compared to the casting route. Of the NiAl/TiB_2, CoAl/TiB_2, TiAl/TiB_2, and NiAl +Ni_2AlTi/TiB_2 systems reviewed below, only the TiAl/TiB_2 composites were produced by ingot metallurgy.

The addition of TiB_2 particulates to stoichiometric NiAl was shown to enhance the compression strength at 1300K (19) in proportion to the volume percent of TiB_2. The improvement was also observed at slow strain rates at 1300K; for a 20 vol.% TiB_2 material, compression flow stress at 1% strain was ~80 MPa under 1300K, $2x10^{-7}s^{-1}$ testing conditions compared to ~25 MPa for the monolithic material. The addition of these particulates to the NiAl decreased density and enhanced elastic modulus at room and elevated temperatures (up to 1373K) without degrading the fracture toughness.(20) Microstructurally, the particulates refined the grain size and served to pin dislocations during deformation, leading to the observed enhancement in flow stress relative to the monolithic material. Similar behavior was also observed in the CoAl/TiB_2 system. (21)

Since NiAl is inherently weak at high temperatures, multiphase matrices containing the $L2_1$ second phase (such as Ni_2AlTi) have been considered for improving its high-temperature capabilities.(22) In a recent study, (23) TiB_2 particulates were added to this dual-phase matrix of NiAl-Ni_2AlTi to further enhance the creep behavior. The high-temperature strength of the composite containing 20 vol.% TiB_2 was lower than that of the monolithic material at fast strain rates ($2x10^{-4}$ s^{-1}) but higher at slow strain rates ($2x10^{-7}s^{-1}$). This reversal in strength as a function of strain rate was rationalized as due to a threshold stress: above this stress, a matrix-particle incompatibility causes dislocations to be emitted at the matrix-particle interface, thus weakening the composite; at slow strain rates, the threshold stress is not reached, and the particles strengthen the matrix.

Incorporating TiB_2 particles in a Ti-47 at.% Al alloy, which consists of an $\alpha_2+\gamma$ (Ti_3Al + TiAl) microstructure, refines the as-cast grain size and, in turn, enhances the workability of the material. The as-cast microstructure in these two-phase materials typically assumes a lamellar morphology which benefits toughness but adversely affects the ductility. By appropriate heat treatments, it is possible to obtain an equiaxed microstructure that enhances ductility. (24) The refinement in grain size via TiB_2 addition enhances the kinetics of transforming the lamellar structure to an equiaxed structure, thereby improving ductility. The creep behavior of these particulate-reinforced titanium aluminides has been examined and improvements over the base material have been reported.(25)

III. EXPERIMENTAL TASKS

Four experimental tasks were proposed in the original statement of work.

Task I. Produce materials by the powder metallurgy XD™ process (12 compositions).

1. Powder metallurgy XD™ synthesis shall be used for the production of tau-based intermetallics; a total of 12 different powder compositions shall be fabricated as follows:

   (a) $Al_{22}Fe_3Ti_8$ + 0, 5, 10 and 20 vol. % TiB_2.
   (b) Modified $Al_{22}Fe_3Ti_8$ with 2Nb + 0, 5, 10, and 20 vol. % TiB_2.
   (c) Modified $Al_{22}Fe_3Ti_8$ with 2Mn + 0, 5, 10, and 20 vol. % TiB_2.

2. The 12 powder compositions shall be densified by hot pressing, hot isostatic pressing, and/or hot extrusion.

3. Sufficient quantities of fully dense materials of each of the 12 compositions to satisfy the needs of Task IV shall be produced.

Task II. Produce materials by the ingot metallurgy XD™ process (9 compositions).

1. Ingot metallurgy XD™ synthesis shall be used for the production of tau-based intermetallics; a total of 9 different compositions shall be fabricated as follows:

   (a) $Al_{22}Fe_3Ti_8$ + 0, 5, and 10 vol. % TiB_2.
   (b) Modified $Al_{22}Fe_3Ti_8$ with 2Nb + 0, 5, and 10 vol. % TiB_2.
   (c) Modified $Al_{22}Fe_3Ti_8$ with 2Mn + 0, 5, and 10 vol. % TiB_2.

2. Sufficient quantities of fully dense materials of each of the 9 compositions to satisfy the needs of Task IV shall be produced.

Task III. Establish the extent of the single-phase field for the ternary compound $Al_{22}Fe_3Ti_8$.

The composition limits of the $L1_2$ crystal structure tau phase shall be determined as a function of temperature between 900K and 1300K on the basic tau phase composition ($Al_{22}Fe_3Ti_8$).

Task IV. Conduct physical and mechanical property testing and supply materials to Lewis Research Center.

1. The following physical and mechanical property testing shall be undertaken:

	Test	Minimum Number Of Materials To Be Examined
(a)	Room-temperature density as a function of volume fraction TiB_2	3
(b)	Coefficient of thermal expansion as a function of volume fraction TiB_2 and temperature between room temperature and 1300K	3
(c)	Elastic modulus as a function of volume fraction TiB_2 and temperature between room temperature and 1300K	3
(d)	Compressive yield strength as a function of volume fraction TiB_2 and temperature between room temperature and 1200K	3
(e)	The brittle-to-ductile transition temperature as a function of volume fraction TiB_2, by biaxial flexure testing	3
(f)	Tensile testing above the ductile-to-brittle transition temperature as a function of volume fraction TiB_2.	3

2. Sufficient fully dense materials from at least three different tau-based composites shall be made available to the Lewis Research Center for additional characterization, such as short-term tension testing, tensile creep testing, compressive creep testing, oxidation testing, and microstructural analysis.

3. Sufficient tau-based intermetallic powder from at least two compositions shall be made available to the Lewis Research Center for studies of the fabrication of advanced fiber-reinforced composites and hot extrusion.

IV. EXPERIMENTAL PROCEDURE

A. MATERIAL PREPARATION

Discontinuously reinforced composites of the $L1_2$ trialuminides $Al_{22}Fe_3Ti_8$, $Al_{67}Cr_8Ti_{25}$, and $Al_{66}Mn_9Ti_{25}$, containing 0 to 20 vol. % TiB_2 particulates ~1 µm in size, were produced by the XD™ process. (18) The monolithic forms and composites with low-volume percentages of reinforcement (5 vol.% TiB_2) were processed by ingot metallurgy (I/M) and powder metallurgy (P/M) approaches; the high-volume-percent reinforcement composites (10 vol.% and 20 vol.% TiB_2) were processed only by the P/M route due to melt viscosity problems that prohibit the use of conventional casting processes. The effect of minor quaternary alloying substitutions (2 at.% Mn and 2 at.% Nb) in $Al_{22}Ti_8Fe_3$ on the mechanical properties was also examined.

The bulk of the P/M effort involved monolithic and particulate composites based on the Al-Ti-Fe system. A limited amount of effort was expended on processing the Al-Ti-Cr- and Al-Ti-Mn-based composites (20 vol. %TiB_2) by the P/M approach, although the monolithic ternary materials in the latter two systems were obtained by pulverizing ingots to the desired powder screen size.

1. P/M Approach

Appropriate amounts of elemental powders in the -150-µm to +44-µm size range were blended to obtain the ternary and quaternary compositions shown in Table I. The ternary compounds were prepared with two Fe levels: 6.7 at.% and 8.75 at.%; in both cases, the $L1_2$ phase $Al_{22}Fe_3Ti_8$ was dominant although additional phases were present. Excess Ti and submicron boron powders were added to obtain composites containing 5, 10, and 20 vol.% TiB_2 particulates. In all cases, the powders were cold isostatically pressed and processed by XD™ synthesis. (18) Exact compositions were determined by wet chemical analysis (Table II) and were close to the target compositions shown in Table I. The resulting product was crushed, milled to ≤63 µm size, vacuum hot-pressed at 1473K for 2 h under a load of 20 MPa, and subsequently hot isostatically pressed (HIPed) to full density at 1473K for 4 h in argon at a pressure of 200 MPa. The density of the HIPed material was measured by both specimen geometry and immersion techniques and compared against anticipated densities where possible (Table III).

Table I - Target Compositions for Monolithic and Composite Materials Produced via the P/M Route

	Weight Percent						
	Al	Ti	Fe	Cr	Mn	Nb	B
Al-Ti-Fe	48.21	41.11	10.65				
Al-Ti-Fe + 5 vol% TiB_2	45.39	42.77	10.00				1.82
Al-Ti-Fe + 10 vol% TiB_2	42.62	44.38	9.35				3.61
Al-Ti-Fe + 20 vol% TiB_2	37.22	47.48	8.17				7.07
Al-Ti-Fe(+2 at% Mn)	45.97	40.48	10.46		3.06		
Al-Ti-Fe(+2 at% Mn) + 5 vol% TiB_2	43.29	42.18	9.88		2.90		1.79
Al-Ti-Fe(+2 at% Mn) + 10 vol% TiB_2	40.68	43.78	9.25		2.72		3.57
Al-Ti-Fe(+2 at% Mn) + 20 vol% TiB_2	35.56	46.97	8.09		2.38		7.04
Al-Ti-Fe(+2 at% Nb)	46.98	37.50	10.39			5.14	
Al-Ti-Fe(+2 at% Nb) + 5 vol% TiB_2	44.34	39.27	9.76			4.85	1.77
Al-Ti-Fe(+2 at% Nb) + 10 vol% TiB_2							
XD synthesis	41.72	41.02	9.18			4.55	3.49
Mechanically alloyed							
Al-Ti-Fe(+2 at% Nb) + 20 vol% TiB_2	36.57	44.47	8.05			4.00	6.89
Al-Ti-Fe (higher Fe, lower Ti)	49.30	36.80	13.90				
Al-Ti-Fe (higher Fe, lower Ti) + 20 vol% TiB_2	38.06	44.04	10.72				7.06
Al-Ti-Cr	52.84	35.00		12.19			
Al-Ti-Cr + 20 vol% TiB_2	40.77	42.73		9.35			7.12
Al-Ti-Mn	51.30	34.51			14.21		
Al-Ti-Mn + 20 vol% TiB_2	40.62	41.57			11.27		6.44

Table II - Measured Compositions for Monolithic and Composite Materials Produced via the P/M Route

	Weight Percent						
	Al	Ti	Fe	Cr	Mn	Nb	B
Al-Ti-Fe	49.20	38.10	10.70				
Al-Ti-Fe + 5 vol% TiB_2	46.80	43.10	9.95				1.27
Al-Ti-Fe + 10 vol% TiB_2	43.00	44.70	8.98				3.53
Al-Ti-Fe + 20 vol% TiB_2	35.30	47.70	7.52				6.62
Al-Ti-Fe(+2 at% Mn)	46.40	41.00	10.10		3.01		
Al-Ti-Fe(+2 at% Mn) + 5 vol% TiB_2	42.10	41.90	8.74		2.67		1.20
Al-Ti-Fe(+2 at% Mn) + 10 vol% TiB_2	40.60	43.90	8.62		2.68		3.13
Al-Ti-Fe(+2 at% Mn) + 20 vol% TiB_2	35.10	47.20	7.94		2.39		6.73
Al-Ti-Fe(+2 at% Nb)	48.60	38.40	10.30			4.82	
Al-Ti-Fe(+2 at% Nb) + 5 vol% TiB_2	45.50	40.20	9.86			4.62	1.62
Al-Ti-Fe(+2 at% Nb) + 10 vol% TiB_2							
XD synthesis	42.50	41.00	9.04			4.50	3.02
Mechanically alloyed	41.20	37.80	9.26			4.21	4.07
Al-Ti-Fe(+2 at% Nb) + 20 vol% TiB_2	34.30	45.10	8.00			4.33	6.83
Al-Ti-Fe (higher Fe, lower Ti)	43.00	34.80	13.70				
Al-Ti-Fe (higher Fe, lower Ti) + 20 vol% TiB_2	34.90	43.30	11.00				6.29
Al-Ti-Cr	44.20	33.30		11.50			
Al-Ti-Cr + 20 vol% TiB_2	35.60	41.00		8.62			6.56
Al-Ti-Mn	41.10	31.90			13.40		
Al-Ti-Mn + 20 vol% TiB_2	35.30	41.20			10.50		6.60

Table III - Anticipated and Measured Densities for the Monolithic and Particulate Composites (g/cm^3)

Compound	Anticipated	Hot Pressed (g/cm^3)	Hot Pressed and HIPed
τ (6.7 at.% Fe)	3.81	----	3.82
τ + 5 vol. % TIB_2	3.84	3.53	3.61
τ + 10 vol. % TIB_2	3.88	3.90	3.87
τ + 20 vol. % TiB2	3.95	3.94	3.95
τ + (8.75 at.% Fe)	3.81	---	3.98
τ + 20 vol. % TiB_2	3.95	---	3.98
τ_{Nb}	3.94	3.83	3.88
τ_{Nb} + 5 vol. % TiB_2	3.97	3.90	3.95
τ_{Nb} + 10 vol. % TiB_2	4.00	3.90	---
τ_{Nb} + 20 vol. % TiB_2	4.05	4.01	4.02
τ_{Mn}	3.85	3.83	---
τ_{Mn} + 5 vol. % TiB_2	3.88	3.70	3.88
τ_{Mn} + 10 vol. % TiB_2	3.92	3.94	3.97
τ_{Mn} + 20 vol. % TiB_2	3.98	---	4.00

Note: $\tau = Al_{22}Fe_3Ti_8$; $\tau Nb = Al_{22}Fe_3Ti_8$ (6.7 at.% Fe) + 2 at.% Nb;

$\tau_{Mn} = Al_{22}Fe_3Ti_8$ (6.7 at.% Fe) + 2 at.% Mn

2. I/M Approach

Two-kilogram ingots of the ternary compounds $Al_{67}Ti_{25}Cr_8$ and $Al_{66}Ti_{25}Mn_9$ and a composite of $Al_{66}Ti_{25}Mn_9$ containing 5 vol.% TiB_2 particulates were prepared by induction melting of high-purity binary master alloys under an argon atmosphere. (The XD™ process was used as a precursor for making the composite.) The alloys were melted in zirconia crucibles and poured into graphite molds. Cylinders (60 mm in diameter x 64 mm high) were electrodischarge-machined from the as-cast materials and were homogenized in slowly flowing argon first at 1323K for a day, followed by 4 days at 1473K. The homogenized material was examined optically to ensure a substantially single-phase microstructure. The cylindrical sections were isothermally forged to approximately 18-mm-thick "pancakes" at Pratt & Whitney in Florida. Results of wet chemical analysis on these castings and forgings are shown along with target compositions in Table IV. The interstitial levels of C,N,O, and H in the two forgings are also reported in Table IV. The reasons for the high levels of oxygen in the Mn-based forging are not known, since the same processing conditions were used for both materials. It is possible that the Mn-containing master alloy had a high oxygen level to start with. It must be noted that attempts were made to cast and forge the Fe-based monolithic and composite materials but were unsuccessful due to cracking during homogenization or during forging.

Table IV - Target and Measured Compositions of the Ternary $L1_2$ Compounds Produced By I/M and Forging (wt%)

Compound		Al	Ti	Cr	Mn	O	N	C	H
$Al_{67}Ti_{25}Cr_8$	Target	52.8	35.0	12.2	–	–	–	--	–
	Forging, Measured	51.7	35.9	12.3	–	0.05	0.03	0.02	0.003
	Casting, Measured	52.4	35.0	12.5	–	–	–	--	–
$Al_{66}Ti_{25}Mn_9$	Target	51.3	34.5	–	14.2	–	–	--	–
	Forging, Measured	49.2	34.5	–	15.8	0.14	0.16	0.01	0.002
	Casting, Measured	50.3	34.8	–	14.7	–	---	--	–

B. MECHANICAL TESTING

1. Compression Tests

Compression specimens (5.1 mm diameter x 10.9 mm high) were electrodischarge-machined from the HIPed material and the forgings and tested at a strain rate of ~10^{-4} s^{-1} at temperatures ranging from 300K to 1373K. In some instances, compression tests were performed at 77K in liquid nitrogen (77K) and at 205K in a methanol/dry ice solution. Load-displacement curves were generated and from these, the 0.2% offset yield strength was calculated as a function of temperature.

In addition, slow-strain-rate compression studies were done at NASA Lewis Research Center at constant crosshead speeds. Strain rates ranged from 2 x 10^{-4} s^{-1} to 2 x 10^{-7} s^{-1}, and temperatures from 900K to 1200K. Samples were deformed in air to ~8 percent strain. True compressive stresses, strains, and strain rates were calculated from the autographically recorded load-time charts by the offset method (26), under the assumption of constant volume.

2. Bend Tests

Three-point bend tests were performed on ground and polished specimens (32 mm x 7.9 mm x 3.1 mm) cut from the three ternary forgings, and load-displacement curves were generated. For tests at room temperature and 473K, resistance strain gages were glued onto the tensile side of the bend specimens. Bend tests at higher temperatures (up to 873K) were performed without strain gages, due to their temperature limitations. Since a bend test involves compressive stresses on one side of a piece and tensile stresses on the other, surfaces of some samples were diamond polished prior to the test and both (tension and compression) sides were examined optically after deformation. Load-strain curves were generated from the output of the resistance strain gages used for the tests at room temperature and at 473K.

As noted previously, sections of the cast and homogenized ingots of monolithic Al-Ti-Cr and Al-Ti-Mn were pulverized to $\leq$ 63 μm, hot-pressed, and HIPed to full density. Composites of Al-Ti-Cr-20 TiB_2 and Al-Ti-Mn - 20 vol. % TiB_2 were then produced by the P/M-XD™ process These four materials, together with the ternary P/M Al-Ti-Fe - 20 vol. % TiB_2 composite, were tested in bending at 473K, 623K, 773K, and 873K. Since the conventional bend-test jig uses tool steel pins, which limit the test temperatures to ~873K, a ceramic jig was fabricated to handle temperatures up to 1100K. The ductile-to-brittle transition temperature was defined as the minimum temperature where the load-displacement curve deviated from linearity.

3. Biaxial Flexure Tests

Specimens from the quaternary system Al-Ti-Fe-2Mn, containing various levels of TiB_2 reinforcements (0, 10, and 20 vol. %), were tested in biaxial flexure over a range of temperatures from 900K to 1173K. Surfaces of disk-shaped specimens, 25.4 mm in diameter and 1.6 mm thick, were ground and polished to a 1-μm diamond finish. One disk was mounted on three sapphire spheres, and a fourth sphere was placed on top on the geometric center of the specimen. This setup was then loaded to failure and a load-displacement curve was generated. As in the bend tests, deviation of the load-displacement curve from linearity was taken as an indication of the brittle-to-ductile transition temperature.

4. Tensile Tests

Cylindrical "buttonhead" tensile specimens were electrodischarge-machined with the gage length lying in the radial plane of the monolithic forgings, finish-ground with 10-μm grit silicon carbide paper, and tested at a strain rate of $\sim 10^{-4}\ s^{-1}$ from ambient to 1073K for the Mn-based material, and at 623K and 923K for the Cr-based material. The 0.2% offset yield strength and plastic elongation were determined from the resulting load-displacement curves.

5. Fracture Toughness

Four cylinders, 12.7 mm diameter x 19.1 mm tall, were machined from each of the monolithic ternary forgings, chevron-notched, and tested at room temperature to obtain "short-rod" K_{IC} values. These tests were performed by Dr. R. Cutler at Ceramatech, Salt Lake City, Utah. All these samples indicated either residual stress or plasticity thus, valid toughness values could not be obtained. Larger diameter specimens were needed for valid K_{IC} values, but they were not obtainable because of size limitations on the forgings.

6. Coefficient of Thermal Expansion (CTE) Measurements

CTE measurements were made on 1) the forged monolithic Al-Ti-Mn, 2),3) Al-Ti-Fe + 10 vol. % TiB_2 and 20 vol. % TiB_2, 4) Al-Ti-Fe-2Nb, and 5) Al-Ti-Fe-2Nb + 20 vol. % TiB_2 (five samples in all) at the Lewis Research Center by Dr. M. Nathal. Samples were heated and cooled, in the temperature range 300K-1300K.

C. MICROSTRUCTURAL CHARACTERIZATION

X-ray diffraction (XRD), differential scanning calorimetry (DSC), optical microscopy, scanning electron microscopy (SEM) with fully quantitative energy-dispersive X-ray (EDX) analysis capabilities, and transmission electron microscopy (TEM) were used to characterize the materials produced in this program. Microstructure was characterized after hot processing, casting, homogenizing, and forging. Post-deformation microstructures were also examined. Fracture surfaces obtained from the bend and tensile tests were characterized by SEM. TEM samples were prepared by electrolytic jet polishing of 3-mm circular sections electrodischarge-machined from thin sections. Jet polishing was performed in a 25% HNO_3-methanol solution at 243K at 12-15 V.

V. RESULTS AND DISCUSSION

A. DETERMINATION OF THE $L1_2$ PHASE FIELD IN THE AL-TI-FE SYSTEM

The phase equilibria in the Al-Ti-Fe system have been studied in detail by several investigators. (27-29) In each instance, the presence of an $L1_2$ compound with a nominal composition corresponding to $Al_{22}Fe_3Ti_8$ was confirmed. However, there has been some disagreement on the location, shape, and extent of the single-phase field. Mazdiyasni et al. (29) very carefully established the compositional range of the $L1_2$ phase field at 1473K and 1073K. They showed the geometric center of the $L1_2$ phase field at 1473K to be 64 at.% Al, 28 at.% Ti, 8 at.% Fe, with a width of approximately 7%. This composition differs slightly from that reported by Siebold. (27) In the present study, we evaluated the extent of the $L1_2$ phase field at ambient temperature, 900K, 1100K, and 1300K to verify the previous observations; samples were held at temperature for 500 h in argon and quenched.

For this study, we fabricated eight 25-g ingots of the compositions listed in Table V by mixing elemental powders of Al, Ti, and Fe in the appropriate amounts, cold compacting the powders, and induction melting the compacts in an argon atmosphere. Sufficient superheat was provided to ensure complete melting. The ingots were then furnace-cooled again to room temperature. The location of the eight alloys on the ternary isotherm relative to the $L1_2$ (τ_3) phase is shown in Fig. 1. A portion of each ingot was mounted, polished, and examined optically and with a scanning electron microscope (SEM). Representative optical micrographs from these alloys are shown in Figs. 2a-f. As expected, a multiphase microstructure was observed in all eight samples. The $L1_2$ phase was the dominant phase in each case, although the morphology of the second (and third) phase differed depending on the types of phases present. Thus, in samples 2, 3, and 8, where the λ ($Fe_2Ti(Al)$) is anticipated, a Widmanstatten morphology is observed. The volume fraction of these phases increased with decreasing hold temperatures.

The composition of the matrix, as well as that of the precipitates, was measured by fully quantitative energy-dispersive X-ray analysis (EDX) with a standard ZAF iterative correction program. An average of 5-10 composition measurements were made and the typical spread was well within 1 at.%.

The presence of precipitates with the Widmanstatten morphology in some of the alloys made it very difficult to obtain the matrix composition in a reliable fashion. The problem is aggravated at the lower temperatures. Nevertheless, compositions for the matrix were determined and the locus of compositions was connected to obtain the $L1_2$ phase field boundary. The apparent geometric center of this phase field was determined to be 6.7 at.% Fe, 30 at.% Ti, and the balance Al. However, a cast and homogenized ingot of this center composition (Fig. 3) revealed a multiphase microstructure. The minor phases were identified as $Fe_2Ti(Al)$ and TiAl(Fe) by X-ray diffraction. Since the binary Fe_2Ti phase exhibits a large solubility for Al, the X-ray data for the binary compound do not match exactly with the data for $Fe_2Ti(Al)$ present in the ternary alloys. Therefore, a "button-melt" of Fe_2Ti containing significant amounts of Al was cast, homogenized, and used as a calibration sample for X-ray diffraction studies. The geometric center of the $L1_2$ phase field thus determined actually lies outside the single phase field, away from the Al-corner of the isotherm. This deviation is due to the errors involved in determining the matrix composition in those samples where the minor phases had a Widmanstatten morphology. In an attempt to produce a single-phase material, we fabricated an alternate composition, leaner in Ti and higher in Fe, close to the geometric center of the $L1_2$ phase field as determined by

Table V - Composition (wt.%) of Alloys Selected For $L1_2$ Phase Field Determination

Alloy #	Composition (wt.%)		
	Ti	Fe	Al
1	40	10	50
2	40	15	45
3	40	20	40
4	30	10	60
5	30	15	55
6	30	20	50
7	35	10	55
8	35	20	45

Mazdiyasni et al. (29) This composition corresponded to 8.75 at.% Fe and 27 at.% Ti, the balance Al.

B. COMPRESSION TESTING IN THE AL-TI-FE SYSTEM

Monolithic and composite materials in the Al-Ti-Fe, Al-Ti-Fe-2Nb and Al-Ti-Fe-2Mn systems were made via the powder route and characterized with respect to compression behavior in the hot-pressed and HIPed condition. Two nominal ternary compositions were examined: one with 6.7 at.% Fe and 30.3 at.% Ti, and one with 8.75 at.% Fe and 27 at.% Ti. The two quaternary compositions are based on the 6.7 at.% Fe compound with the 2 at.% Nb substituting for Ti and the 2 at.% Mn for Al.

Optical microscopy on etched cross sections of the hot-pressed and HIPed samples revealed a two-phase Widmanstatten morphology (Fig. 4a) in the 6.7 at.% Fe-containing material (low Fe, high Ti) and what appeared to be an essentially single-phase microstructure (Fig. 4b) in the 8.75 at.% Fe-containing material (high Fe, low Ti). Fine oxide particles were observed at prior powder particle boundaries in both these materials. Likewise, in the composites containing 10 and 20 vol.% TiB_2 in a 6.7 at.% Fe matrix (Figs. 4c,d), the Widmanstatten structure persists similar to that observed in the monolithic material (Fig. 4a). The size of the TiB_2 particles in these composites is such that it is difficult to differentiate them from the oxides using optical microscopy. It appears that the distribution is more uniform in the 20 vol.% TiB_2 material relative to the 10 vol.% composite (cf. Fig. 4c and 4d). Realistic grain size measurements could not be obtained in any of these materials. X-ray diffraction confirmed a predominantly $L1_2$ matrix in all the compositions examined, as well as the presence of TiB_2 in the composite materials. In the 6.7 at.% Fe-based material (low Fe, high Ti), in addition to an $L1_2$ matrix, a second and third phase were identified as λ (Fe_2Ti), containing significant amounts of dissolved aluminum, and γ (TiAl), containing Fe. In the 8.75 at.% Fe-based material (high Fe, low Ti), γ (TiAl) was absent, although weak peaks of λ (Fe_2Ti) were present.

The hot-pressed microstructures of the ternary monolithic compound containing 8.75 at.% Fe were examined at higher magnifications in a TEM; representative micrographs are shown in Figs. 5a-c. The second phase (hexagonal Fe_2Ti (Al), determined by X-ray diffraction) precipitates with a lath morphology on the cube faces of the $L1_2$ compound, as revealed by the 100 streaks in the diffraction pattern in Fig. 5a. Fringe contrast from the laths, inclined to the plane of foil, is seen in Fig. 5b. These precipitates also nucleate at grain boundaries, and in such instances are coarser than the matrix precipitates (Fig. 5c).

The results of the compression tests on the ternary monolithic and composite materials are shown in the form of compressive yield stress versus temperature curves in Figs. 6 and 7. From Fig. 6 (6.7 at.% Fe), it is seen that the particulate reinforcements play a significant role in strengthening such materials, particularly at ambient and warm temperatures. Specifically, the compressive yield strength (0.2% offset) increases at 700K from ~1250 MPa for the monolithic to ~1500 MPa for the composite containing 10 vol.% TiB_2 to ~1800 MPa for the 20 vol.% TiB_2 material. Further, a peak in strength, typical of several $L1_2$ compounds, is seen at ~800K, and is more pronounced for the 10 and 20 vol.% TiB_2-containing material than the monolithic.

Of particular technological relevance is the high-strength retention of these materials at 1000K where the monolithic and the composites exhibit similar strength levels of ~1000 MPa. In Fig. 7, it is seen that the 6.7 at.% Fe composition is stronger than its 8.75 at.% Fe counterpart in the monolithic form. This difference in strength is attributed to the combined effect of the presence of a larger volume fraction of second and third phases in the 6.7 at % Fe material, as well as the difference in the $L1_2$ matrix composition for the two in terms of Fe and Ti contents. In addition, from Fig. 7 it can be seen that for 20 vol.% particulate reinforcement, the strengthening is more pronounced in the 6.7 at.% Fe system than in the 8.75 at.% Fe system. This again could be caused by differences in interparticle spacing arising from the presence of a larger volume fraction of the minor phase(s) together with TiB_2 in the 6.7% Fe and/or the difference in the $L1_2$ stoichiometry between the two systems, which would influence defect energies and hence dislocation motion. At temperatures above 1000K, both monolithic materials have similar strengths and are stronger than the composites at any particular temperature (Fig. 7b). In fact, with increasing volume percent TiB_2 (Fig. 6), the strength at a particular temperature above 1000K decreases.

Post-deformation microstructures for the 8.75 at.% Fe monolithic material and its 20 vol.% TiB_2 composite (Figs. 8a-d) show that specimens deformed at 773K contain a significant residual amount of the second phase, while those deformed at 1073K have a substantially clean matrix, suggesting that almost all of the $Fe_2Ti(Al)$ has dissolved. Superdislocations with a finite separation can be seen in Fig. 8c, and the mottled appearance in the matrix of Fig. 8c, more clearly seen in Fig. 8d, results from the reprecipitation of $Fe_2Ti(Al)$ on a fine scale during air cooling of the specimen subsequent to deformation at 1073K. Thus, the ultra-high strength levels observed in this study at ambient and warm temperatures are attributed to the presence of a second and third phases (higher levels in the 6.7 at.% Fe ternary than in its 8.75 at.% Fe counterpart). The sudden drop in strength observed around 1000K is probably related to the dissolution of the second phase (and third when present).

The higher strength observed for the composites compared to the monolithics at ambient and warm temperatures is attributed to grain refinement and the impedance of dislocation motion by the particulates. The crossover in strength above 1000K can be explained on the basis of "dispersion weakening," (30) where at a certain threshold stress, the matrix-particle interfaces act as dislocation sources, pumping out dislocations which weaken the composite.

The Nb-containing quaternary compound (Fig. 9a) is very similar in behavior to the 6.7 at.% Fe ternary composition, both in the monolithic and composite forms, but shows a second crossover at ~1150K where the composites become marginally stronger than the monolithic. Thus, the substitution of 2 at.% Nb for Ti in the ternary composition does not influence the strength-temperature profile. This result is contrary to a recent report (31) where 2 at.% Nb was found to enhance the high-temperature strength in a substantially single-phase $L1_2$ $Al_{22}Fe_3Ti_8$. It is possible that at the much higher strength levels observed in the multiphase materials in our study, any positive effect of the Nb addition was masked. The Mn-containing quaternary compound (Fig. 9b), although it contains only 6.7 at.% Fe, responds more like the 8.75 at.% Fe ternary alloy and is, in fact, even weaker than the 8.75 at.% Fe ternary alloy below 1000K (Fig. 7a). In other words, the Mn appears to behave like Fe [i.e., it raises the "Fe level" (Fe + 2Mn) to 8.7 at.%]. Such a behavior can be anticipated since an $L1_2$ compound $Al_{66}Ti_{25}Mn_9$, is known to exist (3,9) and $Al_{22}Fe_3Ti_8$ may very well be in a solid solution with it. Further, from recent studies, (2,4) it can be shown that the Mn-based ternary compound is weaker than its Fe-based counterpart, which would explain our observation that the Mn-containing quaternary is even weaker than the 8.75 at.% Fe ternary. It is to be noted that while the monolithic Al-Ti-Fe + 2Mn is the weakest, its 20 vol.% composite is the strongest.

The effect of strain rate on flow stress at 1000K-1200K was studied based on compressive stress-strain data taken in the strain-rate regime 2 x 10^{-4} s^{-1} to 2 x 10^{-7} s^{-1}. Typical 1100K and 1200K true stress-strain curves are presented in Figs. 10-12 for the ternary (6.7 at.% Fe and 8.75 at.% Fe) monolithic and composite materials. These plots illustrate the general behavior of all tested materials: during fast straining (Figs. 10a, 11a and 12a), the samples exhibited work-hardening through the first ~1% deformation, diffuse yielding over nominally 1-2% strain, and then strain-softening; under slow compressive conditions (Figs. 10b, 11b and 12b), the intermetallics exhibited work-hardening through the first ~1% deformation, followed by continued flow under a more or less constant stress (steady state). Testing at the intermediate rates of 2 x 10^{-5} s^{-1} and 2 x 10^{-6} s^{-1} resulted in curves that were similar in appearance to those in Figs. 10a, 11a and 12a, but showed a gradual transition from diffusive yielding to steady state with decreasing deformation velocity. A few tests at 1000K and a strain rate of 2 x 10^{-5} s^{-1} resulted in stress-strain plots similar to those in Fig. 10a.

At fast strain rates (Figs. 10a, 11a, and 12a), the particulate composites are weaker than the unreinforced matrix at both 1100K and 1200K, irrespective of the Fe content; furthermore, the low-Fe matrix is somewhat stronger than the 8.75 at.% Fe version. Testing under the slowest strain rate conditions (Figs. 10b, 11b, and 12b), however, demonstrates that 20 vol.% TiB_2 can produce some strengthening at 1100K and 1200K, whereas the effect of 10 vol.% is slight at best (Figs. 10b, 11b). We apply our previous argument to explain the observed reversal in strength with fast strain rate between the monolithic and composite: the threshold stress for dislocation generation at matrix-particle interfaces is not reached at the slowest strain rate; thus, the particles strengthen the matrix.

True compressive stress-strain rate behavior for the unreinforced matrices and both 20 vol.% TiB_2-containing composites at 1000K, 1100K, and 1200K are illustrated in Fig. 13. The flow stresses (σ) and deformation rates ($\dot{\varepsilon}$) from the constant velocity tests were evaluated at 1 % strain, a value that gives a reasonable estimate of the maximum strength of the aluminide, irrespective of the type of stress-strain diagram (Figs. 10-12). The data were fitted by linear regression techniques to the usual temperature-compensated power law:

$$\dot{\varepsilon} = B\sigma^n \exp(-Q/RT)$$

where B is a constant, n is the stress exponent, R is the universal gas constant, and T is the absolute temperature. The values for these parameters and the Coefficients of Determination are given in Table VI for all the ternary materials.

The data in Fig. 13 support the contention that both the 6.7 at.% Fe matrix and its 20 vol.% TiB_2 composite are slightly stronger than their 8.75 at.% Fe counterparts between 1000K and 1200K. Although there are differences in strength, the regression fits and the stress exponents and activation energies (Table VI) are, for all practical purposes, independent of the iron content for each form. Hence, the elevated-temperature, slow plastic-deformation mechanism(s) in either the matrix or the composite is little affected by chemistry (at these temperatures, the matrix is essentially single-phase for both compositions), at least for materials evaluated in this study. Comparison of the stress exponents and activation energies calculated (Fig. 13 and Table VI) clearly show that both n and Q are much higher for the composite than

Table VI - Temperature-Compensated Power Law Fits of True Compressive Flow Stress - Strain-Rate Data for Monolithic and Composite Materials

	B (s^{-1})	n	Q (kJ/mol)	Rd^2
Matrix(1)				
6.7 at.% Fe	1.15×10^3	2.80	308.6	0.983
8.75 at.% Fe	1.56 x 103	2.90	312.5	0.986
Composites(2)				
6.7 at.% Fe + 10 vol.% TiB_2	2.89×10^6	3.63	413.0	0.978
6.7 at.% Fe + 20 vol.% TiB_2	1.87×10^6	4.77	464.7	0.982
8.75 at.% Fe + 20 vol.% TiB_2	3.10×10^6	4.79	466.4	0.957

(1) Standard deviation of n and Q = ~0.15 and ~25 kJ/mol, respectively.

(2) Standard deviation of n and Q = ~0.27 and ~50 kJ/mol, respectively.

The 1200K true stress-true strain curves for the 2 Nb quaternary compound with various levels of TiB_2 particulate reinforcements are shown in Figs. 14a, b for fast (2×10^{-4} s^{-1}) and slow (2×10^{-7} s^{-1}) strain rates, respectively. At the fast strain rate, the flow stress for any strain level decreases with increasing volume fraction of reinforcement. For the first 2% strain, the 0 and 5 vol.% TiB_2 material exhibits work-hardening followed by some softening, whereas a more or less constant stress is observed for the higher reinforcement levels. At the slowest strain rate (Fig. 14b), the monolithic material is the weakest and the 20 vol.% TiB_2 composite the strongest. At this strain rate, the materials show some work-hardening over the first 1% strain, followed by a steady-state stress level. Flow stress at 1% strain versus strain rate at ~1200K is shown in Fig. 15 for the 2 Nb quaternary monolithic and composites materials. The behavior is consistent with that observed for the ternary system (Fig. 13). The composites are weaker than the monolithic material at the highest-strain rate but the reverse is true at the slowest strain rate. Finally, the effect of quaternary addition on flow stress as a function of strain rate, shown in Fig. 16, clearly indicates that the minor alloying additions do not strongly influence the behavior of the ternary compound, at least at 1200K.

C. COMPRESSION TESTING IN THE Al-Ti-Mn AND Al-Ti-Cr SYSTEMS

Al-Ti-Mn and Al-Ti-Cr monolithic materials and a forged composite of the Al-Ti-Mn intermetallic containing 5 vol.% TiB_2 were made via the I/M route and isothermally forged. Additionally, a section of the ingot of each of the monolithic ternary compounds was pulverized and hot-pressed and HIPed to full density, yielding some relatively fine-grained material. Finally, composites containing 20 vol.% TiB_2 in both ternary matrices (Al-Ti-Mn and Al-Ti-Cr) were fabricated by the P/M XD™ process and tested in compression.

Low-magnification photographs of the two monolithic forgings are shown in Fig. 17. Both intermetallics forged extremely well, exhibiting virtually no edge cracking. The Mn-containing $L1_2$ compound exhibited better fabricability than the Cr-containing counterpart. Successful forging of such materials promises a viable processing route for near-net-shape components such as blades and compressors in engines. Forged microstructures in radial and transverse orientations are shown in Figs. 18a,b, respectively. In general, the microstructure appears fully recrystallized. The grain size is typically about 50 μm, with aspect ratios that generally are not more than about two.

Transmission electron microscopy of thin foils of the forged Al-Ti-Cr and Al-Ti-Mn $L1_2$ compounds reveals well-formed subgrains (Figs. 18c, d), about 1-3 µm in size, as well as loosely knit dislocation cell walls and well-defined sub-boundaries (Figs. 18e, f). Thus, isothermal forging not only fully densifies the material and refines the grain size, but also introduces fine subgrains that are likely to influence the subsequent deformation behavior.

Variation in compressive yield strength with temperature for these forged intermetallics can be compared in Fig. 19 to the results of Zhang et al. (4) for the cast, homogenized, and HIPed material of both alloys and of Mabuchi et al. (3) for their powder metallurgy-processed $Al_{67}Ti_{25}Cr_8$ composition. In general, at any particular temperature, these two compounds were not as strong as $Al_{22}Ti_8Fe_3$; (1) further, they both exhibited a mild positive temperature dependence of strength (really a plateau between 600K and 1000K rather than a peak). The strength at any given temperature compared well with the results of Zhang et al. (4) In contrast, compressive yield strengths for forged alloys in this study were lower than those reported earlier by Mabuchi et al., (3) and a prominent peak in strength at 900K that was reported was not observed in the present study. It is possible that the higher strength observed by Mabuchi et al. (3) was a manifestation of the finer grain size and fine oxides resulting from the powder processing route adopted in that investigation. In addition, recent findings of Zhang et al. (4) indicate that the role of stoichiometry also significantly influences the yield strength values at any particular temperature. In the present study, strength increased with decreasing temperature below room temperature, and at a higher rate than that previously observed for ternary $Al_{22}Ti_8Fe_3$ and the quaternary Al-Ti-Fe-Nb (31) compounds. Thus, the observed strength-temperature profile for these two compounds is reminiscent of Pt_3Al rather than the Co_3Ti-type behavior reported for $Al_{22}Ti_8Fe_3$.(31)

Also presented in Fig. 19 is the strength-temperature profile for a composite of $Al_{66}Ti_{25}Mn_9$ containing 5 vol.% TiB_2 and processed by casting, homogenizing, and forging. This composite shows some improvements over its monolithic counterpart and is similar to the profile of the P/M product from Mabuchi et al.(3) Optical microscopy revealed the TiB_2 particles to be non-uniformly distributed in the forging, often clustered together. This is a consequence of the TiB_2 particles segregating to the interdendritic solute-rich regions of the casting during solidification.

As previously mentioned, an unused portion of each of the homogenized ingots that was sectioned for forging ($Al_{67}Ti_{25}Cr_8$ and $Al_{66}Ti_{25}Mn_9$) was milled to <44 μm powder and hot-pressed and HIPed to full density. Optical microscopy revealed fine oxide particles on the prior powder particle boundaries. Compression behavior as a function of temperature was determined for these ground I/M materials as well as for composites of $Al_{67}Ti_{25}Cr_8$ and $Al_{66}Ti_{25}Mn_9$ + 20 vol.% TiB_2 produced by the XD™ process (Fig. 20). The yield strengths of the ground I/M monolithic materials are significantly higher than those of the forged ingot metallurgy counterparts (Fig. 19), presumably due to grain-size refinement and the presence of the fine oxide particles in the P/M product. The addition of 20 vol.% TiB_2 to these matrices doubles the strength of the material up to ~900K; at higher temperatures, the strengths converge, decreasing to ~200 MPa at 1173K.

True compressive stress-strain diagrams at 1000K as a function of nominal strain rate are presented in Fig. 21a for the forged $Al_{67}Ti_{25}Cr_8$ and $Al_{66}Ti_{25}Mn_9$. Both materials display a range of behaviors from continuous work-hardening at the highest rates to more or less steady state (continued flow at a nominally constant stress) at the lowest rates. At strain rates of 2×10^{-6} s^{-1} and 2×10^{-7} s^{-1}, for strains > 1%, the Cr-based compound is stronger than the Mn-based intermetallic. At 1100K (Fig. 21b), both materials once again display a range of behaviors depending on the strain rate. However, at low strains (<2%), the strength of $Al_{67}Ti_{25}Cr_8$ is relatively insensitive to deformation rates exceeding 2×10^{-6} s^{-1}, whereas $Al_{66}Ti_{25}Mn_9$ shows distinct softening at rates less than 2×10^{-5} s^{-1}.

The strengths of both compounds can be directly compared in Fig. 22, which illustrates the flow stress at 1% strain as a function of strain rate and temperature. At 1000K, the flow stress for the two compounds is similar except at the lowest rate where $Al_{67}Ti_{25}Cr_8$ is stronger. Although an increase in temperature to 1100K does not greatly reduce the strength of either composition at the highest strain rate, clearly the properties of $Al_{66}Ti_{25}Mn_9$ and $Al_{67}Ti_{25}Cr_8$ are affected at rates below ~2×10^{-5} s^{-1} and ~2×10^{-6} s^{-1}, respectively.

Figures 23a-c show true compressive stress-strain profiles from 900K-1100K in the strain-rate regime 2×10^{-4} s^{-1} to 2×10^{-7} s^{-1} for the forged $Al_{66}Ti_{25}Mn_9$ + 5 vol.% TiB_2 composite. At 900K, continuous work-hardening is observed independent of strain rate, and the flow stress is for all practical purposes independent of strain rate for small strains (~1%). For higher strains, the scatter in data is too large to discern a trend (Fig. 23a). At 1000K, continuous work-hardening is again observed independent of strain rate, except that the material is appreciably softer at 2×10^{-7} s^{-1} compared to the faster strain rates. At 1100K, continuous work-hardening is observed at 2×10^{-4} s^{-1}, while, at lower strain rates, after approximately 1% strain, steady-state flow is achieved. Variation in flow stress at 1% strain with strain rate is shown for the three temperatures in Fig. 24a and a corresponding figure for flow stress at 3% strain in Fig. 24b. From these two figures, it can be seen that flow stress is independent of strain rate in the range 2×10^{-4} s^{-1} to 2×10^{-7} s^{-1} at 900K. At 1000K, the flow stress at 1% strain is independent of strain rate between 2×10^{-4} s^{-1} and 2×10^{-6} s^{-1}, although flow stress decreases at 2×10^{-7} s^{-1} (Fig. 24a); however, flow stress at 3% strain shows a strain-rate dependency even between 2×10^{-4} s^{-1} and 2×10^{-6} s^{-1} (Fig. 24b), and the dependency increases below 2×10^{-6} s^{-1}. At 1100K, a strain-rate dependency of flow stress is observed for both 1% and 3% strain, with the rate steeper below 2×10^{-6} s^{-1}.

The effect of strain rate on the compressive flow stress at 1000K and 1100K has been examined for the XD™-processed P/M composites of $Al_{67}Ti_{25}Cr_8$ and $Al_{66}Ti_{25}Mn_9$ containing 20 vol.% TiB_2. The true stress-true strain curves for these composites are shown in Figs. 25a-d. These two composites essentially behave similarly. At 1000K and a strain rate of 2×10^{-4} s^{-1}, both composites exhibit work-hardening over the first 2% strain, followed by steady-state flow. At the lower strain rate, 2×10^{-5} s^{-1}, work-hardening is observed only up to 1% strain, followed by strain-softening. At even lower strain rates, negligible work-hardening and steady-state flow are observed. Similar observations hold at 1100K.

Variation in flow stress at 1% strain with strain rate at 1000K and 1100K for these two composites is provided in Figs. 26a,b. Power-law behavior adequately describes the response at both temperatures. Stress exponents were 4.21 for the Cr-based composite and 4.7 for the Mn-based counterpart. The corresponding activation energies were 385.9 kJ/mole and 387.8 kJ/mole respectively.

D. THREE-POINT BEND TESTING

1. Forged I/M Compositions

The load-displacement curves obtained from the three-point bend tests are shown in Fig. 27a for the Al-Ti-Mn compound, in Fig. 27b for the Al-Ti-Cr compound, and in Fig. 27c for the Al-Ti-Mn compound containing 5 vol.% TiB_2. $Al_{66}Mn_9Ti_{25}$ exhibits a definite deviation from linearity at ambient, indicating plastic deformation. At elevated temperatures (i.e., 623K, 723K, and 873K), serrated yielding is observed, together with appreciable plastic deformation. The load drops during plastic deformation were accompanied by audible clicks. The nature of the serrations (i.e., wavelength and amplitude) also varies as a function of temperature (Fig. 27a). The Al-Ti-Cr compound, $Al_{67}Cr_8Ti_{25}$, failed before yielding both at room temperature and at 473K (Fig. 27b). At 623K, plasticity was observed, as was serrated flow. In this case, the test was interrupted prior to failure. At 723K, the sample exhibited plasticity, but failed soon after. At 873K, however, the specimen exhibited extensive plasticity, so that only a portion of the load-displacement curve is shown. It should also be noted that the type of serrations observed at 873K for the Al-Ti-Mn intermetallic (Fig. 27a) is very different from that observed for the Al-Ti-Cr (Fig. 27b) compound.

The load-displacement curves (Fig. 27c) for the composite exhibit some interestingly different features compared to their monolithic counterpart (Fig. 27a). Ambient ductility is absent in the composite, although at 473K, a definite deviation from linearity is observed. At intermediate temperatures (~650K), a drop in ductility is observed, followed by an increase in ductility. Over the entire temperature regime, serrated flow is absent, possibly because failure occurred prior to the onset of serrated flow in the intermediate-temperature range. The alternate possibility is that some (ppm) free boron influenced the deformation behavior and prevented plastic instability.

Load-strain curves were simultaneously generated for those specimens that had strain gages glued to them. For $Al_{67}Cr_8Ti_{25}$, the load-strain curves were linear at ambient and at 473K. In such a situation, elastic stress-strain curves can be generated, with the stress calculated using elastic-beam deflection equations. Load-strain curves for $Al_{66}Mn_9Ti_{25}$ deformed at room temperature showed a clear plastic portion where the permanent deformation was ~0.25 percent. Linear elastic-beam equations cannot be used to obtain the entire stress-strain curves for this situation.

However, an approximate yield strength of 310 MPa was obtained for the linear portion of the stress-strain curve, which is in reasonable agreement with the compressive yield strength (Fig. 19).

Optical micrographs obtained from polished surfaces of the compression and tension sides of the bend specimens are shown for the Al-Ti-Mn compound in Figs. 28, 29, and 30. Optical microscopy on the compressive side of a bend specimen fractured at 623K reveals extensive slip traces transitioning from one grain to another (Fig. 28a). In addition, the surface also assumes a rumpled appearance. Secondary cracks are visible and only a single set of slip traces (i.e., direction) is obvious in any particular grain (Fig. 28b).

The compression surface of a $Al_{66}Mn_9Ti_{25}$ sample deformed at 723K reveals a more pronounced rumpling, extensive slip traces, and, in addition, slip traces in more than one orientation within a particular grain (Fig. 29a). The density of these slip traces decays rather abruptly 3-4 mm away from the mid-point of the bend specimens. Similar deformation markings are also observed on the tensile surface of the specimen (Fig. 29b), with one important difference: the slip traces within a particular grain are in one orientation only, unlike the compression side of the same specimen but similar to the compression surface of the specimen deformed at 623K (Fig. 28b). In addition, the spacing between the slip traces increases significantly with distance from the midpoint of the specimen (the point of maximum tensile strain) (Fig. 29b), indicating how these traces progress with increasing strain.

Extensive slip traces are seen on both the compressive (Fig. 30a) and tensile (Fig. 30b) surfaces of the specimen (Al-Ti-Mn) deformed at 873K. In addition, even though this specimen was taken to failure, it did not "fall apart" but remained as a single piece. The regions adjacent to the primary crack on the tensile surface are shown in Fig. 30c. A secondary crack is visible which appears to propagate along grain boundaries. Extensive slip traces are seen and in certain regions, traces in more than one orientation are visible within a grain. It thus appears that higher temperatures are needed in tension relative to compression to activate slip in multiple orientations.

A representative micrograph of the tensile surface of the $Al_{67}Cr_8Ti_{25}$ bend specimen deformed at 623K is shown in Fig. 31. This test was interrupted (Fig. 27b) *prior to failure.* The tensile surface reveals fine multiple cracks even though the overall specimen continued to deform plastically. It is possible that the test was interrupted just before failure or, alternately, that the compression component could continue supporting the overall load even though tensile failure occurred.

Fracture surfaces resulting from these bend tests were examined in a SEM. The results are shown for $Al_{67}Cr_8Ti_{25}$ in Figs. 32-34 as a function of increasing temperature. At 300K and 473K, fracture occurs by transgranular cleavage; at 723K, while transgranular cleavage still predominates, occasionally intergranular grain-boundary failure is observed, mostly on the compression side of the specimen. At 873K, intergranular failure is observed on both the tensile and compressive sides of the specimen, mixed with some transgranular cleavage.

2. Hot-Pressed (P/M) Monolithic and Composite Materials

Bend specimens were electrodischarge-machined from the monolithic $Al_{67}Ti_{25}Cr_8$ and $Al_{66}Ti_{25}Mn_9$ compounds produced via the powder route, the 20 vol.% TiB_2 composites of these two compounds, and the $Al_{67}Ti_{25}Cr_8$ (8.75 at.% Fe) + 20 vol.% TiB_2 composite. Bend tests were performed at elevated temperatures, yielding the typical load-displacement curves shown in Fig. 35. From the curves, we identified ductile-to-brittle transition temperature (DBTT) ranges for these materials. As is evident, the addition of 20 vol.% TiB_2 lowers the DBTT of both $Al_{67}Ti_{25}Cr_8$ and $Al_{66}Ti_{25}Mn_9$ from 975K - 1075K to less than 975K. Also, the Al-Ti-Fe-based composite has a higher DBTT than the Al-Ti-Mn- and Al-Ti-Cr-based composites. Finally, while the I/M forgings exhibited bend ductility at much lower temperatures, the P/M monolithic material tested at room temperature (both the Al-Ti-Cr and Al-Ti-Mn compounds) was brittle, although in one instance, some plasticity was observed in a P/M sample of $Al_{67}Ti_{25}Cr_8$ tested at 473K.

The fracture surfaces for the P/M-processed monolithic $Al_{66}Ti_{25}Mn_9$ and the corresponding composite containing 20 vol.% TiB_2 are shown in Figs. 36 and 37. The monolithic specimen was tested at 773K and the composite at 973K. In both cases, cleavage was the dominant mode of failure. In the monolithic and composite samples, fine oxide particles (~0.5 μm) are seen on the fracture surface. The TiB_2 particles are frequently larger than the oxide particles and fracture propagates along the matrix-particle interface, as shown in Fig. 37b.

E. BIAXIAL FLEXURE TESTING

Specimens from the quaternary system Al-Ti-Fe-2Mn, containing various levels of TiB_2 reinforcements (0, 10, and 20 vol. %), were tested in biaxial flexure over a range of temperatures from 900K to 1173K. Up to 1150K, the monolithic quaternary hot-pressed aluminide exhibited no plasticity in biaxial flexure. Similar behavior was observed for the aluminide containing 10 vol. % TiB_2. However, the 20 vol. % TiB_2 composite showed significant plasticity even at 1125K, suggesting a lower ductile-to-brittle transition temperature and a positive effect of TiB_2 reinforcement. This trend is in qualitative agreement with previous observations from bend tests on the monolithic and composite specimens. A major drawback of the biaxial flexure test is the large surface-to-volume ratio of the specimen, which increases the chances of surface flaws in the specimen.

F. UNIAXIAL TENSION TESTING

Cylindrical "buttonhead" tensile specimens machined from the monolithic $Al_{66}Ti_{25}Mn_9$ forging were tested at an approximate strain rate of 5×10^{-5} s^{-1} in a universal testing machine with specially fabricated Inconel grips. Load-displacement curves in uniaxial tension revealed serrated flow behavior in the warm-temperature regime. A similar response was previously observed in compression and in three-point bending for this compound. Within this temperature range, the serrations were finer and more closely spaced at the low-temperature end than those at the high-temperature end, which were coarser and intermittent; a mixed mode existed in between. At a given temperature, particularly in compression where extensive deformation can be obtained, the amplitude of the serrations increased continuously with increasing strain.

Figure 38 shows the variation in the 0.2% offset tensile yield strength with temperature for $Al_{66}Ti_{25}Mn_9$. The yield strength remains at about 320 MPa from 298K to 625K, but then drops rather abruptly to 230 MPa with only a slight further decline up to 1073K. A comparison of the yield strength-temperature profiles in tension and in compression (dashed lines, Fig. 38) reveals that this abrupt change in tensile yield strength at ~625K is absent in compression. The compressive yield strength is lower than the tensile yield strength below 625K; however, above 625K, they are similar. The observed higher yield strengths in tension relative to compression at any particular temperature between 298K and 623K remain unexplained at present. Compression and tension specimens were obtained from the same forging, which exhibited a uniform grain size and second phase (~3%) distribution. Strain rates used in compression and tension tests were comparable.

The variation in tensile elongation with temperature for $Al_{66}Ti_{25}Mn_9$ is presented in Fig. 39. Ambient ductility was measured to be about 0.2%, increasing to 1.3% at 623K. A minimum in ductility is observed centered around 773K, along with a drop in tensile elongation to 0.3%; elongation then increases continuously to 5% at 1073K. The ductility drop at the intermediate temperature coincided with the onset of serrated flow and the abrupt tensile yield strength decrease observed in Fig. 38.

The nonlinear parts of the stress-strain curves at the various test temperatures were reconstructed in the plastic strain interval 0.02% to 1.3% (where possible) from calculations of the stress based on the original cross-sectional area (Fig. 40). These curves can be broadly divided into those for the temperature range 298K - 623K and those for temperatures greater than 623K. It can be seen that the initial work-hardening rate (0.02% to 0.2% plastic strain) is higher in the first group. Further, the room-temperature specimen exhibits linear work-hardening behavior between 0.02% and 0.2% plastic strain, where it fails. At 473K and 623K, the work-hardening rate from 0.02% to 0.1% plastic strain is similar to that at 298K, but the rate between 0.1% to 0.2% offset strain is lower than the previous rate and therefore also lower than that for the corresponding strain interval in the 298K specimen. For any fixed strain level, the flow stress for the second group is significantly lower than that in the first group.

Some of these findings are depicted by the yield strength-temperature profiles in Fig. 41. As shown, the high linear work-hardening rate at 298K leads to a mild positive temperature dependence of strength for the 0.02% offset and the 0.1% offset, a trend that is absent for the 0.2% offset (cf Fig. 38 and Fig. 41).

In an attempt to understand the observed mechanical behavior in tension, we examined the fracture surfaces in a SEM. At ambient temperature, fracture was due predominantly to transgranular cleavage (Fig. 42a). The fracture surface of the specimen deformed at 473K consists of transgranular cleavage facets (Fig. 42b), although, occasionally, intergranular failure can be seen. One such region of intergranular failure, shown in Fig. 42c, contains smooth-faceted grain boundaries and occasional fracture across the grain. These grain-boundary failures were seen frequently along the circumference of the specimen. At 623K, there is more evidence of intergranular failure mixed with transgranular cleavage (figure not shown). The fracture surface of a specimen tested at 773K (Fig. 42d), where a minimum in ductility was observed, is very similar to that of the specimen tested at 623K, consisting essentially of a mixture of grain-boundary failure and transgranular cleavage. Fracture propagated almost exclusively via an intergranular mode in a specimen tested at 923K (Fig. 42e). The resulting grain-boundary surfaces appear smooth, with no indication of ductile tearing, but the tensile ductility at this temperature was ~1.3%. At 1073K, for the first time, the material underwent appreciable plastic deformation (~5%), although the corresponding tensile fracture surface continues to exhibit intergranular failure (Fig. 42f); however, the grain boundaries are no longer sharp-cornered and smooth-surfaced, but show signs of “dimpling” and “tearing,” as would be expected of a material exhibiting 5% plastic elongation. Thus, with increasing test temperature, the fracture mode transitioned from entirely transgranular cleavage failure to a mixture of cleavage and intergranular failure to predominantly intergranular failure with smooth grain boundary facets, and then to “dimpling” and “tearing.”

To study dislocation structures, we examined a thin foil of $Al_{66}Ti_{25}Mn_9$ in a TEM before and after deformation. The microstructure exhibited a low dislocation density and subgrains, likely from the forging step. The foil was then removed, excessively loaded in the TEM specimen holder to induce a crack, and re-examined in the TEM. The region ahead of a crack tip that advanced is shown in Fig. 43a. Clearly, dislocations were emitted at the crack tip in this material. In addition, a series of closely spaced dislocations lying in a narrow slip band can be seen, suggesting the possibility of dislocation pile-up, probably at an adjacent grain boundary. Likewise, in Fig. 43b, which shows regions adjacent to another crack, a high dislocation density is seen restricted to a narrow region, and closely spaced dislocations are observed lying in narrow slip bands. The burgers vector, **b**, of these dislocations was determined to be of the $a_0[101]$ type (Figs. 44a-d), while their line direction was [211], yielding a (111) slip plane and implying octahedral slip. These observations must be treated with appropriate caution in that plane-stress conditions prevail in this foil; moreover, the strain rate at which fracture was propagated in the foil is not known but is likely higher than that applied in the conventional tensile tests in this study ($\sim 5 \times 10^{-5}\ s^{-1}$).

The nature of dislocations in the tensile specimens deformed at 623K (1.3% plastic strain) and at 923K (1.2% plastic strain) is depicted in Figs. 45a-c and 46a-c, respectively. In all cases, the superdislocations had burgers vectors, **b**, of the a_0<110> type. At 623K, deformation proceeds predominantly by octahedral slip (Fig. 45c) whereas at 923K, cube slip is also present (Fig. 46c). At 923K, some dislocations are observed (N, T, Z) with line directions (Fig. 46c) parallel to the burgers vector, implying that they exhibit pure screw character. Other dislocations (e.g., M, R, S), with line directions close to the <110>-type directions, subtend an angle of 60 degrees with their burgers vectors. In the 623K specimen, dislocation D was the only case where a possible pure screw character was observed and even then, it is angularly separated from b = [101] by at least 10 degrees.

In a previous study, Zhang et al. (4) used weak-beam techniques to resolve superpartial separation in $Al_{67}Ti_{25}Mn_8$ deformed at room temperature. Likewise, we imaged the dislocation networks shown in Figs. 45 and 46 using weak-beam techniques; representative micrographs of these two networks are shown in Figs. 47a, b. In the specimen deformed at 623K, where the dislocations were predominantly on the octahedral planes, superpartials could be resolved but exhibited a very small separation (Fig. 47a); however, the specimen deformed at 923K contained dislocations on both the octahedral and the cube planes, with those on the cube planes appearing well separated (Fig. 47b). It should be noted that segments of dislocation J in Fig. 47a that appear relatively well separated may have cross-slipped onto the cube plane after deformation at 623K.

The discontinuous drop in tensile yield strength observed in the temperature range 623K - 773K implies that less stress is required to initiate slip above 623K than at lower temperatures, possibly because of the activation of new slip systems (for example, cube slip at higher temperatures), removal of obstacles to dislocation motion, such as precipitates, or lowering of the friction stress. The role of dissolution of precipitates in this observed decrease in strength has been discounted based on direct TEM observations, as well as a differential scanning calorimetry study that showed no reaction at these temperatures. The presence of several dislocations on cube planes at 923K and not at 623K suggests that thermally activated cross-slip from octahedral to cube planes occurred at the higher temperature and that the observed decrease in yield strength might be due to cube slip.

Dislocation interactions with grain boundaries in the specimens deformed at 298K, 623K, and 923K are shown in Figs. 48a-f. In the 298K material, dislocations lie in a slip band, similar to those observed previously (Figs. 43 and 44) but less densely packed on the slip planes, as would be expected in locations not adjacent to the fracture region (Fig. 48a). Further, from Figs. 48b and 48c (conditions of **+g** and **-g**), it appears that dislocations arriving at grain boundaries are unable to cross it to move into the adjacent grain, causing a pile-up in the first grain. Some dislocations, however, do enter the grain boundary. The presence of a dipole is also noted from these two figures (Figs. 48b, c). The 623K material (Fig. 48d) shows dislocation emission into a grain from the grain boundary; thus, at this temperature, dislocation transfer from one grain to another across a grain boundary may not be a limitation. Figures 48e, f, for the 923K material, show dislocation arrival at a grain boundary, absorption into the boundary, and emission into the adjacent grain immediately across (Fig. 48e) or at a different location (Fig. 48f) along the grain boundary, implying successful slip transfer across grain boundaries.

The interaction of lattice dislocations with a grain boundary, transfer of these dislocations to the adjacent grain, and stress relief in the first grain, as well as at the grain boundary, are relevant to the deformation behavior of these materials, particularly at lower temperatures. Commonly, when a lattice dislocation impinges on a grain boundary, it reorients and is incorporated into the grain boundary. Such a dislocation can retain its integrity or dissociate into perfect or partial grain-boundary dislocations. (32) The dislocations that follow can also be absorbed into the grain boundary, but the ease of absorption will depend on the mobility of the grain-boundary dislocations. At low temperatures, grain-boundary dislocations can move on the grain-boundary plane, but only if the plane is an accepted slip plane for them. At higher temperatures, glide and climb combinations allow higher dislocation mobility. Thus, at lower temperatures, a stress concentration develops at the grain boundaries. Eventually, back stress due to the immobility of grain-boundary dislocations will prevent matrix dislocations from entering the boundary, causing a pile-up in the matrix and progressively decreasing the mobility of oncoming dislocations. Meanwhile, at the grain boundary, the stress concentration can be relieved by emission of dislocations from such sources as ledges into the adjacent grain or by propagation of an intergranular crack. In this study, both the fractured foil, and to a lesser extent the foil obtained from the deformed 298K tensile specimen, showed evidence of dislocation pile-up on the slip planes, likely due to the difficulty these dislocations encounter in transferring to the adjacent grain. Clearly, the ease with which dislocations move from one grain to another depends on the type of grain boundary they must cross. Without a statistical evaluation of the various boundaries in the deformed specimen, it is not possible to unequivocally say that dislocation mobility in our samples was grain-boundary-limited at 298K. However, it is evident that there were several boundaries at 298K which were able to absorb but unable to emit dislocations readily into the adjacent grain, thereby causing a pile-up in the first grain. The result is rapid work-hardening, an increase in flow stress exceeding that necessary for cleavage, and thus low ductility. At higher temperatures (473K and 623K), even though the material work-hardened rapidly in the initial stages (comparable to the hardening at 298K in the 0.02% to 0.1% strain regime), the subsequent rate dropped, presumably due to some dislocation emission from grain boundaries into adjacent grains (Fig. 48d).

Bond, Robertson, and Birnbaum (33) showed by ambient-temperature in-situ straining experiments in the TEM that grain boundaries in $L1_2$ Ni_3Al act as effective barriers to dislocation motion, absorbing but not emitting dislocations into the adjacent grain. Eventually, in that case, grain-boundary strain was relieved by grain-boundary failure. From similar experiments on this material, however, Baker, Schulson, and Horton (34) concluded that pile-ups at grain boundaries could initiate slip in the adjacent grain, and that cracking in thin foils occurred mainly along slip bands. Nevertheless, they determined that even though the crack followed a transgranular path in the thin regions of the foil, final fracture in the thicker regions was completely intergranular.

The decrease in mobility of the matrix dislocations caused by dislocation tangling and pile-ups at the grain boundary provides an opportunity for solute atmospheres to diffuse to the dislocations and pin them. Pinning further decreases their mobility so that a higher stress is needed to move them. The development of this plastic instability (serrated flow) from ~ 623K to ~800K coincides with the observed decrease in ductility from 1.3% at 623K to ~0.3% at 773K, and the two are likely related.

There are, however, other factors that can cause a decrease in intermediate-temperature ductility, a characteristic of other $L1_2$ compounds such as Ni_3Al and Co_3Ti.(6, 35) In Ni_3Al, this behavior is attributed to dynamic oxygen embrittlement, (36) where atomic bonds weakened by oxygen chemisorption, together with stress concentration at grain boundaries, cause grain-boundary microcracking. The overall decrease in ductility is attributed to continuous embrittlement of fresh crack tips and propagation of the crack along the boundary. Taub, Chang, and Liu (37) compared the high-temperature properties of rapidly solidified boron-doped Ni_3Al with those of conventionally cast and processed material and suggested that the internal oxygen level might influence the high-temperature ductility. It is possible that similar mechanisms were operative in our study, particularly since the oxygen level in $Al_{66}Ti_{25}Mn_9$ was high (Table IV).

Even though the ductility minimum was observed at 773K, small amounts of intergranular fracture were observed at temperatures as low as 473K. At this temperature, fracture was predominantly transgranular cleavage, but the intergranular failure is typically observed at the periphery of the fracture surface (Fig. 49a), lending some credibility to the embrittlement theory. Initial intergranular failure leads to a reduction in cross-sectional area and overload failure by cleavage when the critical stress level is exceeded. A higher magnification micrograph (Fig. 49b) shows secondary microcracks along grain boundaries. It is possible that the kinetics of chemisorption is a maximum around 773K, leading to a ductility minimum. The recovery in ductility at higher temperatures may then be attributed to a combination of possible dynamic recrystallization and enhancement of slip transfer across grains. It must be emphasized that even though ductility improves at higher temperatures, grain-boundary failure persists for all temperatures considered in this study. This outcome reflects the characteristic intrinsic weakness of $L1_2$ grain boundaries and/or the inability of these boundaries to emit dislocations at the same rate they absorb them, leading to a stress concentration at the boundary.

Finally, the most extensively studied compound with respect to intergranular fracture in $L1_2$ materials is Ni_3Al with and without boron additions. George and Liu (13) recently reviewed the various theories proposed to explain this grain-boundary failure, including such arguments as electronegativity differences between constituent atoms, (38) fewer permissible dislocation reactions at grain boundaries which could maintain chemical order, (39) and the presence of columns of atomic size cavities in the boundary structure which act as nuclei for intergranular cracks. (40)

These theories, however, seem unable to explain the behavior of Co_3Ti, a strongly ordered $L1_2$ compound which exhibits ductile transgranular failure at ambient and warm temperatures. (6) Takasugi and Izumi (6, 41) claim that an $L1_2$ compound of two atoms that are similar electrochemically, such as Co and Ti, shows less heteropolarity in the bonding environment in the grain-boundary region, resulting in enhanced grain-boundary strength. In contrast, a compound between a transition atom in the A-group and an atom in the B-subgroup of the periodic table, such as Ni and Al, produces strong covalent-like bonding that results in severe grain-boundary embrittlement. Whether this observation is valid or not remains to be verified with more case studies. Such an argument could explain the observation of intergranular fracture at warm temperatures in the $L1_2$ trialuminides in this study, whereas the cleavage failure at ambient can be argued on the basis of an intrinsically low cleavage strength, (12) lower than the grain-boundary strength. In the ternary $L1_2$ trialuminide $Al_{66}Ti_{25}Mn_9$, the three constituents correspond to group III B (Al), group IV A (Ti), and group VII A (Mn). Based on the concepts of Takasugi and Izumi, (6) this ternary compound likely exhibits less covalency than a binary $L1_2$ compound, such as Al_3Sc, because the effect in the ternary is tempered by the presence of ~10 at.% Mn. Unfortunately, a direct comparison between the binary Al_3Ti and our ternary $L1_2$ compound is not possible because the $L1_2$ structure is destabilized in favor of the DO_{22} structure in that compound.

Takasugi, Izumi, and Masahashi (42) examined the effect of ternary additions to Ni_3Al on electronic structure changes and fracture behavior. They observed that additions such as Mn and Fe, which have bonding characteristics similar to those of Ni, improved the grain-boundary strength when substituted in the Al site. As a consequence, they proposed that a positive valency difference between the third element and the solvent atom it replaces would enhance grain-boundary strength. An analogous experiment in our study would be substitution of quaternary additions that satisfy the above valency requirement, although at present, there is no conclusive evidence even in the ternary system that Mn preferentially occupies either sublattice exclusively.

G. CTE MEASUREMENTS

Specimens for CTE measurements were electrodischarge-machined from both the I/M forgings and the P/M-processed monolithic and composite materials. Results obtained are summarized in Figs. 50a-e.

These figures lead to the following observations:

1) The addition of 20 vol.% TiB_2 particulates to $Al_{22}Fe_3Ti_8$ + 2Nb decreases the CTE by about 2 ppm/°C in the temperature range 100°C to 900°C (the expected maximum-use temperature range for these materials).

2) A comparison of the two composites, $Al_{22}Fe_3Ti_8$ + 20 vol.%TiB_2 and $Al_{22}Fe_3Ti_8$ + 2Nb + 20 vol.% TiB_2, suggests that the addition of 2Nb does not influence the CTE of the ternary intermetallic $Al_{22}Fe_3Ti_8$.

3) The CTE of the monolithic $Al_{66}Mn_9Ti_{25}$ is higher than that of $Al_{22}Fe_3Ti_8$ + 2Nb. Furthermore, based on the previous observations, it follows that the CTE of the monolithic $L1_2$ compound of the Al-Ti-Mn system is higher than that of its Al-Ti-Fe counterpart.

VI. SUMMARY AND ISSUES

A. HIGHLIGHTS

- In the ternary Al-Ti-Fe system, the mechanical properties of the multiphase $L1_2$ compound $Al_{22}Fe_3Ti_8$ did not depend on stoichiometry; further, minor quaternary additions did not significantly influence the high-temperature strength, particularly at slow strain rates.

- Typically, very high matrix strength was observed in compression, and was retained up to ~1000K, where it underwent a steep drop. This was attributed to the dissolution of the minor phases.

- The stress exponent at 1100K and 1200K was ~3.0 for the monolithic materials; for the 20 vol.% TiB_2 composites, the exponent was ~4.8, indicating that the composite would be stronger than the monolithic form at slow strain rates.

- Depending on stoichiometry, the Fe-based $L1_2$ compound frequently exhibited brittle fracture in compression at intermediate and low temperatures (<673K); the Cr- and Mn-based compounds yielded at all temperatures, including cryogenic temperatures.

- The P/M versions of the Cr- and Mn-based $L1_2$ compounds were at least twice as strong as their I/M counterparts, and this superiority in strength was retained up to ~1100K.

- Both the Cr- and Mn-based compounds exhibited excellent forgeability (isothermal forgings), with the Mn-based compound the better of the two.

- Three-point bend tests showed reproducible, finite, ambient plastic deformation for the Mn-based intermetallic, but not for the Cr-based $L1_2$ compound in this study.

- Tensile tests on forged $Al_{66}Ti_{25}Mn_9$ revealed:
  - A discontinuous drop in strength in tension in the temperature range 623K - 773K, attributed to the onset of cube slip
  - Serrated flow in the warm-temperature range, approximately 600K-800K
  - A finite (0.2%) amount of plastic tensile deformation at ambient temperature, increasing to 1.3% at 623K
  - A ductility minimum at 773K, followed by a ductility increase to 5% at 1073K, which is attributed to enhanced slip transfer across boundaries and possibly due to some stress relief by dynamic recrystallization
  - Fracture transitions from transgranular cleavage at ambient to a mixed cleavage plus intergranular failure at 623K to a predominantly intergranular mode at 923K and higher. However, the transition in fracture morphology was not coincident with the observed ductility - temperature profile.
- TiB_2 particulate reinforcement was beneficial in two ways: 1) it decreased the CTE of the composite relative to that of the matrix material, and 2) it significantly improved ambient- and warm-temperature strengths.
- High-temperature strength (>1000K) was not increased by particulate reinforcement; rather, at fast strain rates, the composite was weaker. At slow strain rates, the composites regained their superiority.
- Bend test results indicated that a high volume fraction of reinforcement (20% TiB_2) can lower the brittle-to-ductile transition temperature; it is not clear why this happens and more tests are needed to confirm this observation.

B. CRITICAL ISSUES

- Further improvements are needed in high-temperature strength retention and low-temperature (~298K) ductility and toughness.
- Particulate reinforcement does not enhance the useful temperature range of the monolithic material; rather, it increases the strength over the low- and intermediate-temperature ranges.
- The $L1_2$ compounds containing Fe as the third element are very strong at low and warm temperatures but do not appear to be ductile or tough.
- The Cr- and Mn-based $L1_2$ compounds exhibit excellent forgeability; the Mn-based compound appears more forgiving than the Cr-based intermetallic in terms of ductility.
- The three different $L1_2$ compounds exhibit high strength, oxidation resistance, or potential ductility, but no one compound offers all three. All three compounds lose strength above ~1100K.

VII. REFERENCES

1. K.S. Kumar and J.R. Pickens, Scr. Metall., 22, 1988, p. 1015.

2. M.B. Winnicka and R.A. Varin, Scr. Metall., 23, 1989, p. 1199.

3. H. Mabuchi, K. Hirukawa, H. Tsuda and Y. Nakayama, Scr. Metall. Mater., 24, 1990, p. 505.

4. S. Zhang, J.P. Nic, W.W. Mulligan, and D.E Mikkola, Scr. Metall. Mater., 24, 1990, p. 1441.

5. Y. Mishima, Y. Oya, and T. Suzuki, in High Temperature Ordered Intermetallic Alloys I (editors: C.C. Koch, C.T. Liu and N.S. Stoloff), Vol. 39, Materials Research Society, Pittsburgh, PA, 1985, p. 263.

6. T. Takasugi and O. Izumi, Acta Metall., 33, 1985, p. 39.

7. W.O. Powers, J.A. Wert, and C.D. Turner, Philos. Mag. A., 60, 1989, p. 227.

8. C.D. Turner, W.O. Powers, and J.A. West, Acta Metall., 37, 1989, p. 2635.

9. V.K. Vasudevan, R. Wheeler, and H.L. Fraser, in High Temperature Ordered Intermetallic Alloys III (editors: C.T. Liu, A.I. Taub, N.S. Stoloff and C.C. Koch), Vol. 133, Materials Research Society, Pittsburgh, PA, 1989, p. 705.

10. M.J. Marcinkowski, Phys. Stat. Sol. (a), 90, 1985, p. 621.

11. J.H. Schneibel and E.P. George, Scr. Metall. Mater., 24, 1990, p. 1069.

12. E.P. George, J.A. Horton, W.D. Porter, and J.H. Schneibel, J. Mater. Res., 5, 1990, p. 1639.

13. E.P. George and C.T. Liu in Alloy Phase Stability and Design (editors: G.M. Stocks, D.P. Pope and A.F. Giamei), Vol. 186, Materials Research Society, Pittsburgh, PA, 1990.

14. C.L. Fu, J. Mater. Res., 5, 1990, p. 971.

15. J.D. Whittenberger, D.J. Gaydosh, and K.S. Kumar, J. Mater. Sci., 25, 1990,

p. 2771.

16. J.D. Whittenberger, in Solid State Powder Processing (editors: A.H. Clauer and J.J. deBarbadillo), The Minerals, Metals and Materials Society, Warrendale, PA, 1990, p. 137.

17. N.S. Stoloff and D.E. Alman, Int. J. Powder Metall., 1990, submitted.

18. A.R.C. Westwood, Metall. Trans. A, 19A, 1988, p. 749.

19. J.D. Whittenberger, R.K. Viswanadham, S.K. Mannan, and B. Sprissler, J. Mater. Sci., 25, 1990, p. 35.

20. K.S. Kumar, S.K. Mannan, J.D. Whittenberger, R.K. Viswanadham, and L. Christodoulou, Final Report to the Office of Naval Research, MML TR 89-102(c), Martin Marietta Laboratories, Baltimore, MD, Nov. 1989, pp. 8, 25.

21. S.K. Mannan, K.S. Kumar, and J.D. Whittenberger, Metall. Trans. A, 21A, 1990, p. 2179.

22. P.R. Strutt and B.H. Kear, in High Temperature Ordered Intermetallic Alloys I (editors: C.C. Koch, C.T. Liu, and N.S. Stoloff), Vol. 39, Materials Research Society, Pittsburgh, PA, 1985, p. 279.

23. J.D. Whittenberger, R.K. Viswanadham, S.K. Mannan, and K.S. Kumar, J. Mater. Res., 4, 1989, p. 1164.

24. L. Christodoulou, P.A. Parrish, and C.R. Crowe, in High Temperature, High Performance Composites (editors: F.D. Lemkey, S.G. Fishman, A.G. Evans, and J.R. Strife), Vol. 120, Materials Research Society, Pittsburgh, PA, 1988. p. 29.

25. S.L. Kampe, J.A. Clarke, and L. Christodoulou, in Intermetallic Matrix Composites (editors: D.L. Anton, P.L. Martin, D.G. Miracle, and R. McMeeking), Vol. 194, Materials Research Society, Pittsburgh, PA., 1990, p. 225.

26. J.D. Whittenberger, Mater. Sci. Eng., 57, 1983, p. 77.

27. A. Seibold, Z. Metall., 72, 1981, p. 712.

28. V. Ya. Markiv, V.V. Burnashova, and V.P. Ryabov, Akad. Nauk. Ukr. SSR, Metallofizika, 46, 1973, p. 103.

29. S. Mazdiyasni, D.B. Miracle, D.M. Dimiduk, M.G. Mendiratta, and P.R. Subramanian, Scr. Metall., 23, 1989, p. 327.

30. G.R. Edwards, T.R. McNelley, and O.D. Sherby, Philos. Mag., 32, 1975, p. 1245.

31. K.S. Kumar and R.A. Herring, Scr. Metall. Mater., 24, 1990 p. 1713.

32. T.C. Lee, I.M. Robertson, and H.K. Birnbaum, Philos. Mag. A, 62, 1990, p. 131.

33. G.M. Bond, I.M. Robertson, and H.K. Birnbaum, J. Mater. Res., 2, 1987, p. 436.

34. I. Baker. E. M. Schulson, and J.A. Horton, Acta Metall., 35, 1987, p. 1533.

35. C.T. Liu, in High Temperature Ordered Intermetallic Alloys II (editors: N.S. Stoloff, C.C. Koch, C.T. Liu, and O. Izumi), Vol. 81, Materials Research Society, Pittsburgh, PA, 1987, p. 355.

36. C.T. Liu and C.L. White, Acta Metall., 35, 1987, p. 643.

37. A.I. Taub, K.-M. Chang, and C.T. Liu, Scr. Metall., 20, 1986, p. 1613.

38. A.E. Taub and C.L. Briant, Acta Metall., 35, 1987, p. 1597.

39. A.H. King and M.H. Yoo, in High Temperature Ordered Intermetallic Alloys II (editors: N.S. Stoloff, C.C. Koch, C.T. Liu, and O. Izumi), Vol. 81, Materials Research Society, Pittsburgh, PA, 1987, p. 99.

40. J.J. Kruisman, V. Vitek, and J. Th.M. DeHosson, Acta Metall., 36, 1988, p. 2729.

41. T. Takasugi and O. Izumi, Acta Metall., 33, 1985, p. 1247.

42. T. Takasugi, O. Izumi, and N. Masahashi, Acta Metall., 33, 1985, p. 1259.

APPENDIX A

MATRIX COMPOSITIONS AND TiB_2 VOLUME FRACTIONS FOR $L1_2$ MODIFIED TRIALUMINIDES.

Compositions of the matrices and volume fraction of TiB_2 particles for the various $L1_2$ modified trialuminides whose chemistries are reported in Table II have been calculated with the following methods and assumptions:

1. The reported chemistries (Table II) are accurate and were normalized to 100%. The failure of the summation of the measured chemistries to equal 100% is the result of insoluble oxide phases.
2. All B is in the form of TiB_2.
3. The density of all $L1_2$ modified trialuminides, irrespective of their actual compositions, is assumed to be 3.83 Mg/m^3, while the density of TiB_2 is 4.5 Mg/m^3.

The calculated matrix compositions in atom percent and volume fraction of TiB_2 for the various $L1_2$ modified trialuminides are given in Table A-I.

Table A-I Calculated Matrix Compositions and Volume Fractions of TiB_2 for Monolithic and Composite Materials Produced via the P/M Route

	Matrix Atomic Percent						Volume Fraction TiB_2, %
	Al	Ti	Fe	Cr	Mn	Nb	
Al-Ti-Fe	64.9	28.3	6.8				--
Al-Ti-Fe + 5 vol.% TiB_2	63.0	30.5	6.5				3.5
Al-Ti-Fe + 10 vol.% TiB_2	63.1	30.5	6.4				9.8
Al-Ti-Fe + 20 vol.% TiB_2	61.3	32.3	6.3				19.3
Al-Ti-Fe(+2 at.% Mn)	61.2	30.5	6.4		1.95		--
Al-Ti-Fe(+2 at.% Mn) + 5 vol.% TiB_2	60.3	31.7	6.1		1.9		3.4
Al-Ti-Fe(+2 at.% Mn) + 10 vol.% TiB_2	60.7	31.1	6.2		2.0		8.8
Al-Ti-Fe(+2 at.% Mn) + 20 vol.% TiB_2	60.7	31.1	6.2		2.0		19.2
Al-Ti-Fe(+2 at.% Nb)	63.4	28.2	6.5			1.8	--
Al-Ti-Fe(+2 at.% Nb) + 5 vol.% TiB_2	63.0	28.5	6.6			1.9	4.4
Al-Ti-Fe(+2 at.% Nb) + 10 vol.% TiB_2							
XD synthesis	60.0	28.6	6.5			1.9	8.3
Mechanically alloyed	65.3	25.7	7.1			1.9	11.8
Al-Ti-Fe(+2 at.% Nb) + 20 vol.% TiB_2	60.9	30.0	6.9			2.2	19.6
Al-Ti-Fe (higher Fe, lower Ti)	62.1	28.3	9.6				--
Al-Ti-Fe (higher Fe, lower Ti) + 20 vol.% TiB_2	67.2	22.6	10.6				20.5
Al-Ti-Cr	64.1	27.2		8.7			--
Al-Ti-Cr + 20 vol.% TiB_2	65.0	27.2		7.8			22.2
Al-Ti-Mn	62.6	27.4			10.0		--
Al-Ti-Mn + 20 vol.% TiB_2	63.7	27.0			9.3		20.0

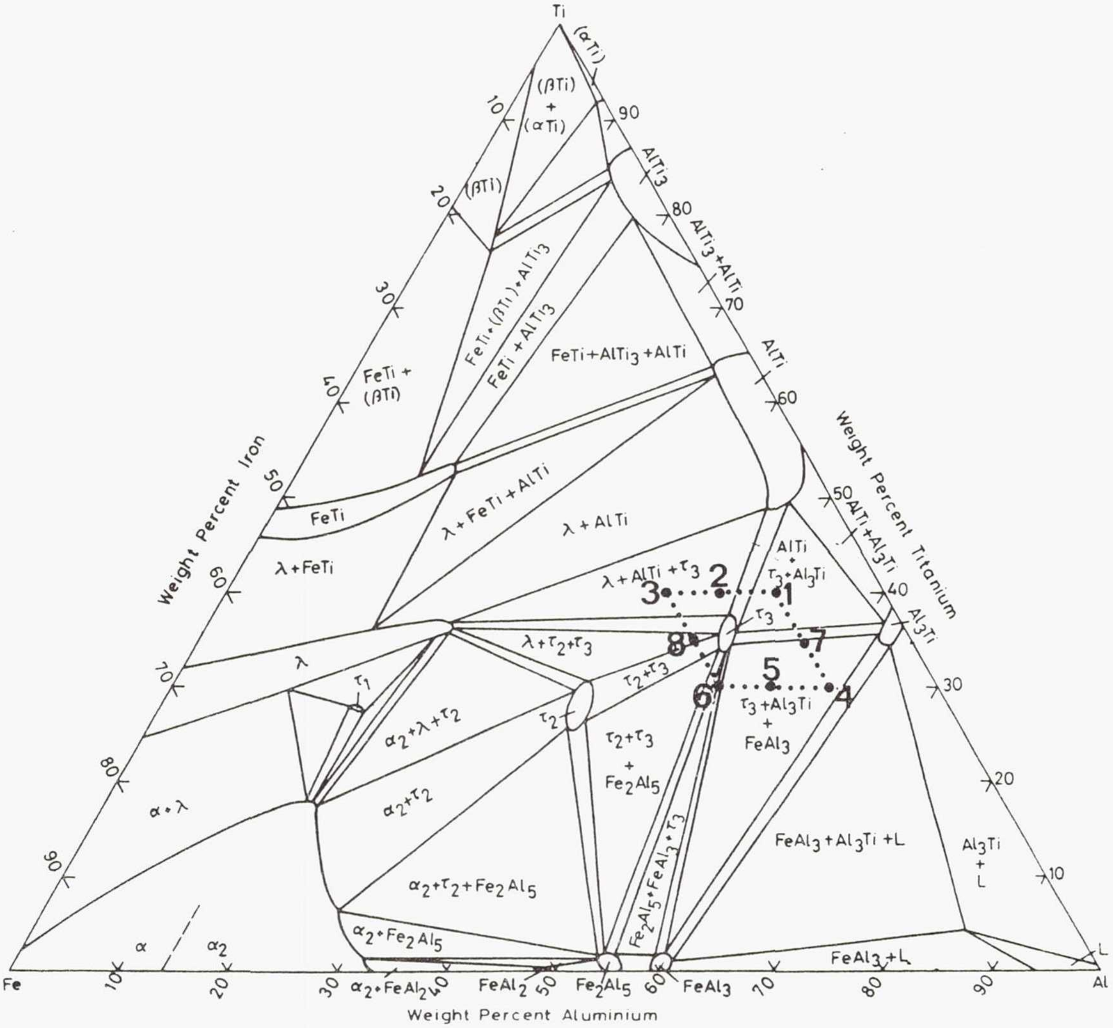

Figure 1. The 1073K isotherm for the ternary Al-Ti-Fe system (27) with the eight compositions selected to verify the extent of the $L1_2$ phase field superimposed.

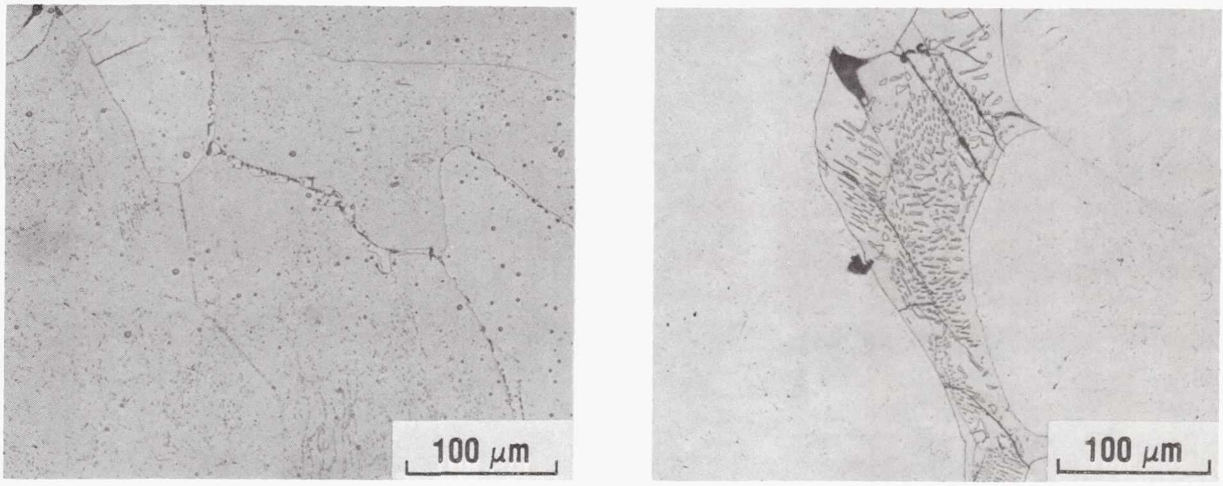

a) Sample # 4

b) Sample # 5

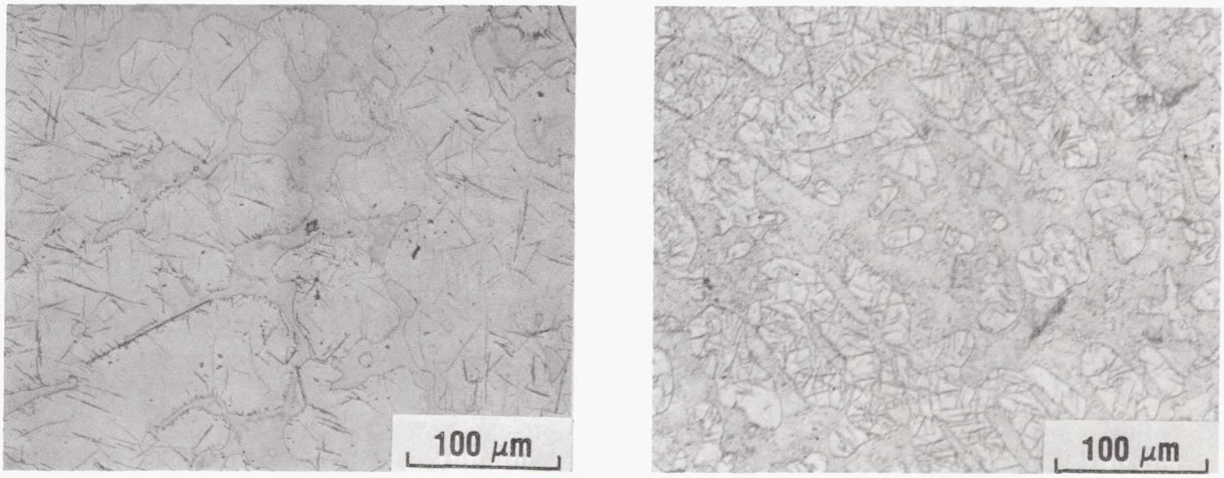

c) Sample #8

d) Sample #3

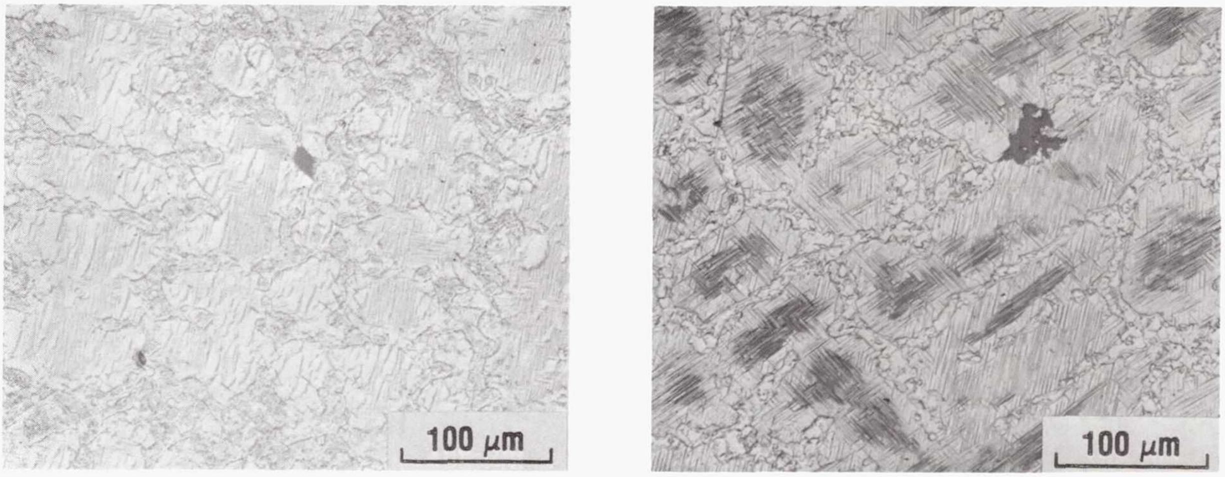

e) Sample #2

f) Sample #2

Figure 2. Representative optical micrographs of the multiphase alloys (Table V) after quenching from 1100K (a-e) and 900K (f): (a) alloy #4, (b) alloy #5, (c) alloy #8, (d) alloy #3, and (e,f) alloy #2.

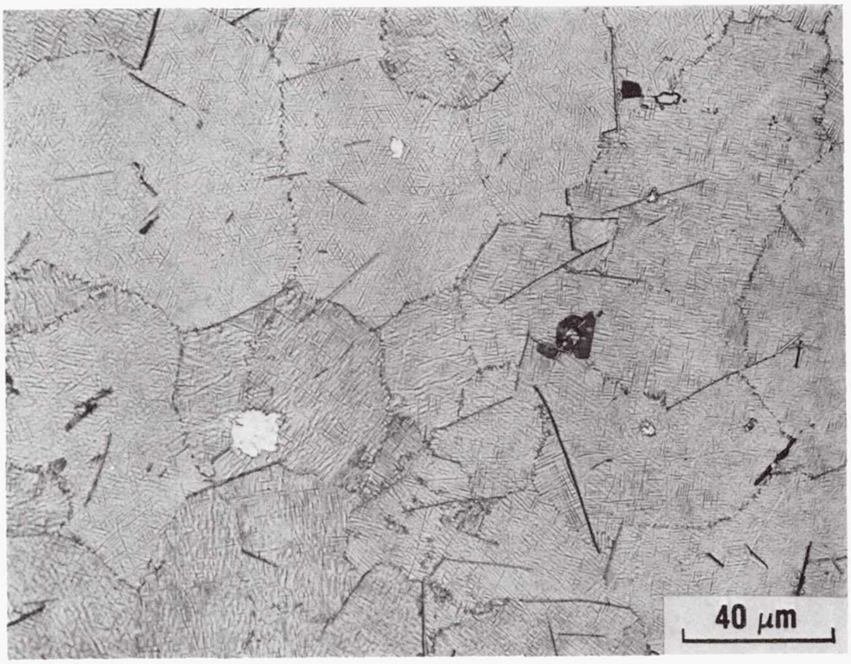

Figure 3. Cast and homogenized (1473K, 5 days) microstructure revealing the presence of minor phases in a 30 at.% Ti, 6.7 at.%Fe alloy.

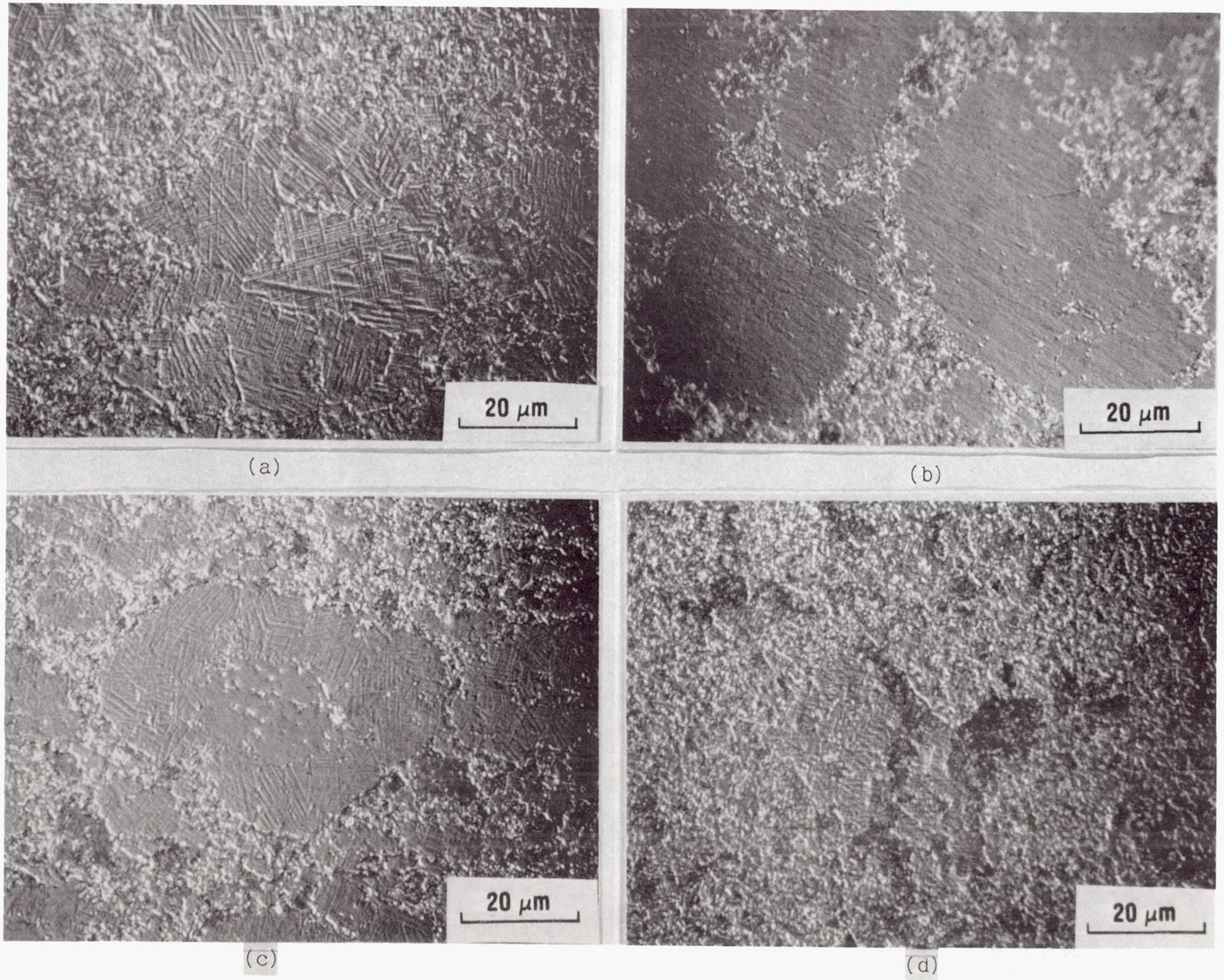

Figure 4. Representative optical micrographs of the hot -pressed monolithic and composite materials: (a) 6.7 at.%Fe, (b) 8.75 at.%Fe, (c) 6.7 at.%Fe + 10 vol.% TiB_2, and (d) 6.7 at.%Fe + 20 vol.% TiB_2.

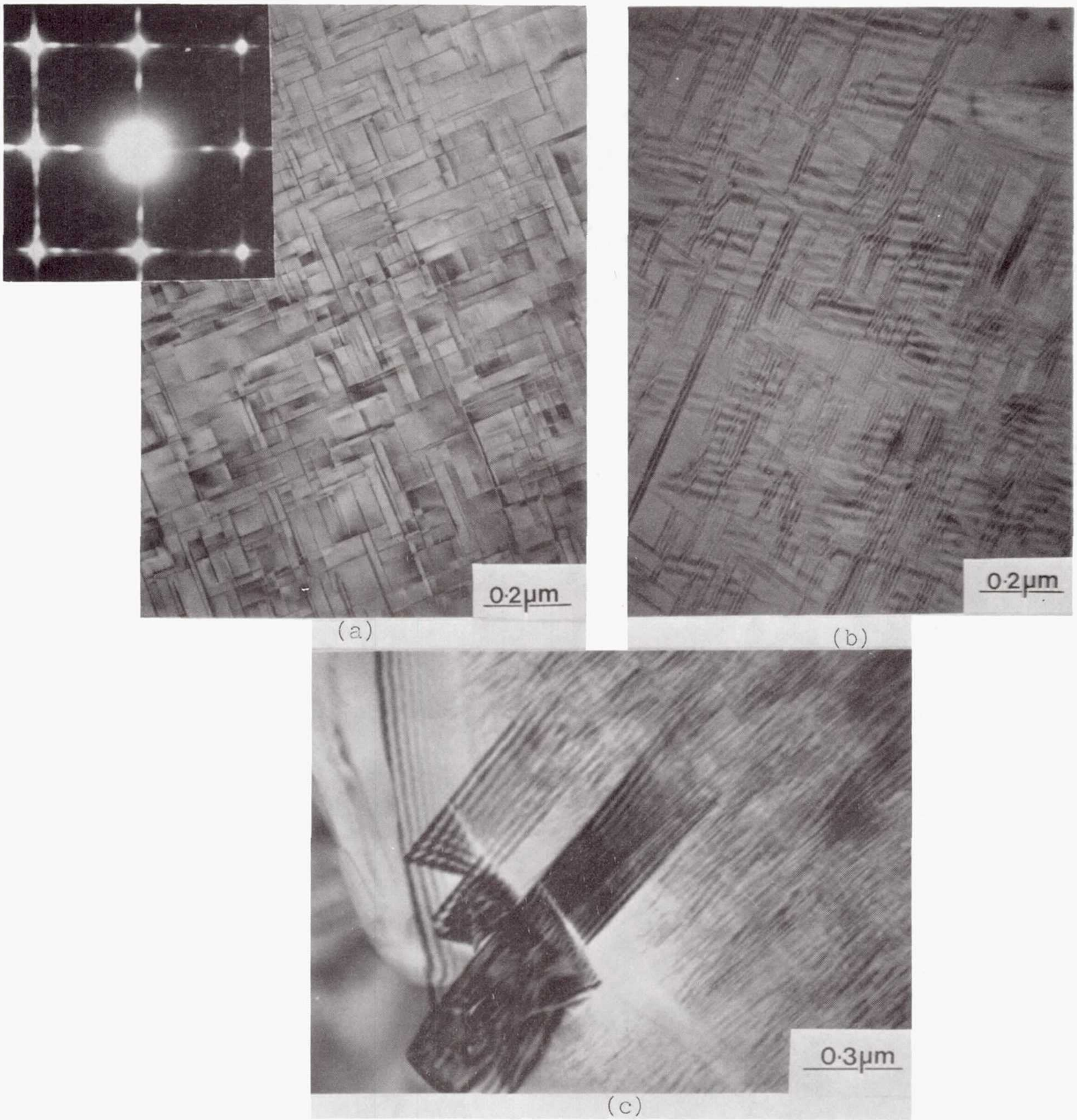

Figure 5. Hot-pressed microstructure of the ternary multiphase monolithic compound Al-Ti-Fe (8.75 at.%Fe): (a) precipitates oriented edge-on; (b) fringe contrast associated with the lath-shaped precipitates lying inclined to the plane of the foil, and (c) lath-shaped precipitates nucleated at a grain boundary.

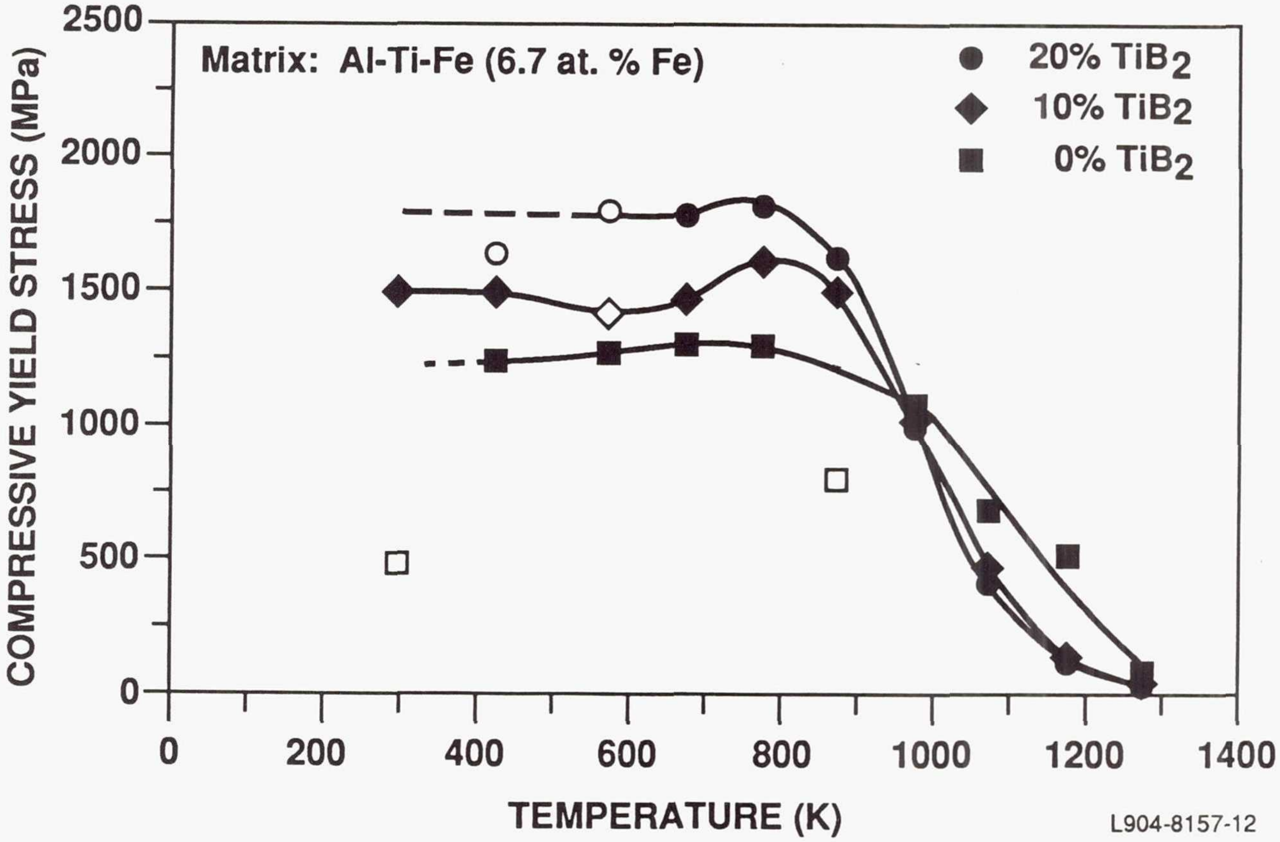

Figure 6. Compressive yield stress versus temperature for monolithic $Al_{22}Fe_3Ti_8$ (6.7 at.%Fe) and with TiB_2 reinforcements (note: open symbols denote failure prior to yield).

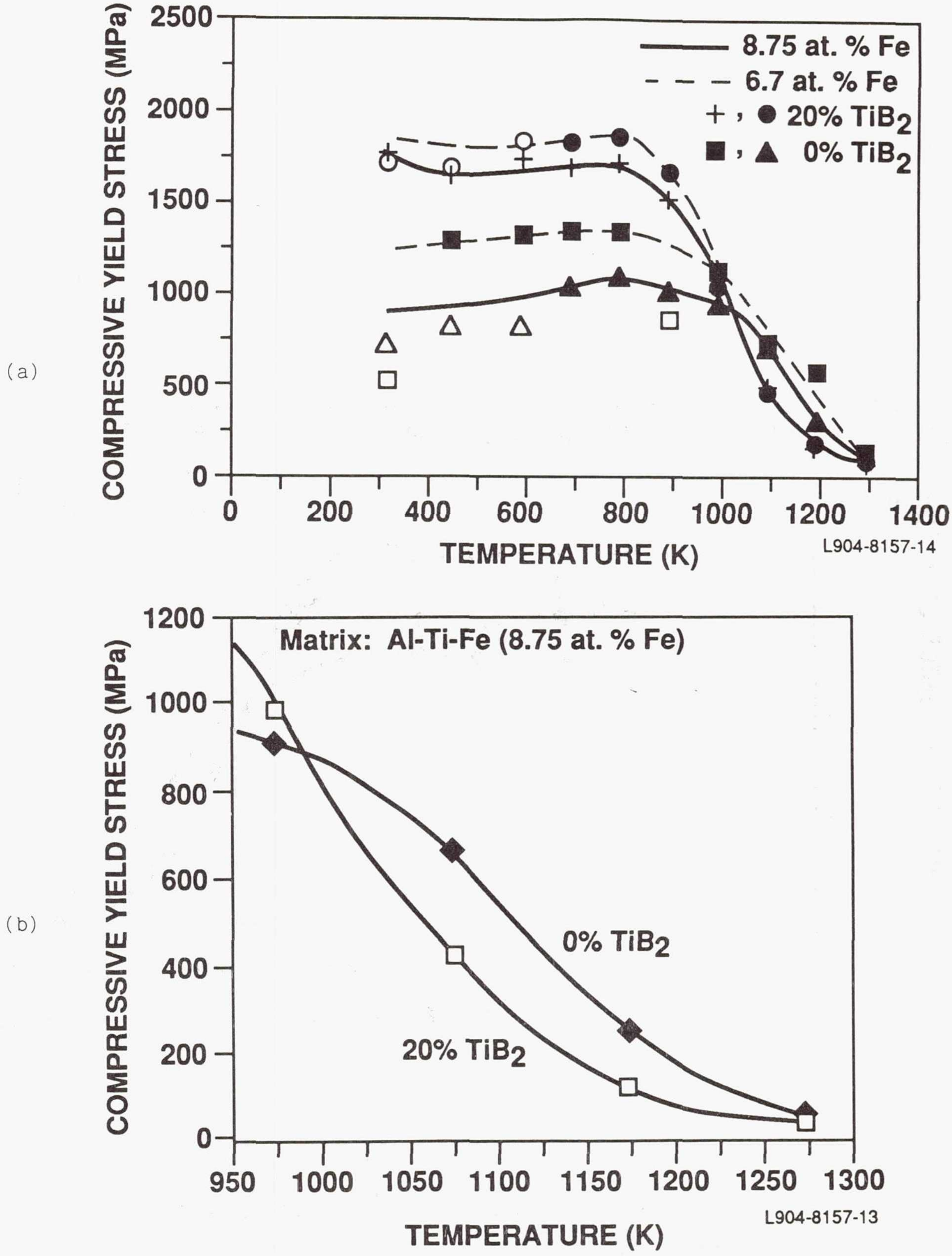

Figure 7. Compressive yield stress versus temperature for (a) monolithic and particulate-reinforced $Al_{22}Fe_3Ti_8$ and (b) an enlargement of the 950K - 1300K region in (a) showing the crossover in strength. (Open symbols denote failure prior to yielding.)

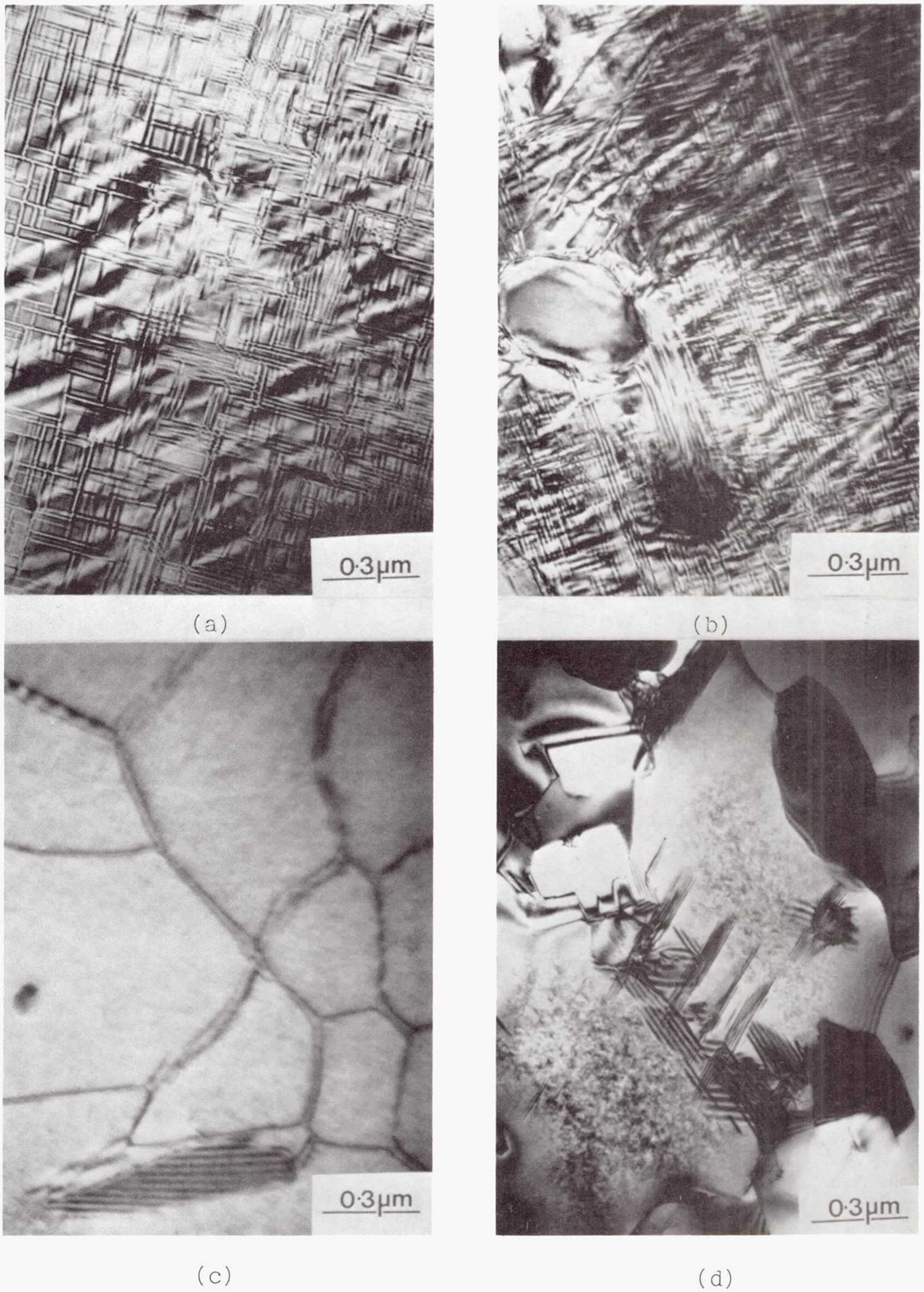

Figure 8. Post-deformation microstructure for the monolithic (a,c) and 20 vol.% TiB_2-containing (b,d) ternary Al-Ti-Fe (8.75 at.%Fe): (a,b) deformed at 773K and (c,d) deformed at 1073K.

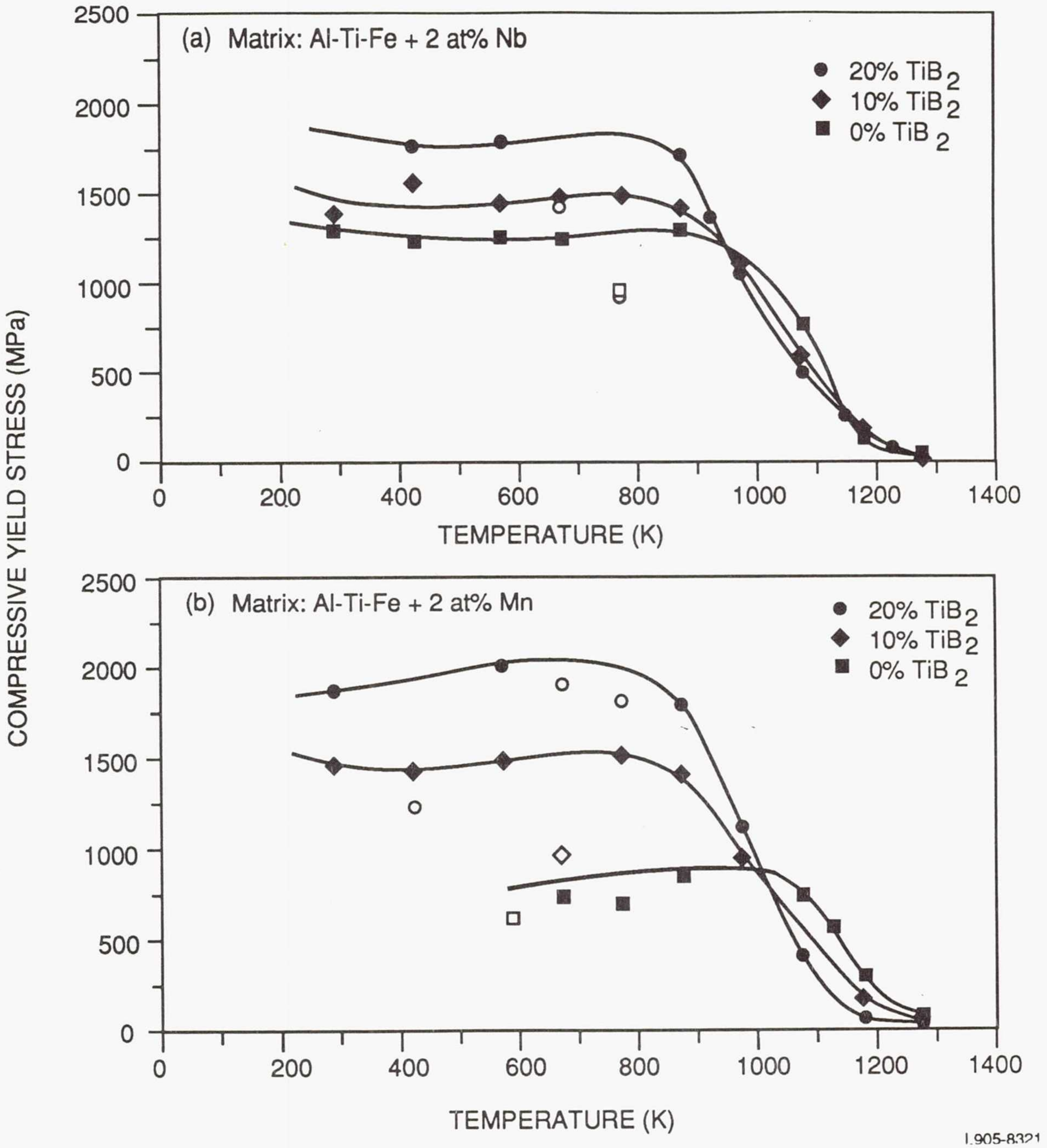

Figure 9. Compressive yield stress versus temperature for quaternary monolithic and composite materials: (a) $Al_{22}Fe_3Ti_8$ (6.7 at.% Fe) + 2Nb and (b) $Al_{22}Fe_3Ti_8$ (6.7 at.% Fe) + 2Mn. (Open symbols denote fracture before yielding.)

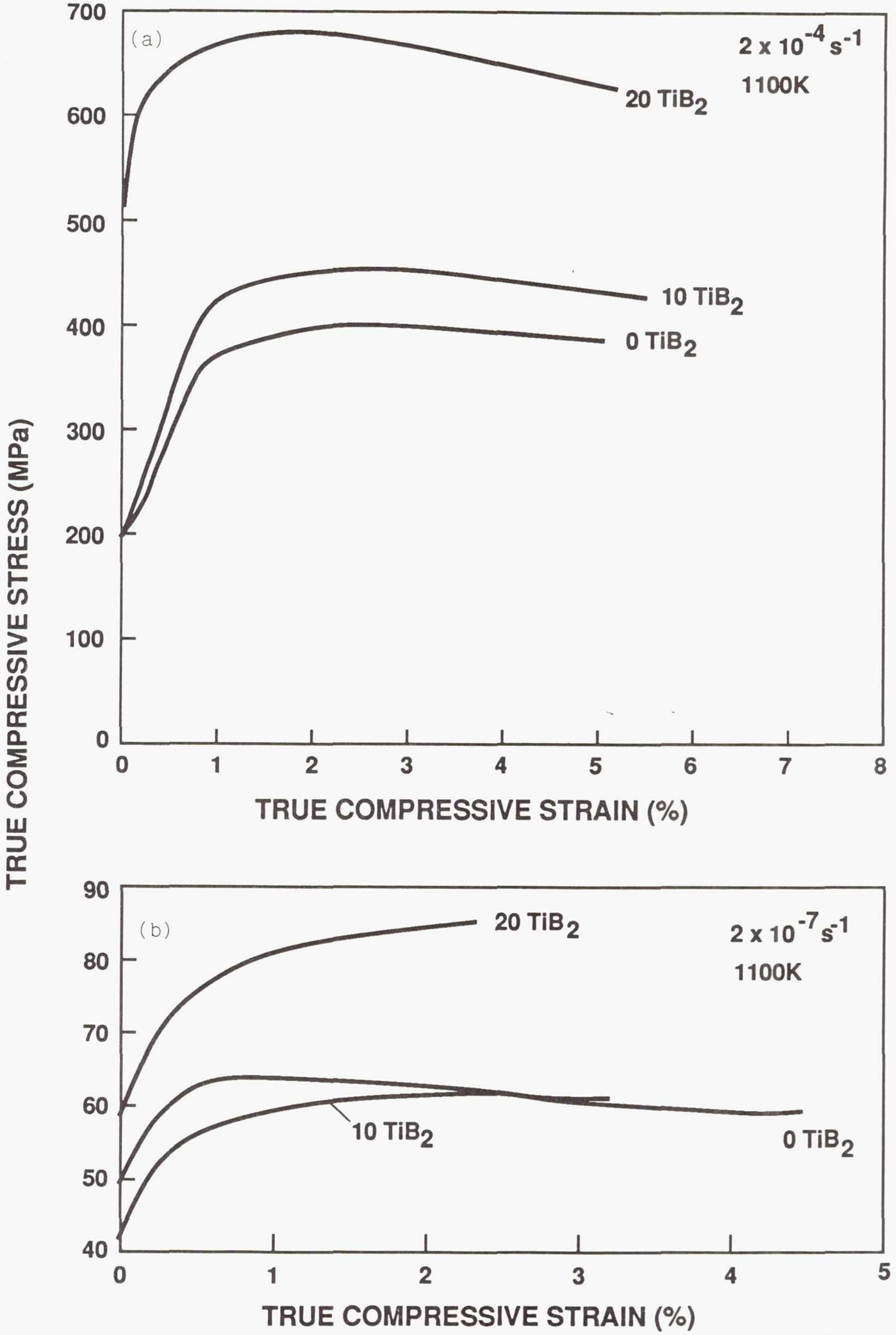

Figure 10. True compressive stress-strain diagrams for monolithic and particulate-reinforced $Al_{22}Fe_3Ti_8$ (6.7 at.%Fe) at 1100K: (a) strain rate = $2x10^{-4}s^{-1}$ and (b) strain rate = $2x10^{-7}s^{-1}$.

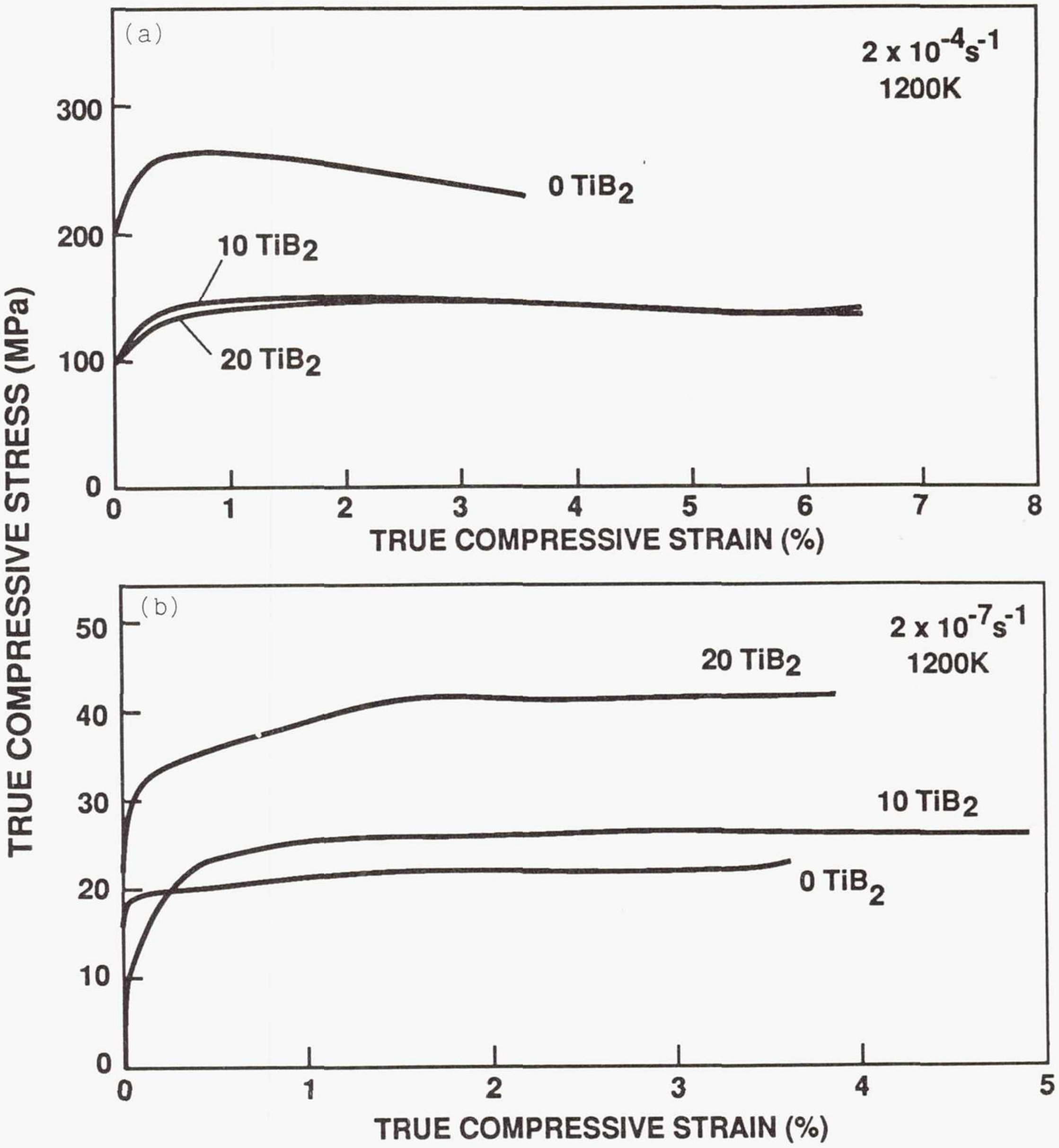

Figure 11. True compressive stress-strain diagrams for monolithic and particulate-reinforced $Al_{22}Fe_3Ti_8$ (6.7 at.%Fe) at 1200K: (a) strain rate = $2x10^{-4}s^{-1}$ and (b) strain rate = $2x10^{-7}s^{-1}$.

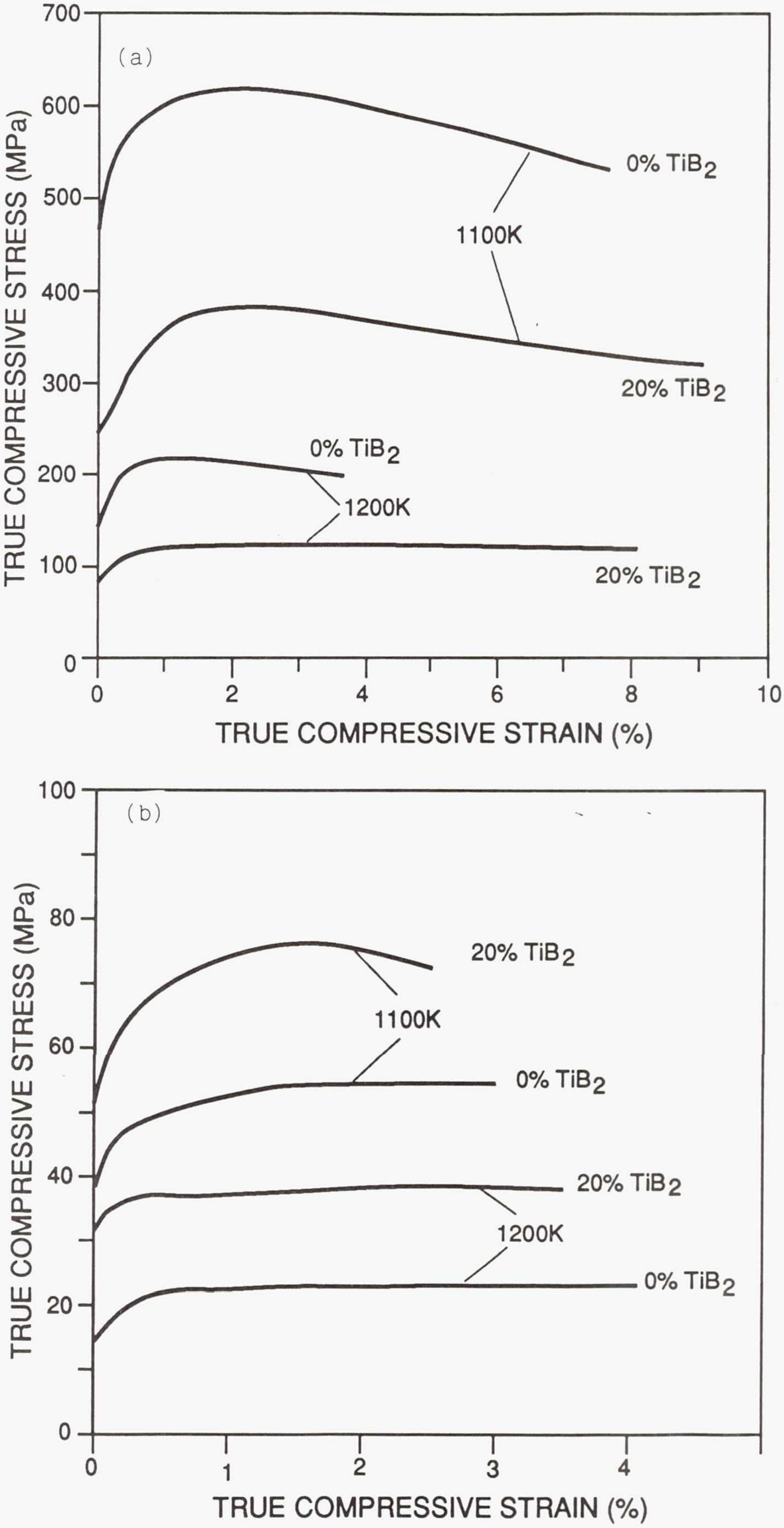

Figure 12. True compressive stress-strain diagrams for monolithic and particulate reinforced $Al_{22}Fe_3Ti_8$ (8.75 at.%Fe) at 1100K and 1200K: (a) strain rate = $2x10^{-4}s^{-1}$ and (b) strain rate = $2x10^{-7}s^{-1}$.

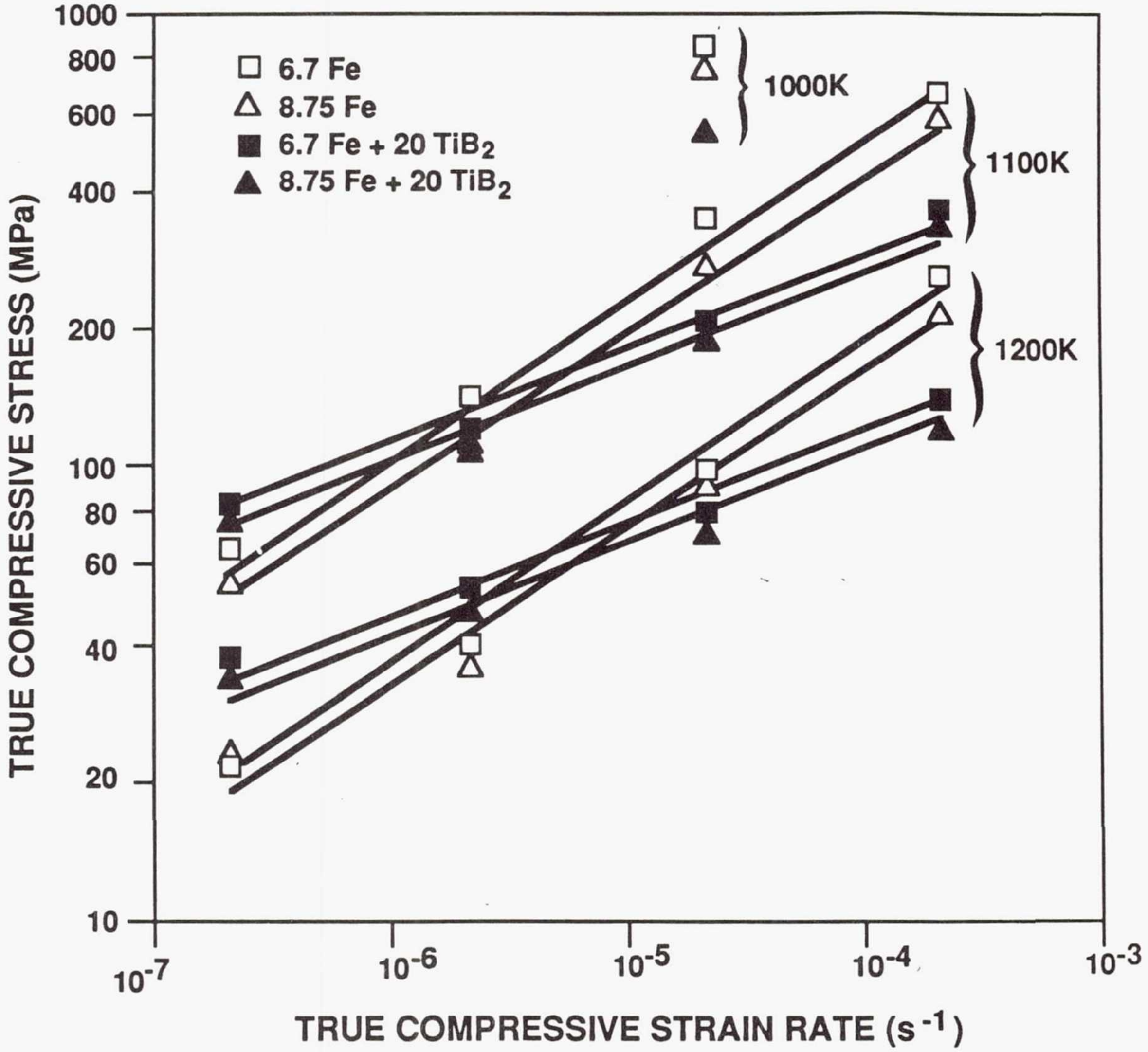

Figure 13. True compressive stress-strain rate behavior at 1000K-1200K for monolithic $Al_{22}Fe_3Ti_8$ (6.7 at.% Fe and 8.75 at.% Fe) and particulate-reinforced composites containing 20 vol.% TiB_2.

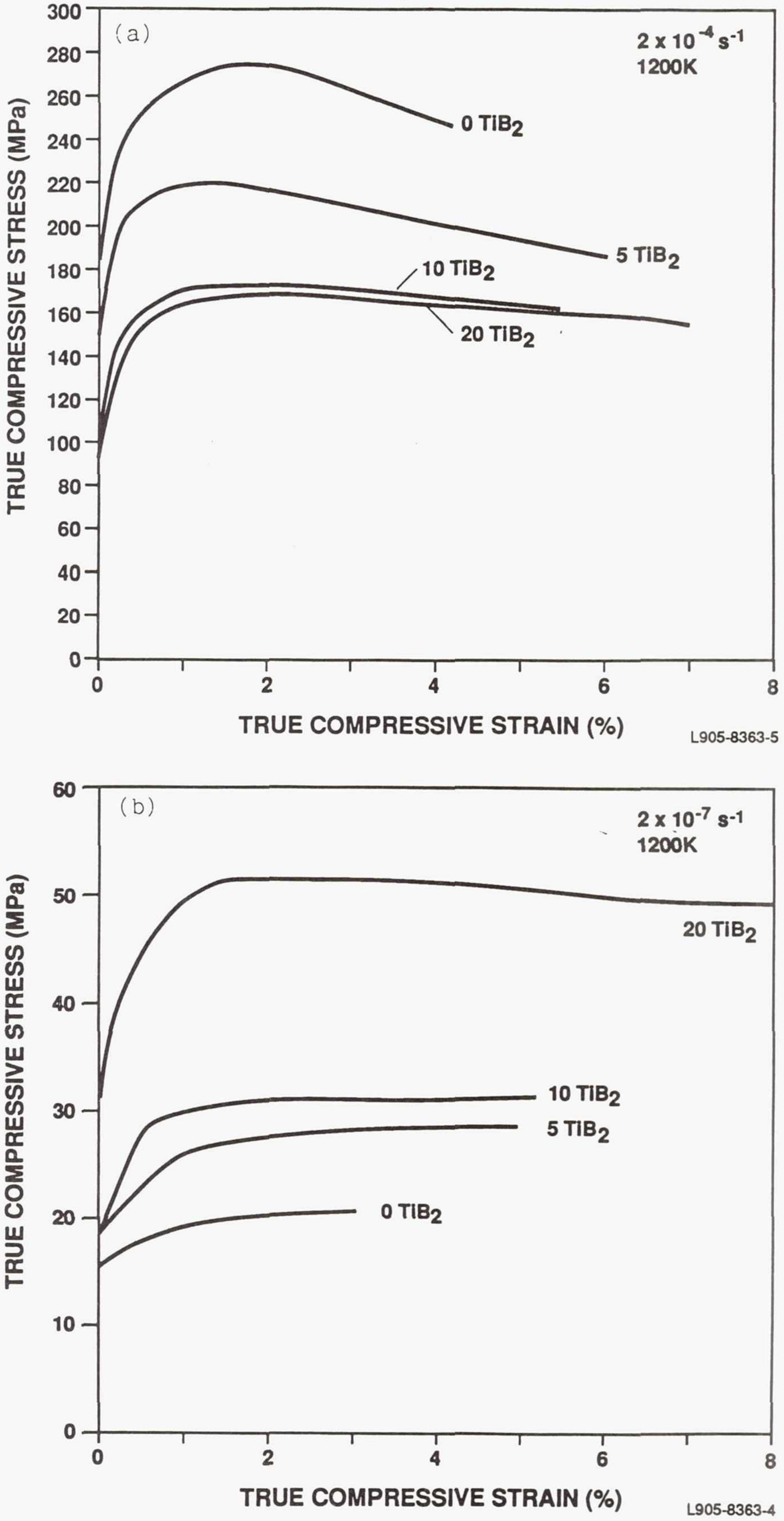

Figure 14. True compressive stress-strain diagrams at 1200K for the quaternary Al-Ti-Fe-2Nb (6.7 at.% Fe) compound containing various levels of TiB_2 additions: (a) strain rate = $2 \times 10^{-4} s^{-1}$ and (b) strain rate - $2 \times 10^{-7} s^{-1}$.

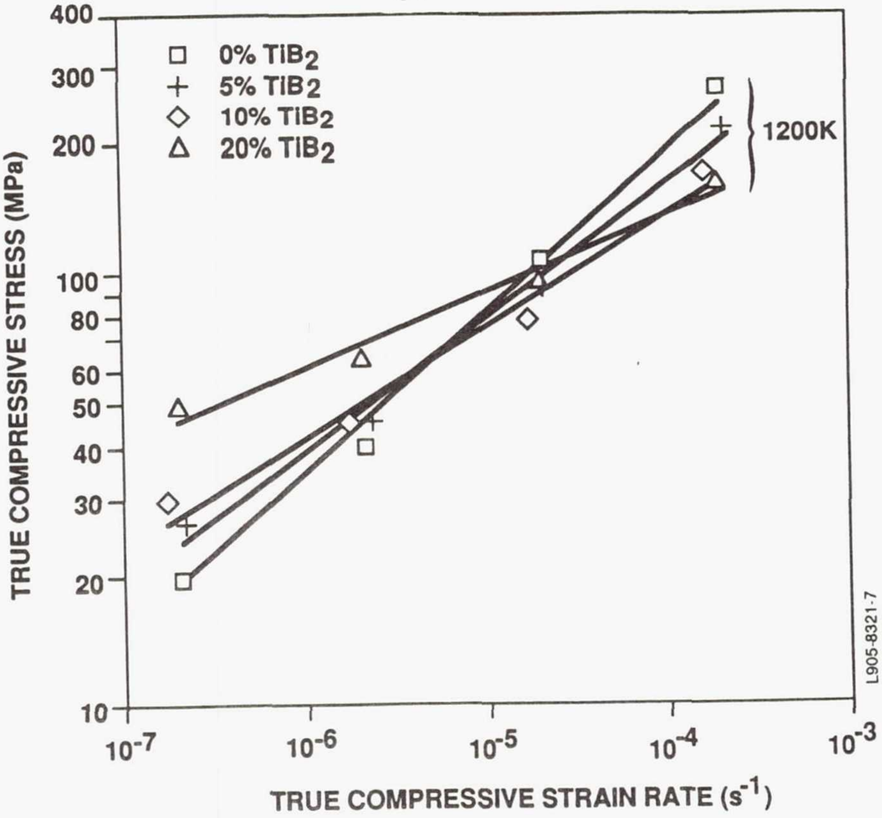

Figure 15. True compressive stress-strain rate behavior at 1200K for monolithic Al-Ti-Fe-2Nb (6.7 at.% Fe) and particulate-reinforced composites with various amounts of TiB_2.

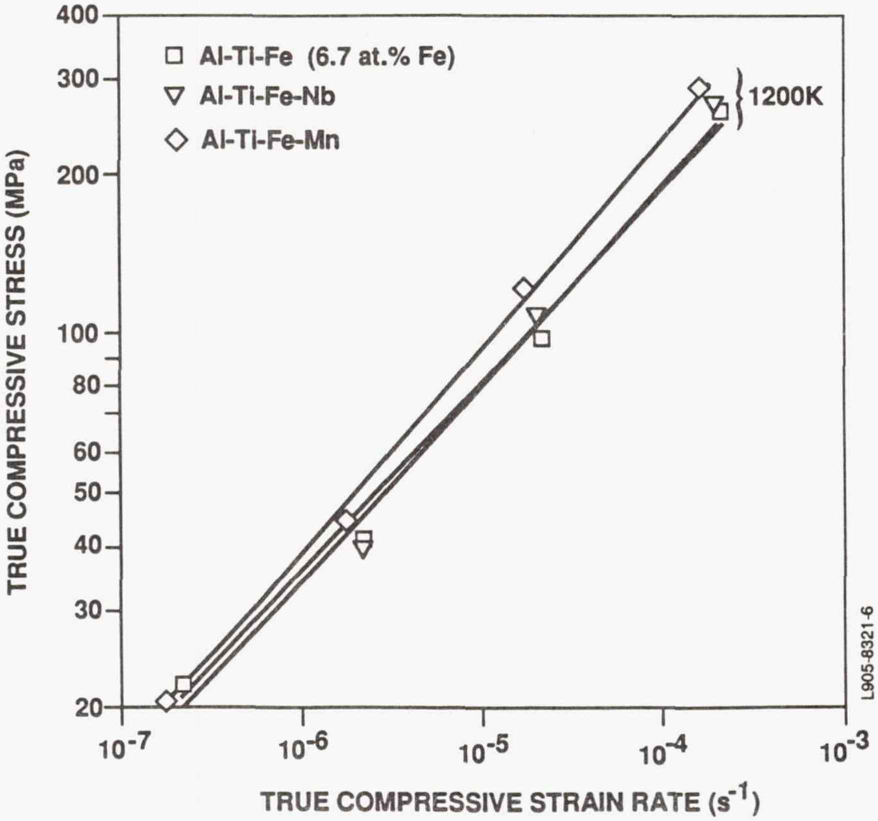

Figure 16. True compressive stress-strain rate behavior at 1200K for monolithic Al-Ti-Fe (6.7 at.% Fe) with and without quaternary additions (2Nb, 2Mn).

(a) (b)

(Acknowledgments are due to Don Clemens of Pratt & Whitney, Florida for these isothermal forgings.)

Figure 17. Low-magnification photographs of (a) $Al_{67}Ti_{25}Cr_8$ and (b) $Al_{66}Ti_{25}Mn_9$ forgings.

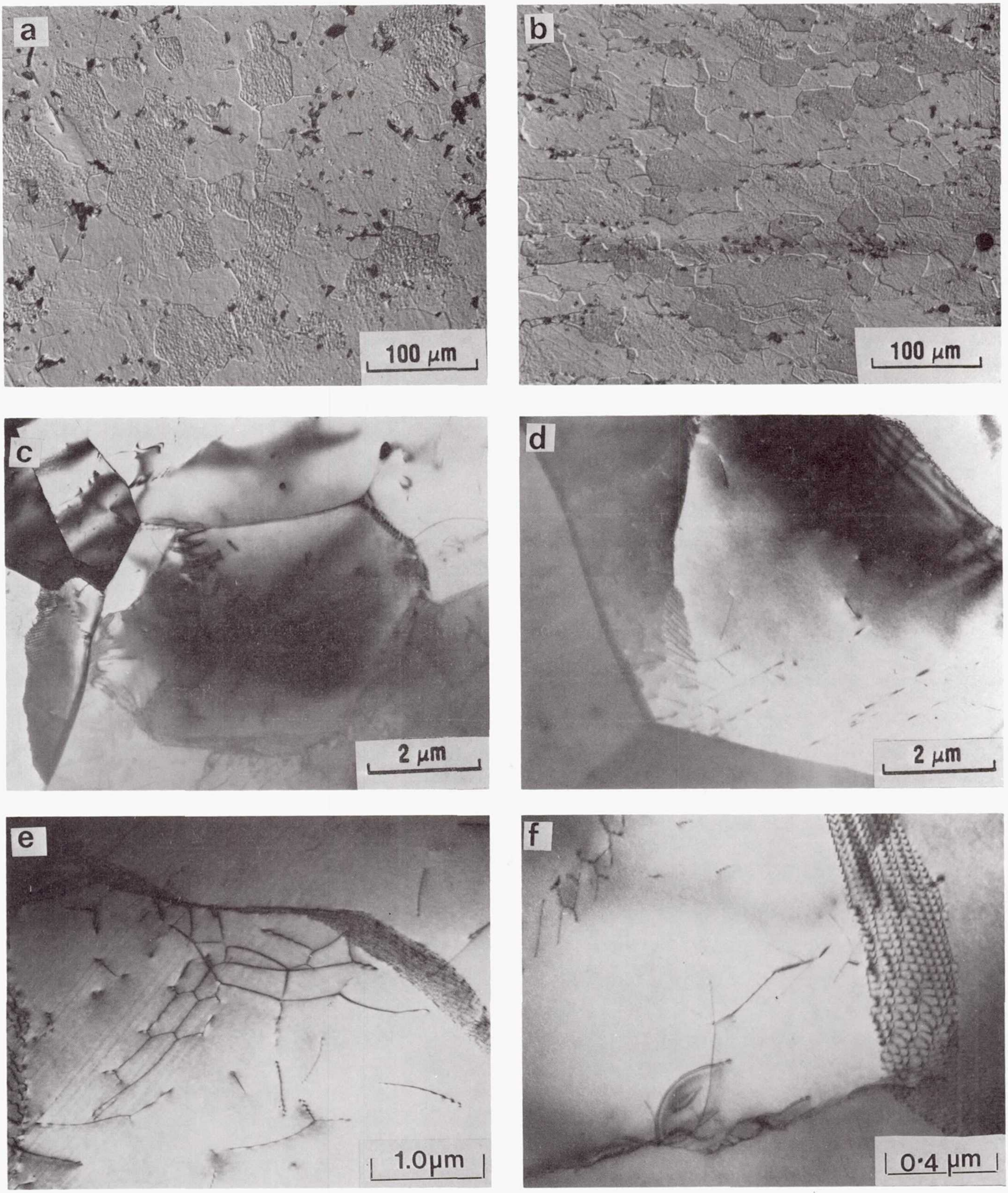

Figure 18. Representative microstructures in the forged L1_2 compounds:(a,b) optical micrographs in the radial and through-thickness plane of $Al_{66}Ti_{25}Mn_9$, respectively, (c,d) TEM micrographs showing subgrains in $Al_{67}Ti_{25}Cr_8$ and $Al_{66}Ti_{25}Mn_9$, respectively, and (e,f) subgrain boundaries and dislocation networks in $Al_{67}Ti_{25}Cr_8$ and $Al_{66}Ti_{25}Mn_9$, respectively.

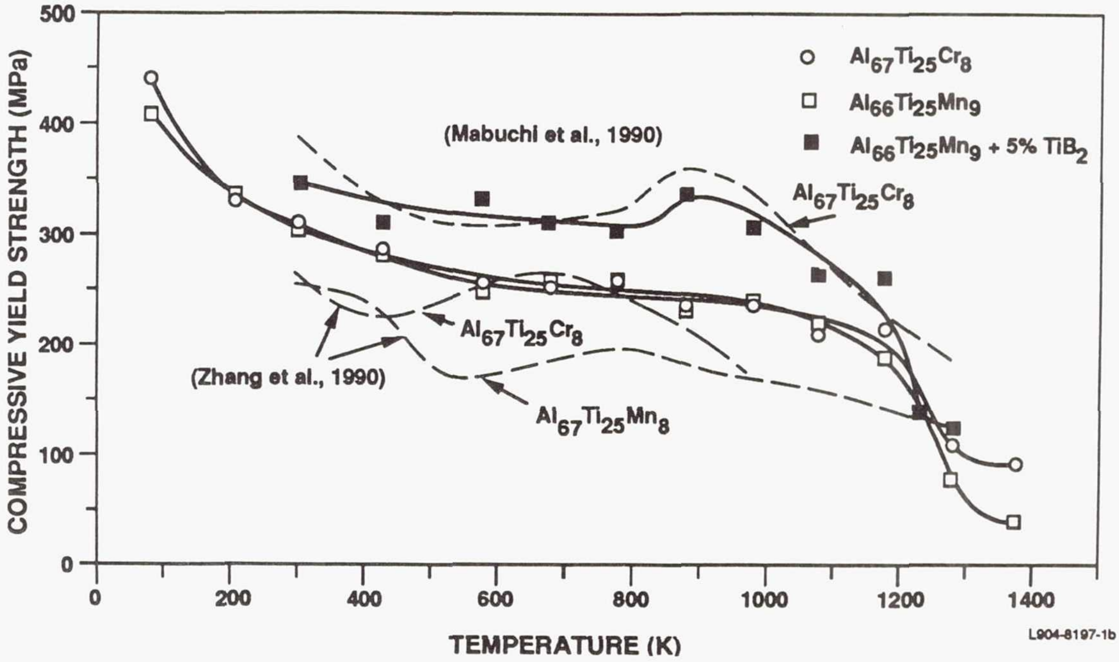

Figure 19. Compressive yield strength versus temperature for cast, homogenized, and forged $Al_{67}Ti_{25}Cr_8$, $Al_{66}Ti_{25}Mn_9$, and $Al_{66}Ti_{25}Mn_9$ + 5 vol.% TiB_2.

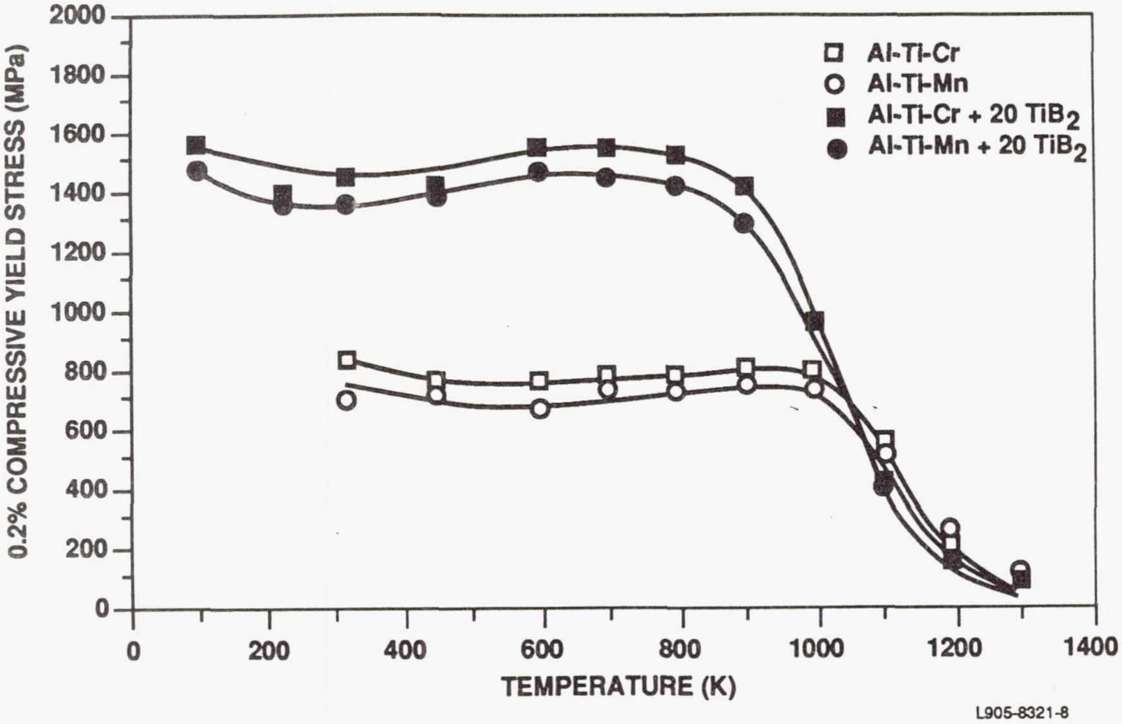

Figure 20. Compressive yield strength versus temperature for hot-pressed and HIPed $Al_{67}Ti_{25}Cr_8$ and $Al_{66}Ti_{25}Mn_9$ with and without 20 vol.% TiB_2, produced via the powder route.

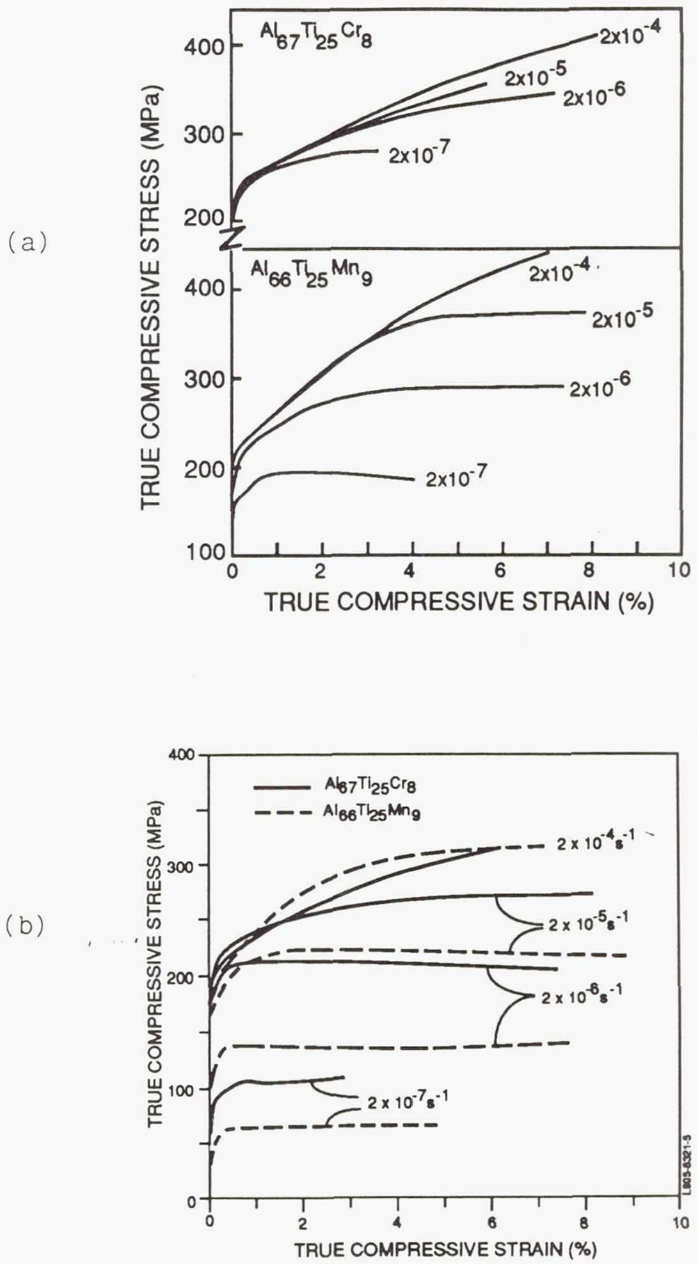

Figure 21. True compressive stress-strain diagrams at various strain rates for the forged monolithic $L1_2$ compounds $Al_{67}Ti_{25}Cr_8$ and $Al_{66}Ti_{25}Mn_9$ at (a) 1000K and (b) 1100K.

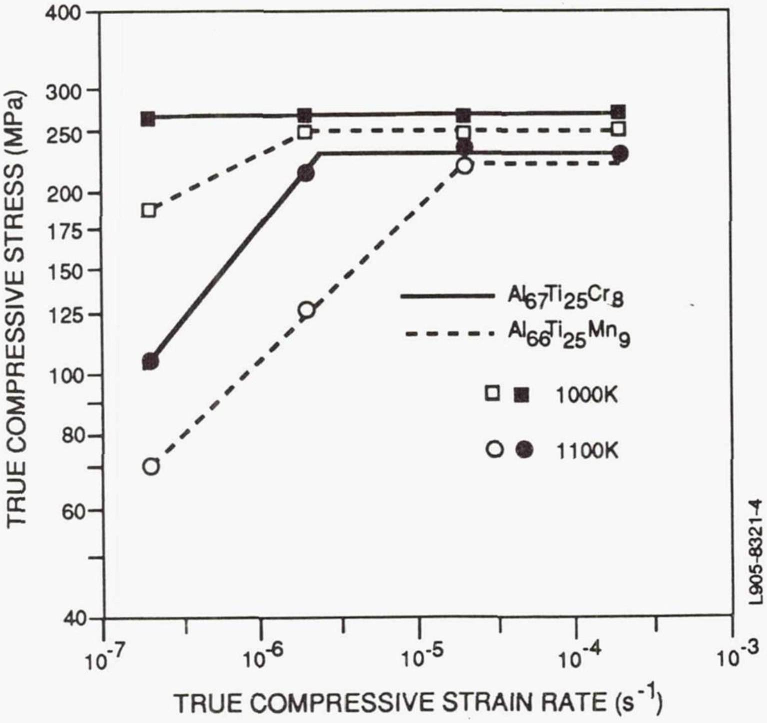

Figure 22. True compressive stress-strain rate behavior at 1000K and 1100K for the forged monolithic $L1_2$ compounds $Al_{67}Ti_{25}Cr_8$ and $Al_{66}Ti_{25}Mn_9$.

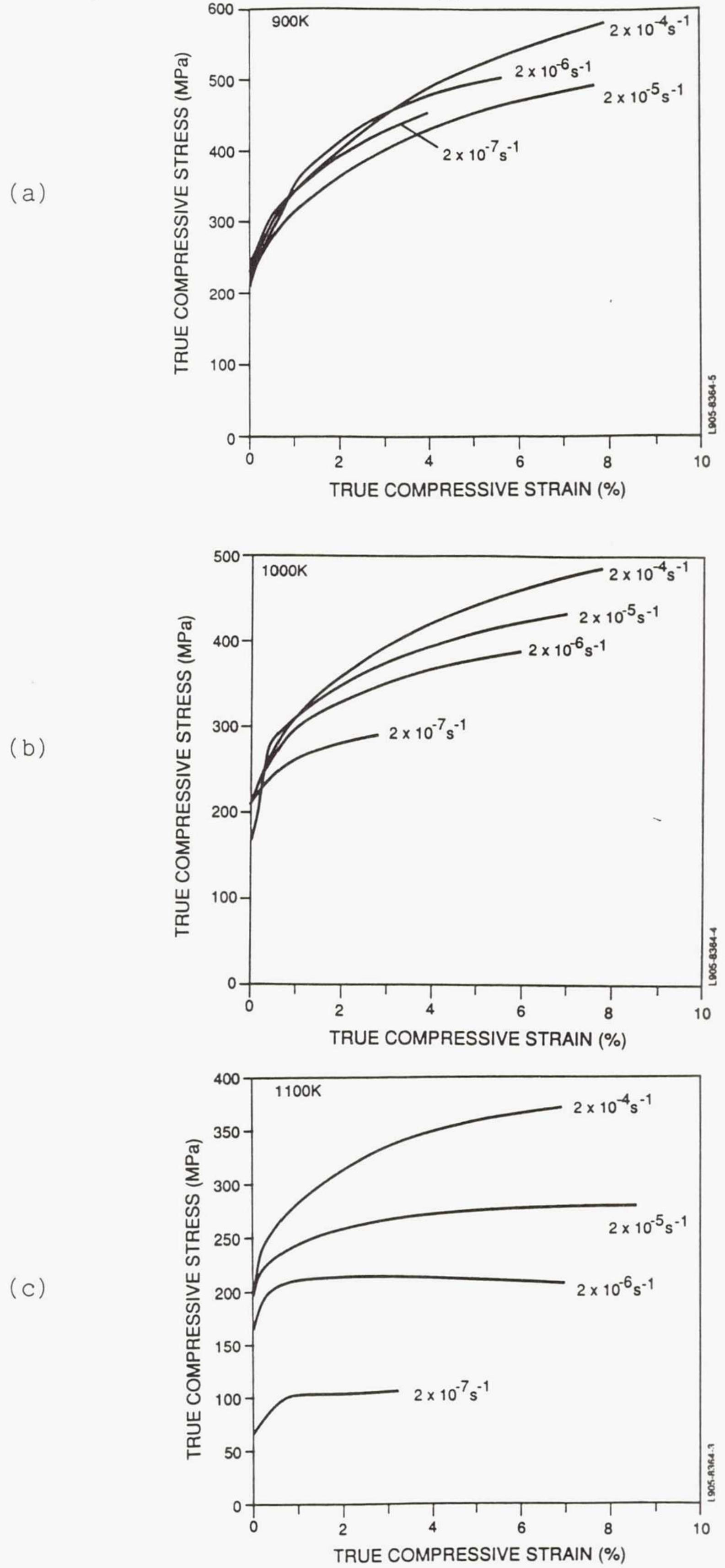

Figure 23. True compressive stress-strain diagrams for the forged $Al_{66}Ti_{25}Mn_9$ + 5 vol.% TiB_2 material at various strain rates at (a) 900K, (b) 1000K, and (c) 1100K.

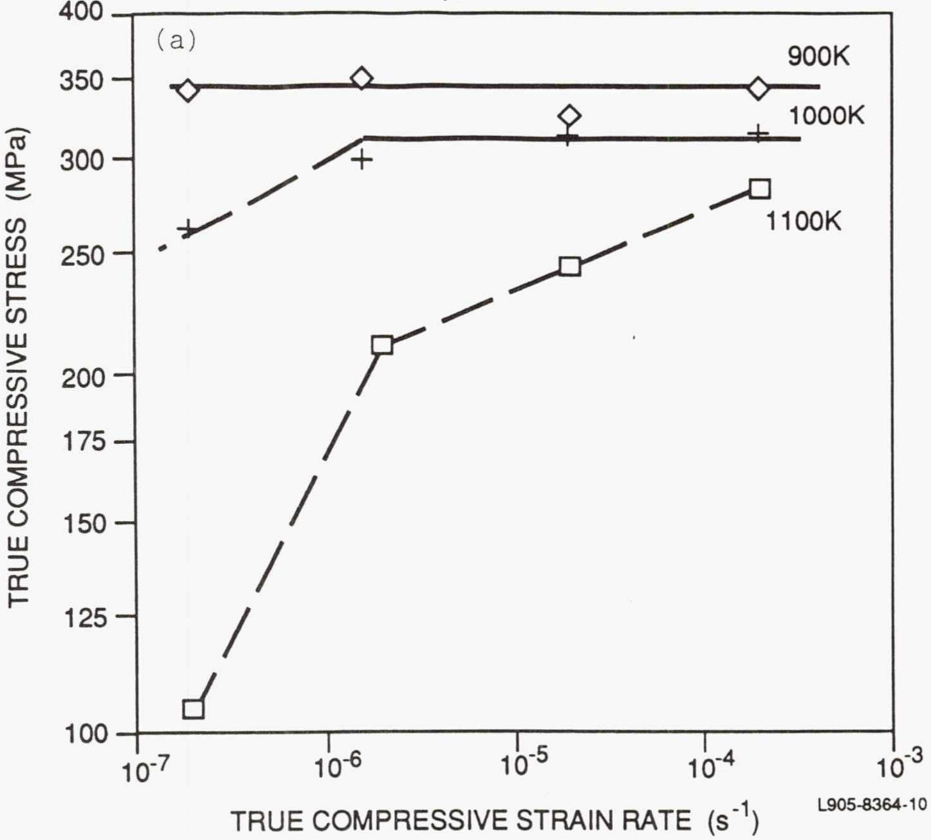

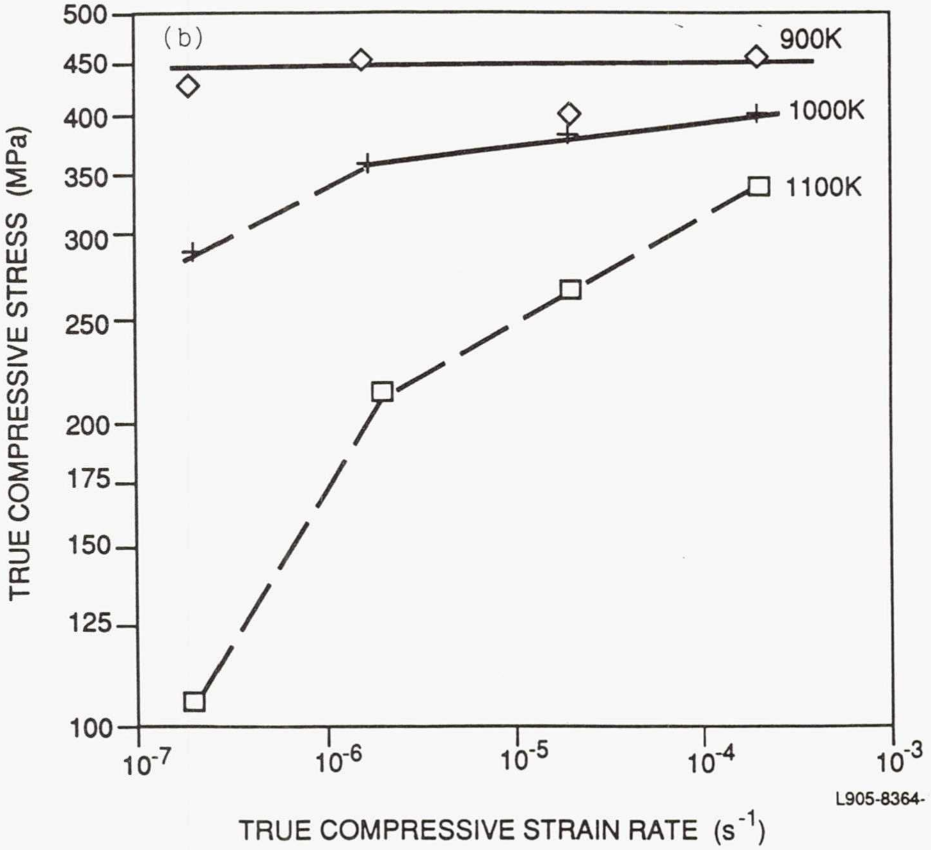

Figure 24. Variation in true compressive flow stress with strain rate at 900K, 1000K and 1100K for the forged $Al_{66}Ti_{25}Mn_9$ + 5 vol.% TiB_2 material at: (a) 1% compression strain and (b) 3% compression strain.

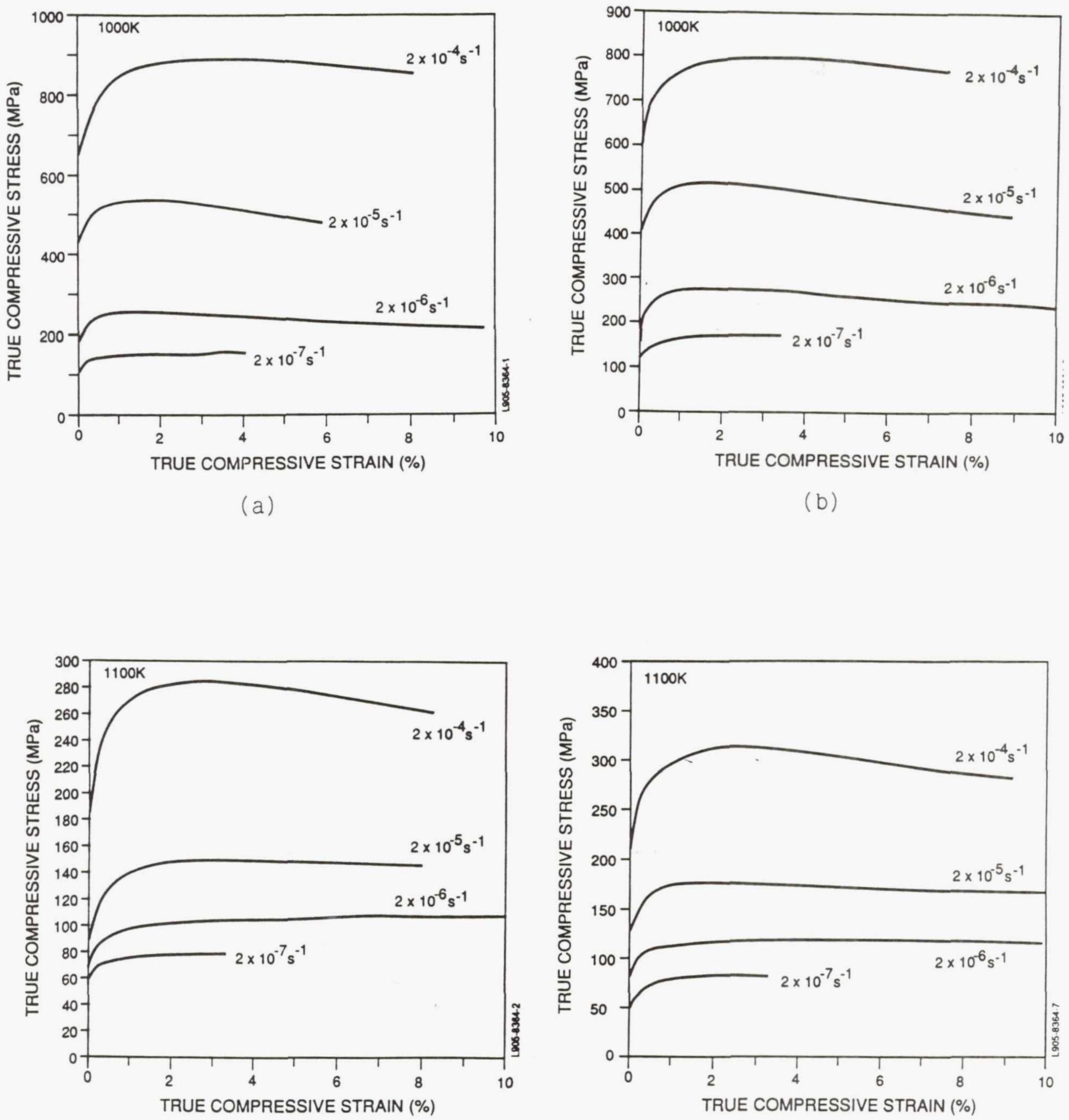

(a)

(b)

(c)

(d)

Figure 25. True compressive stress-strain diagrams at 1000K (a,b) and 1100K (c,d) over a range of strain rates for (a) $Al_{67}Ti_{25}Cr_8$ + 20 vol.% TiB_2, (b) $Al_{66}Ti_{25}Mn_9$ + 20 vol.% TiB_2 (c) $Al_{67}Ti_{25}Cr_8$ + 20 vol.% TiB_2, and (d) $Al_{66}Ti_{25}Mn_9$ + 20 vol.% TiB_2.

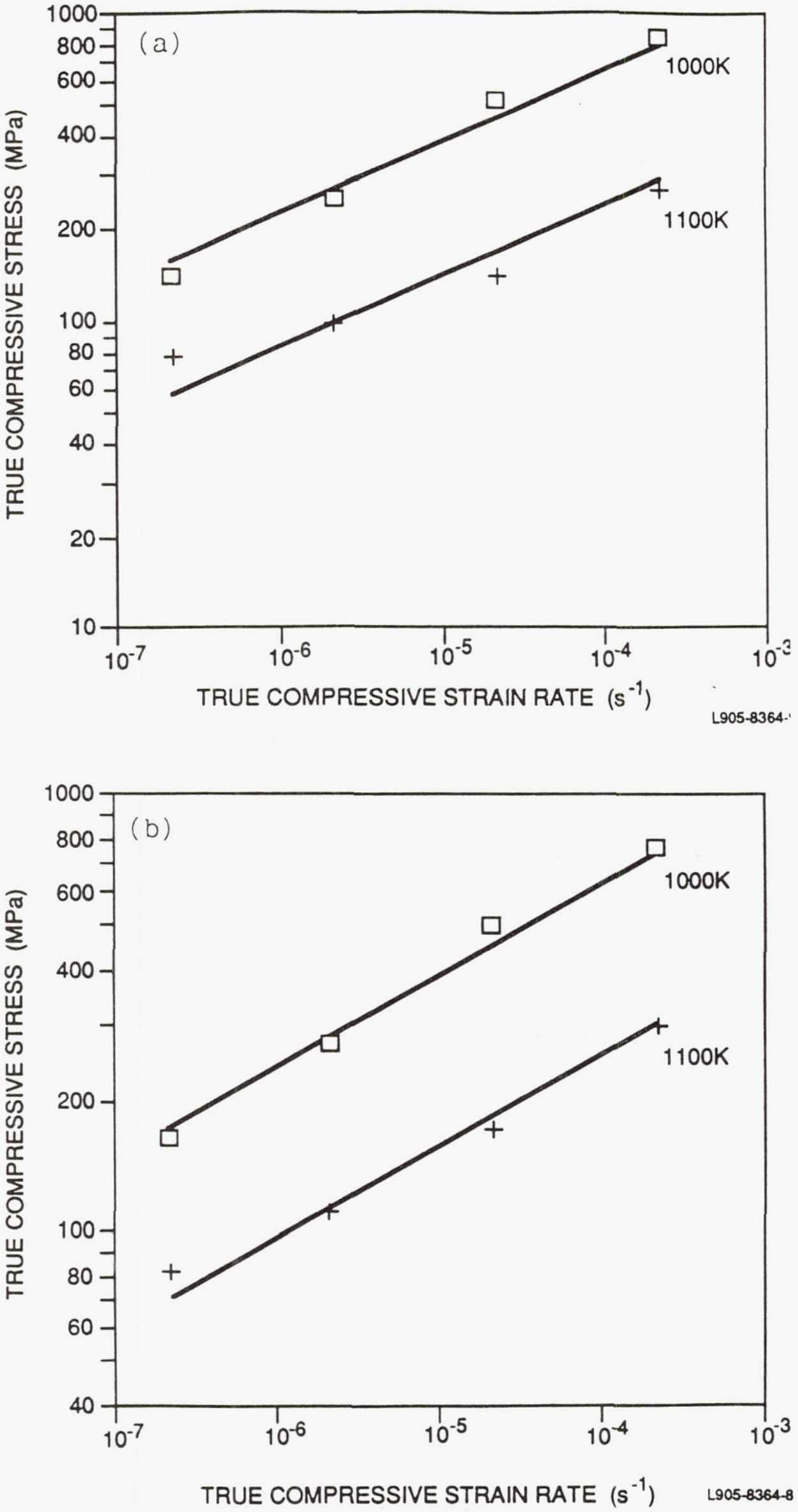

Figure 26. Variation in compressive flow stress at 1% strain with strain rate at 1000K and 1100K for (a) $Al_{67}Ti_{25}Cr_8$ + 20 vol.% TiB_2 and (b) $Al_{66}Ti_{25}Mn_9$ + 20 vol.% TiB_2.

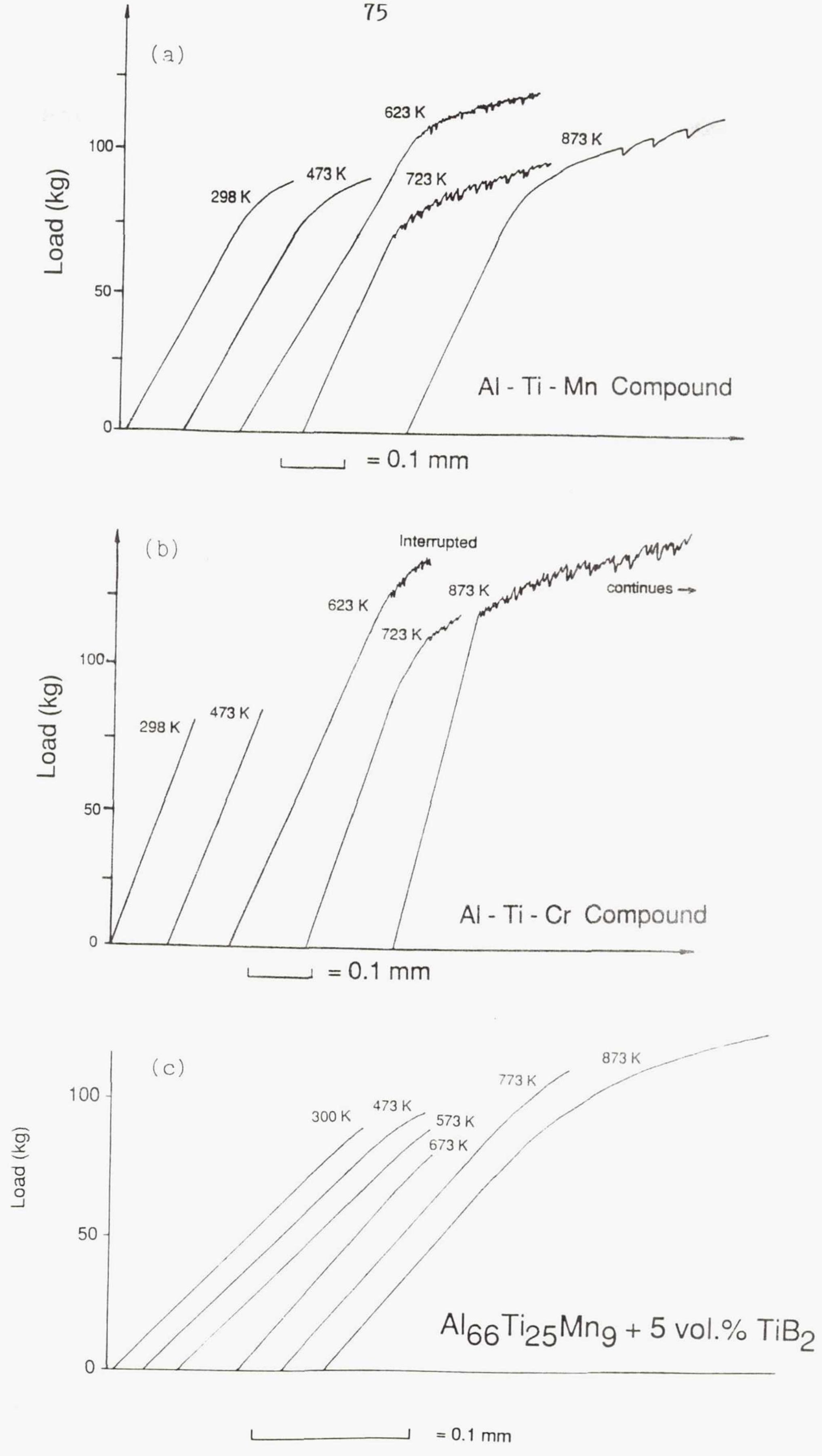

Figure 27. Load-displacement curves obtained from three-point bend tests at various temperatures on forged (a) $Al_{66}Ti_{25}Mn_9$, (b) $Al_{67}Ti_{25}Cr_8$, and (c) $Al_{66}Ti_{25}Mn_9$ + 5 vol.% TiB_2.

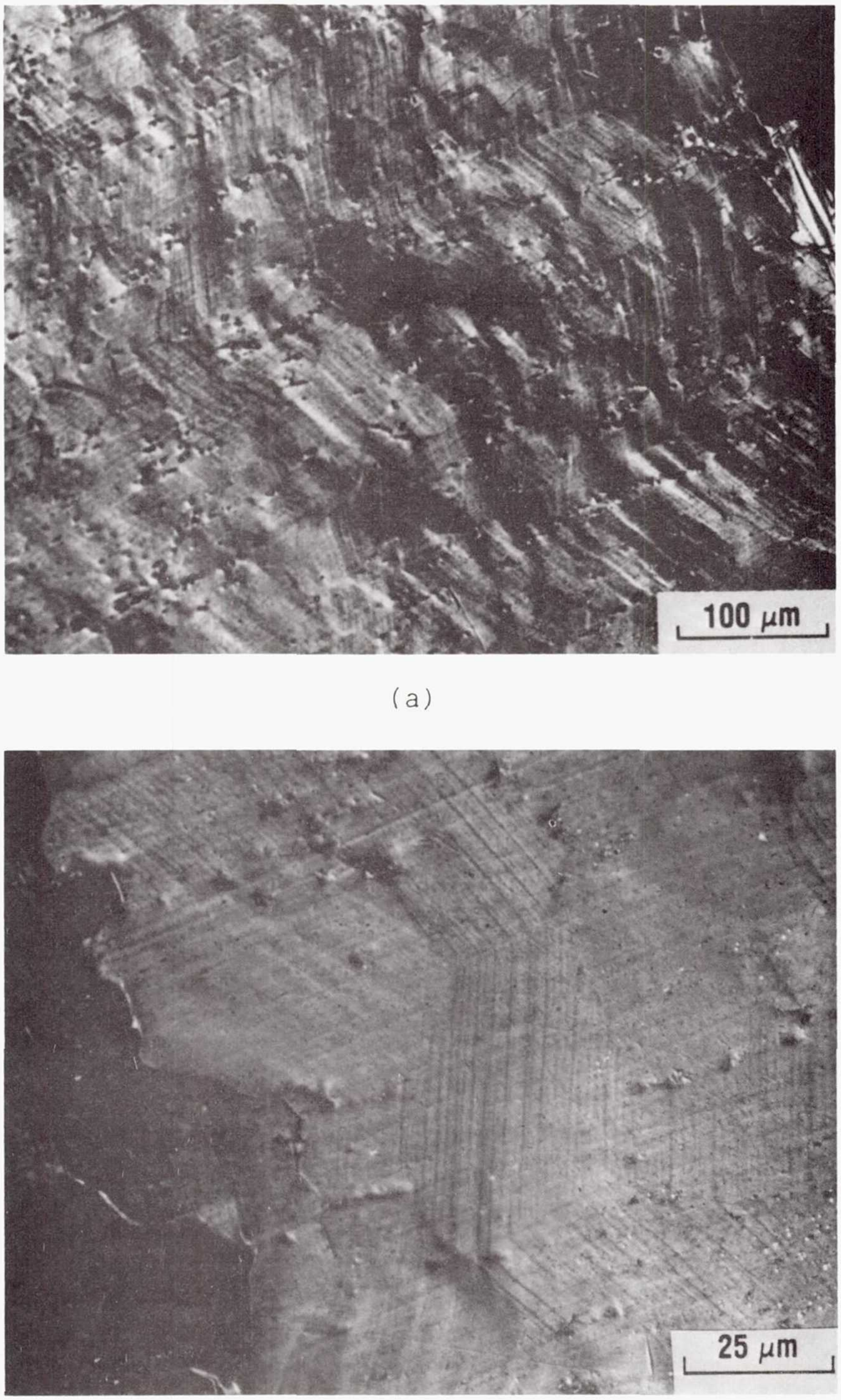

(a)

(b)

Figure 28. Optical micrographs of an Al-Ti-Mn bend specimen deformed at 623K, revealing: (a) slip traces transitioning from one grain to another and (b) only a single set of slip traces in a particular grain.

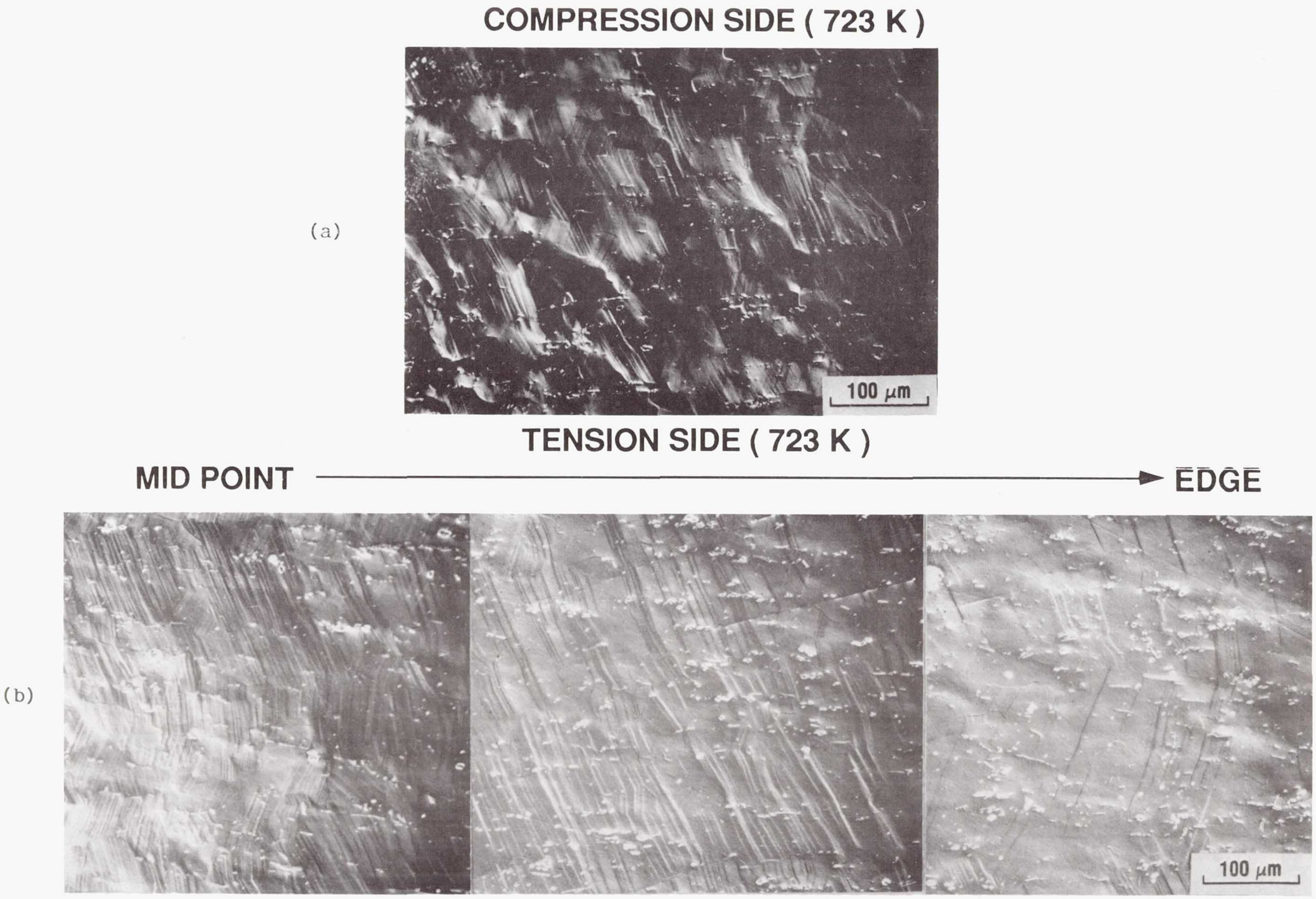

Figure 29. Surface deformation characteristics in the $Al_{66}Ti_{25}Mn_9$ bend specimen tested at 723K: (a) compression side and (b) tension side.

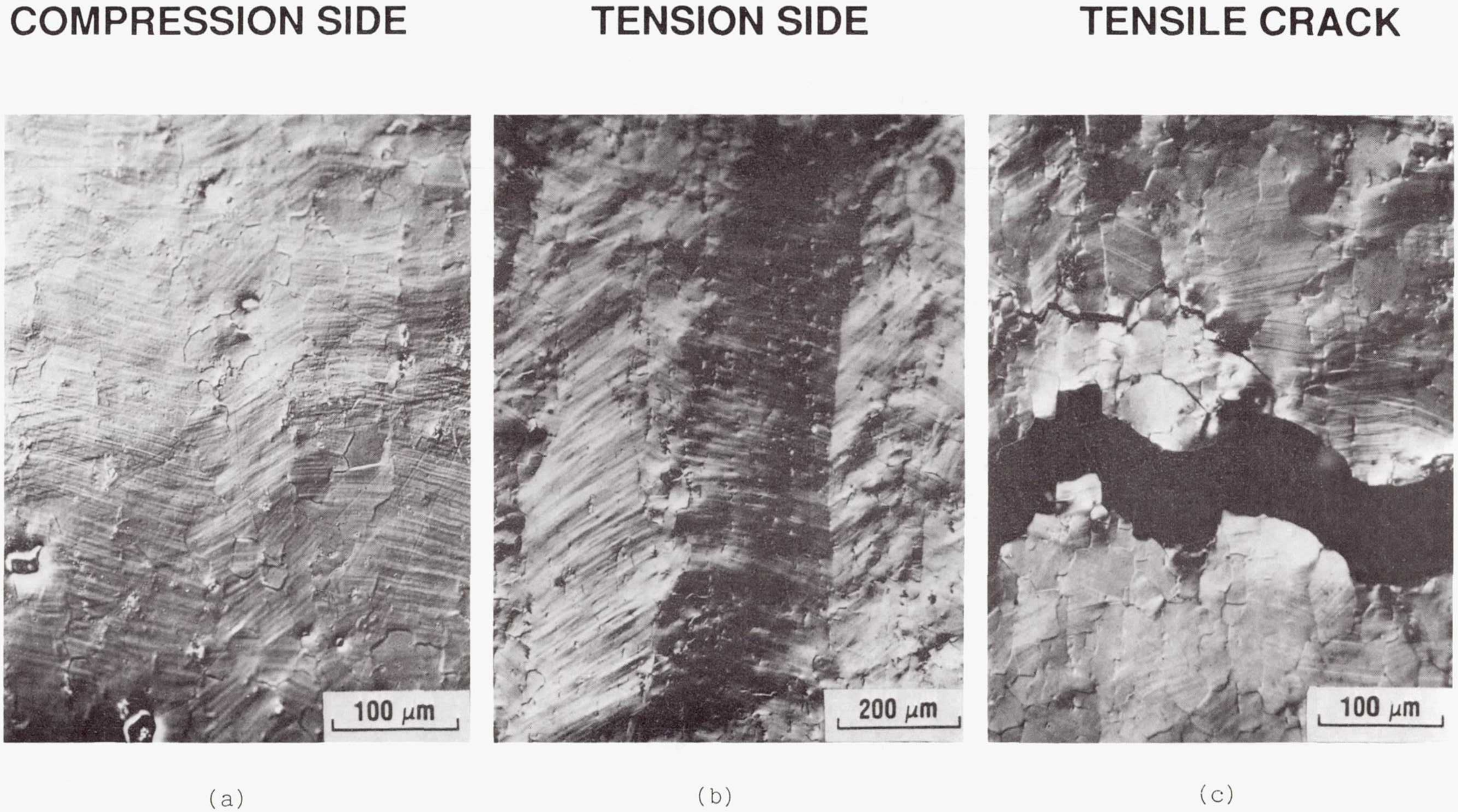

(a) (b) (c)

Figure 30. Slip traces on the surface of a bend specimen of $Al_{66}Ti_{25}Mn_9$ tested at 873K: (a) compression side, (b) tension side, and (c) tension side adjacent to the primary crack.

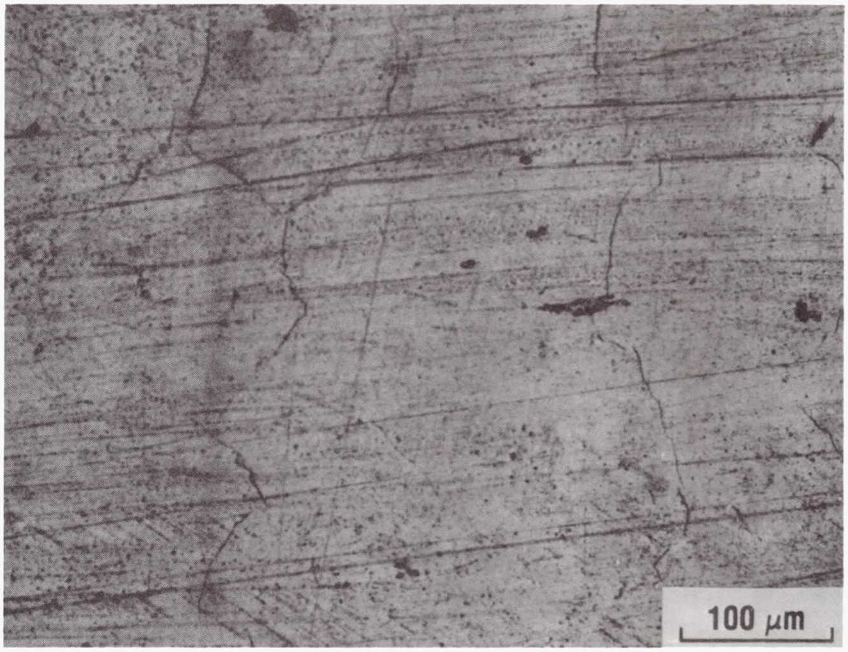

Figure 31. Tensile surface of a bend specimen of $Al_{67}Ti_{25}Cr_8$ deformed at 623K, showing fine cracks.

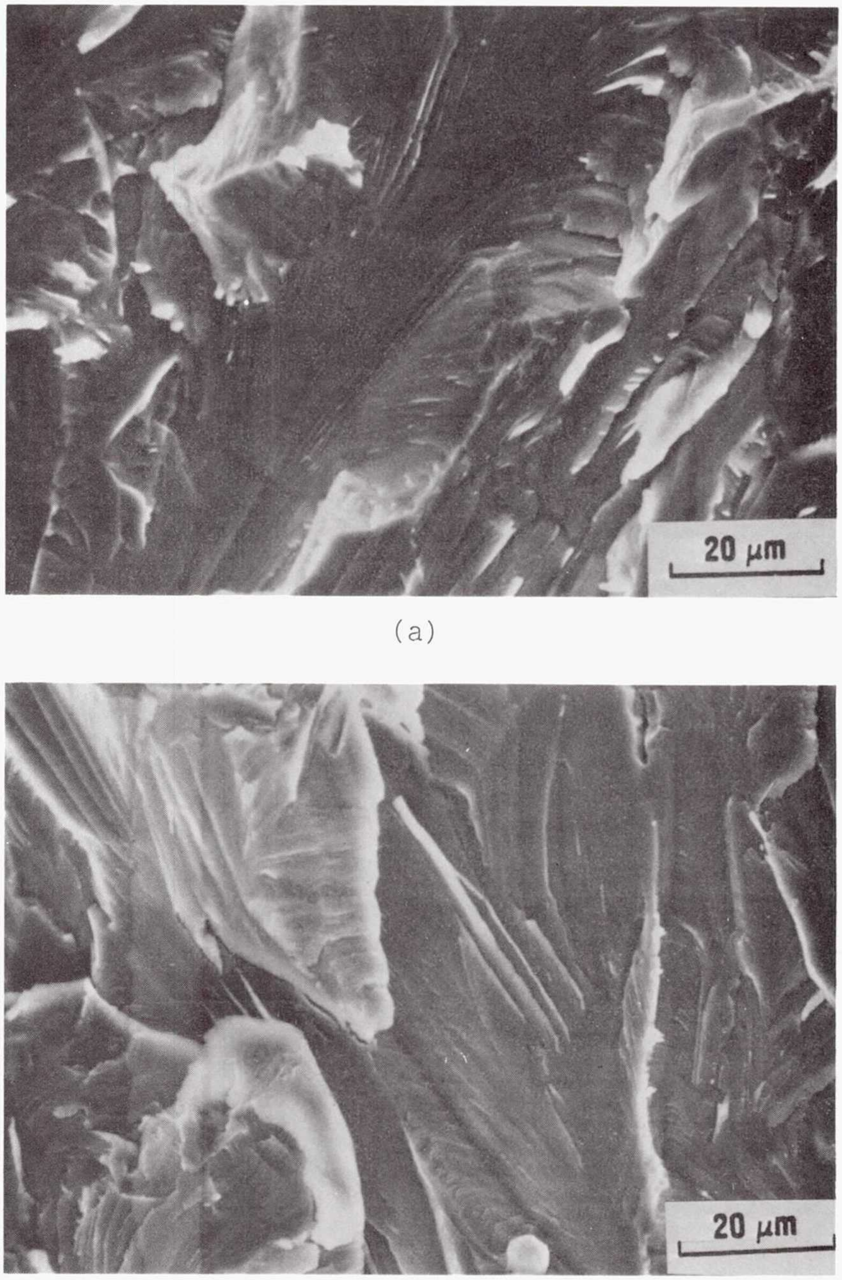

(a)

(b)

Figure 32. Bend fracture surface from a specimen of $Al_{67}Ti_{25}Cr_8$ tested at (a) 300K and (b) 473K.

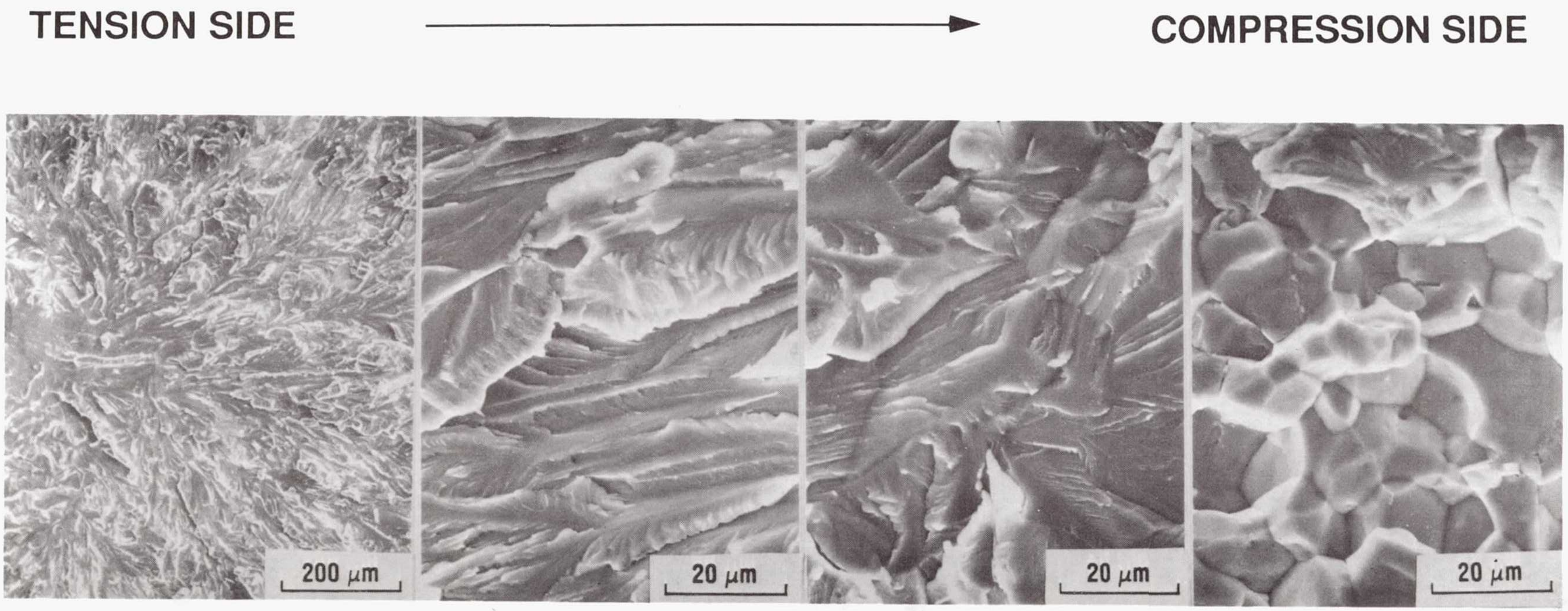

Figure 33. Bend fracture surface from a sample of $Al_{67}Ti_{25}Cr_8$ tested at 723K, showing a transition from transgranular cleavage on the tensile side to a mixture of transgranular cleavage and intergranular failure on the compression side.

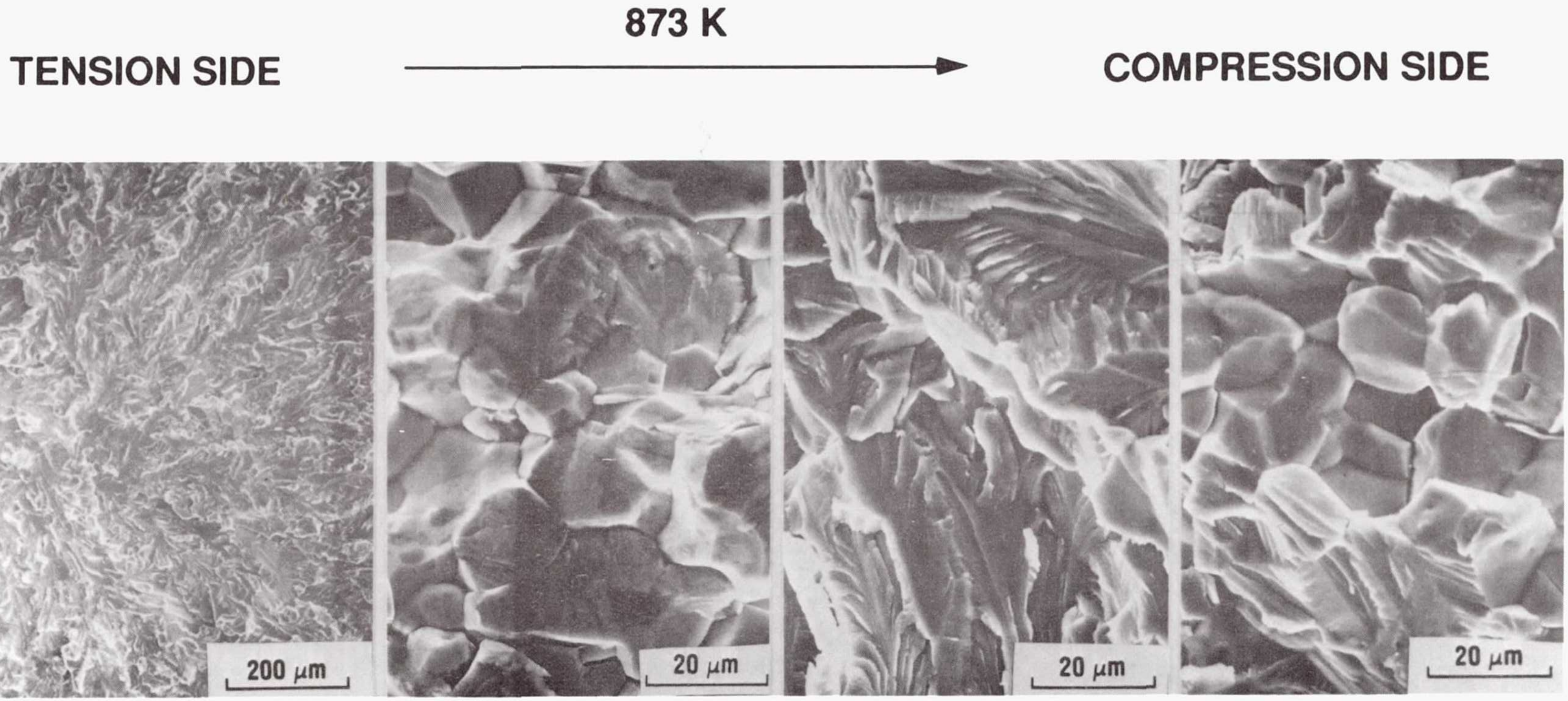

Figure 34. Intergranular failure and transgranular cleavage on both the tensile and compressive sides of bend specimens of $Al_{67}Ti_{25}Cr_8$ tested at 873K.

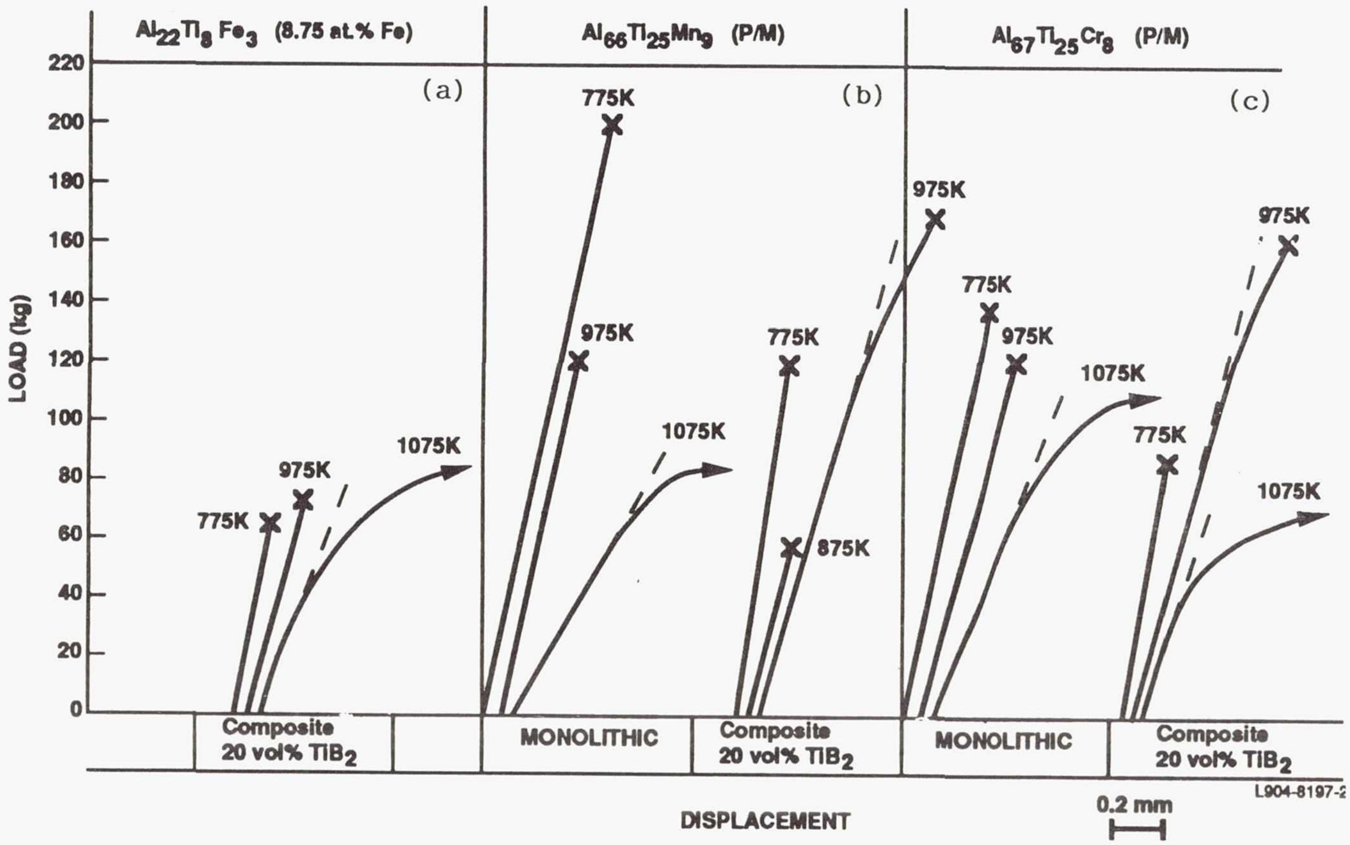

Figure 35. Load-displacement curves from three-point bend tests of P/M-processed (a) $Al_{22}Fe_3Ti_8$ + 20 vol.% TiB_2, (b,c) $Al_{66}Ti_{25}Mn_9$ and $Al_{67}Ti_{25}Cr_8$ with and without 20 vol.% TiB_2.

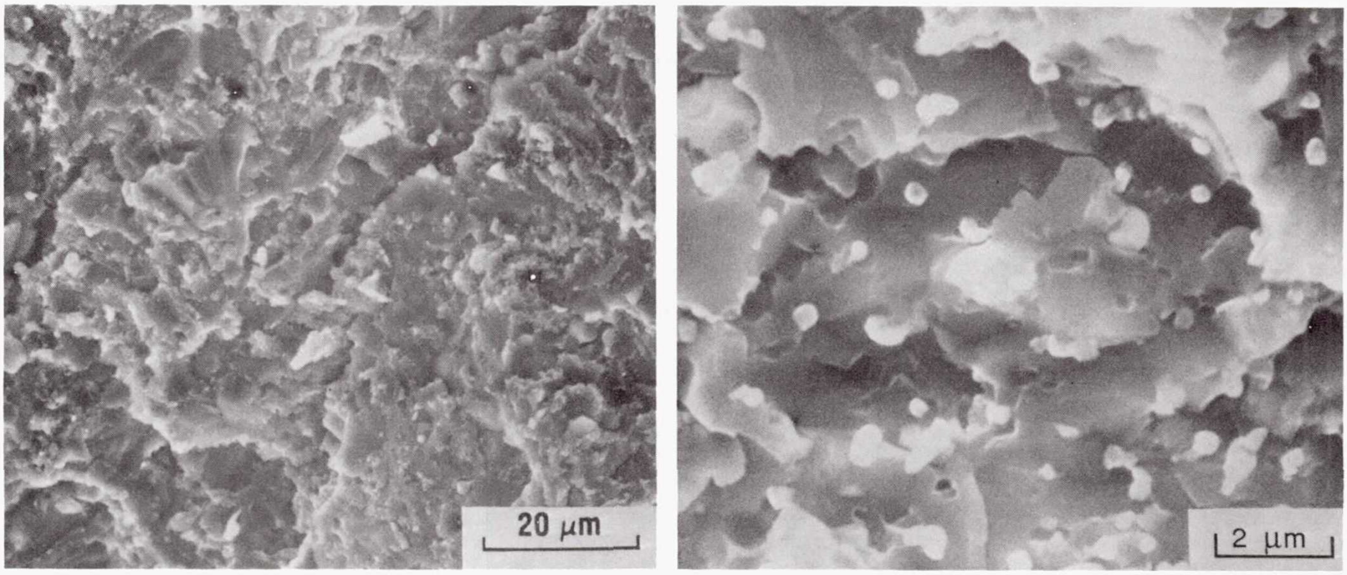

(a) (b)

Figure 36. Fracture surface from a bend specimen of P/M-processed $Al_{66}Ti_{25}Mn_9$ tested at 773K; (a) transgranular cleavage and (b) fine oxide particles on the cleaved surface.

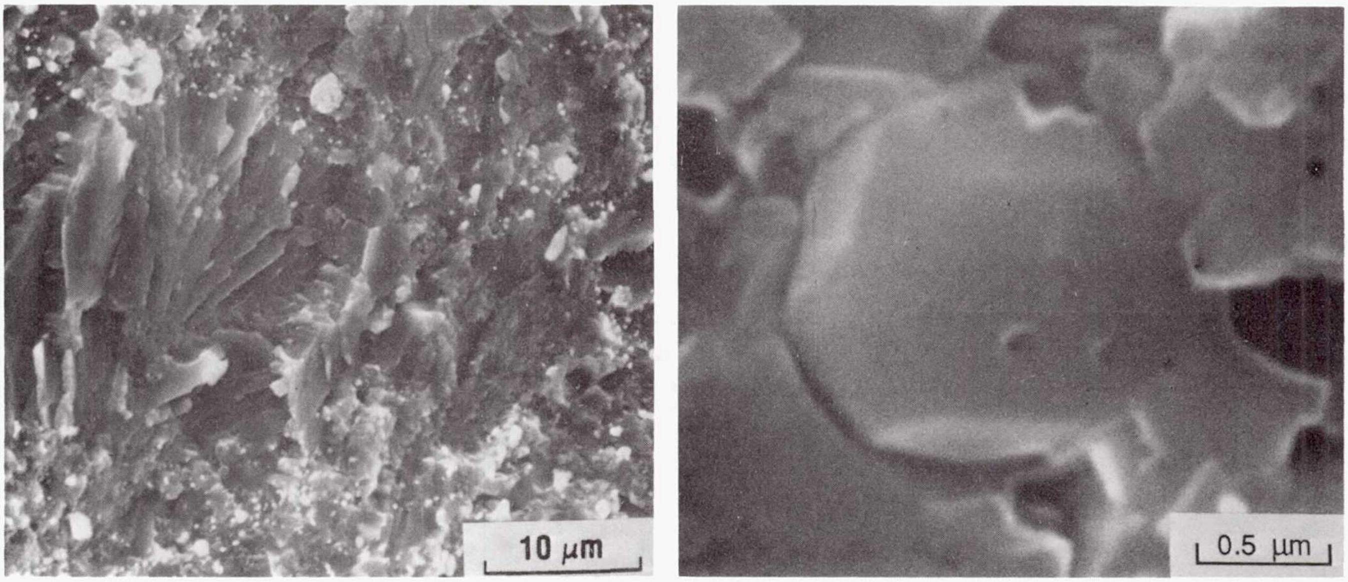

(a) (b)

Figure 37. Fracture surface from a bend specimen of P/M-processed $Al_{66}Ti_{25}Mn_9$ + 20 vol.% TiB_2, tested at 973K: (a) transgranular cleavage and (b) fracture at TiB_2 particle-matrix interface.

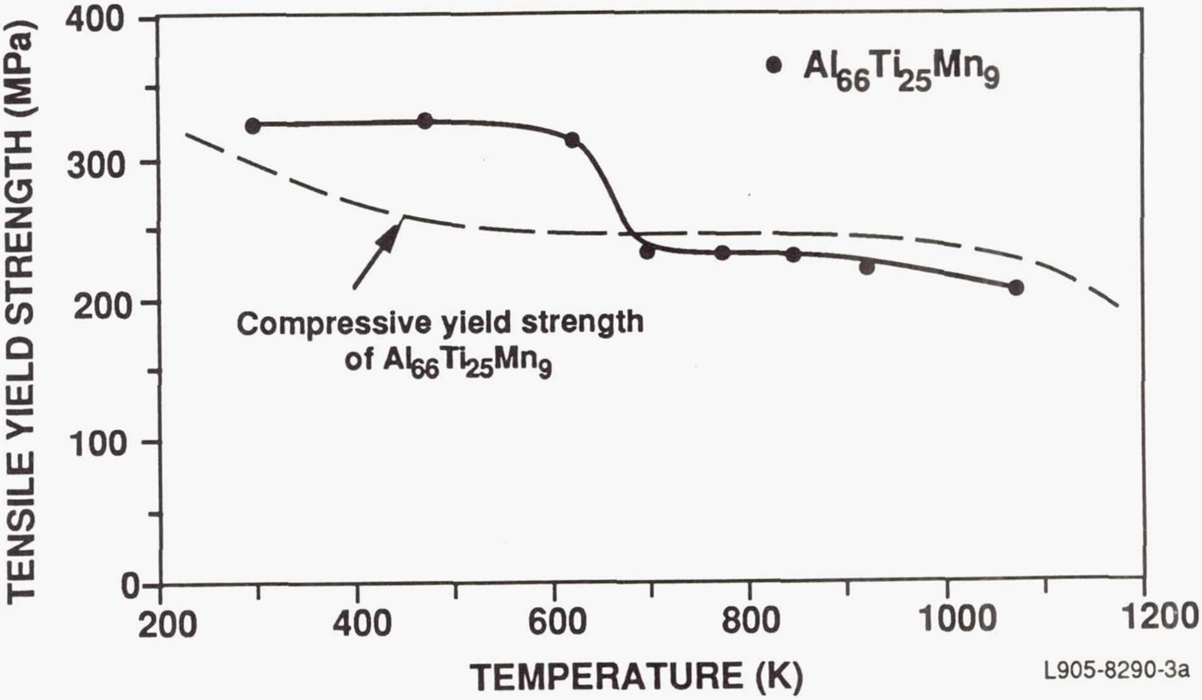

Figure 38. The variation in yield strength with temperature for the forged $L1_2$ compound $Al_{66}Ti_{25}Mn_9$ in tension and compression.

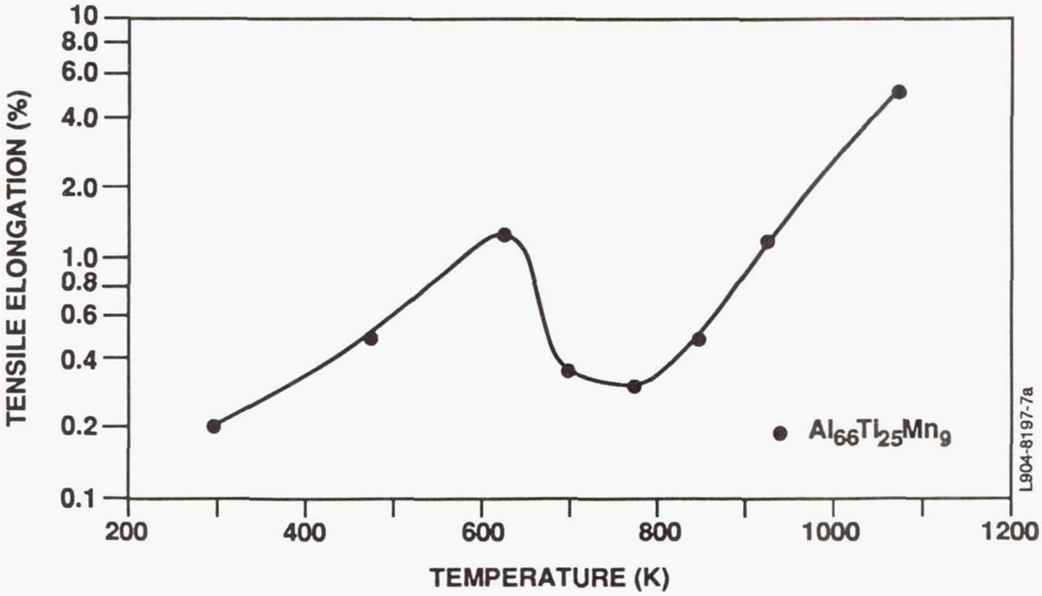

Figure 39. The variation in tensile ductility with temperature for the forged $L1_2$ compound $Al_{66}Ti_{25}Mn_9$.

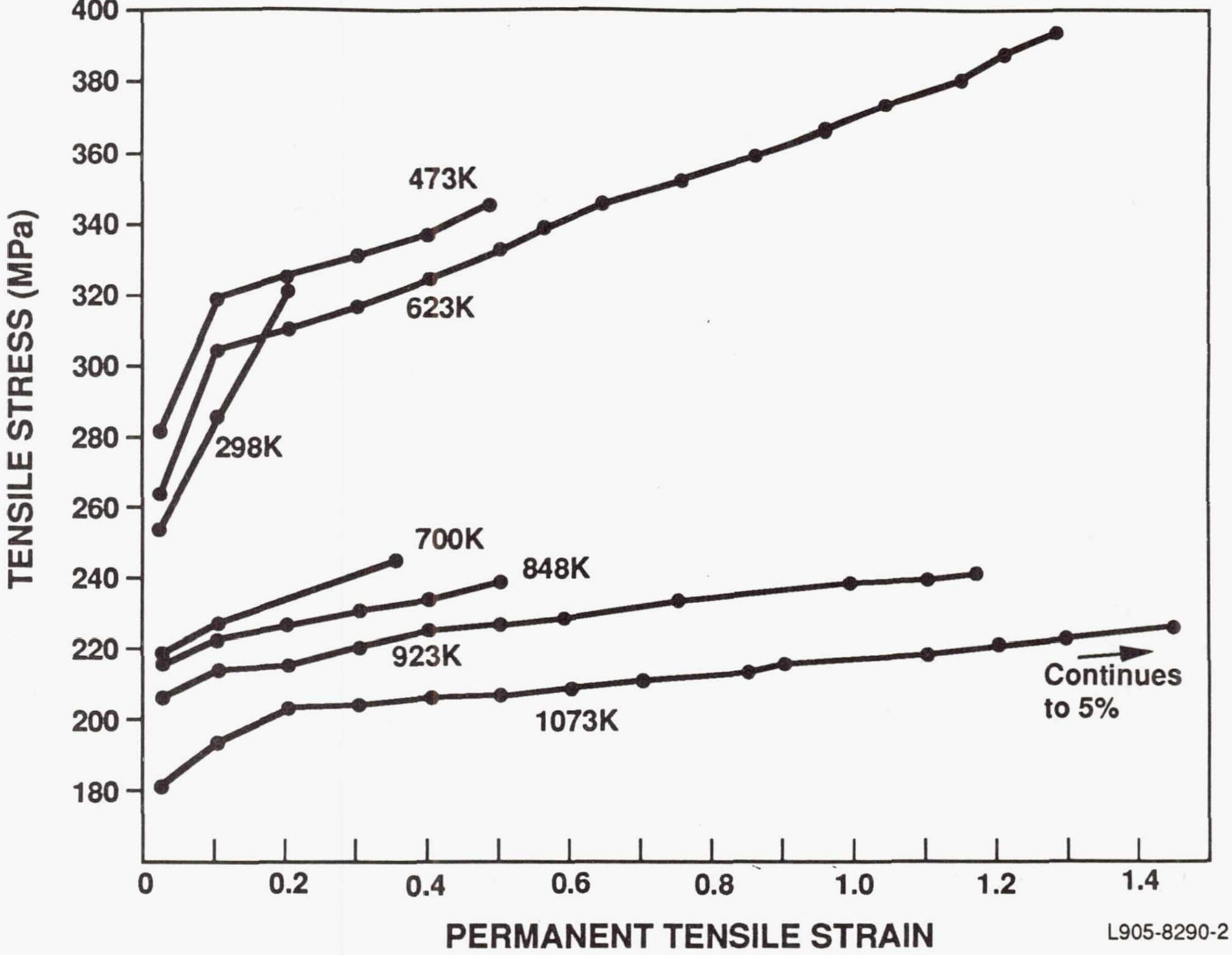

Figure 40. Tensile flow stress versus plastic strain at various temperatures derived from the load-displacement curves. Note: flow stress was calculated from the original cross-sectional area.

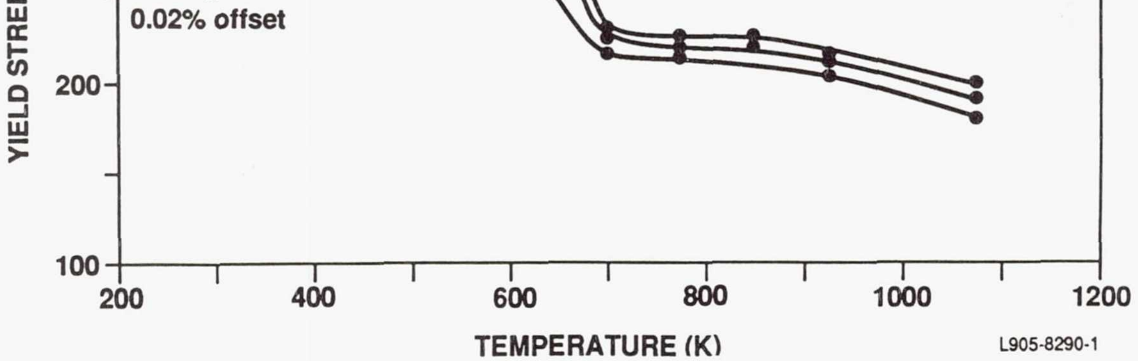

Figure 41. Tensile yield strength for 0.02%, 0.1%, and 0.2% offset strain versus test temperature.

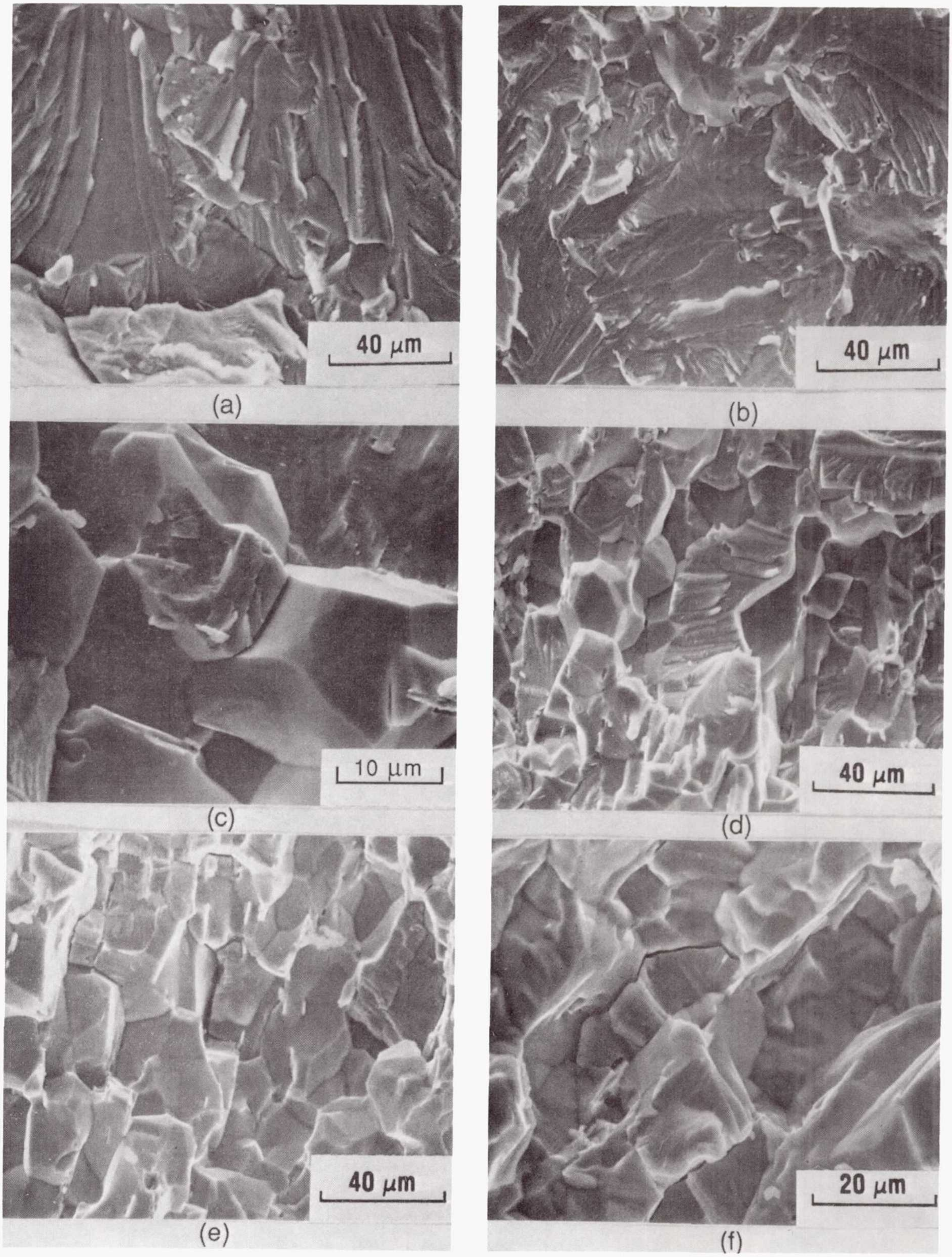

Figure 42. Fracture surfaces of tensile specimens tested at (a) 298K, (b,c) 473K, (d) 773K, (e) 923K, and (f) 1073K.

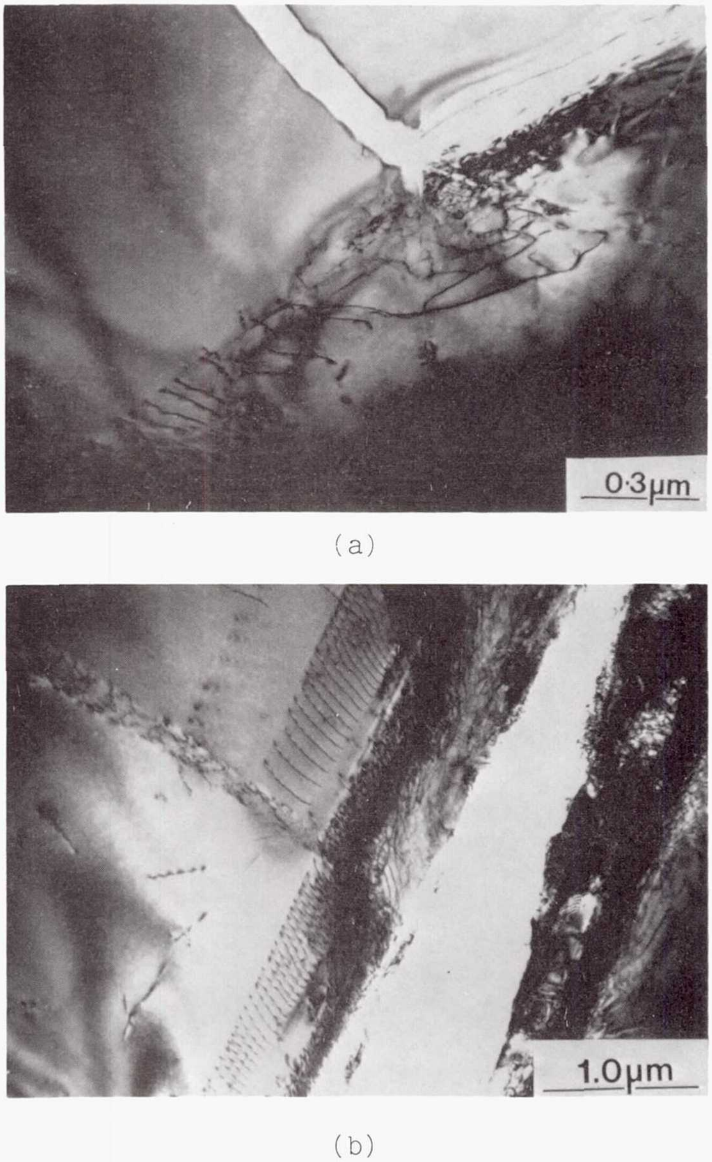

Figure 43. Dislocation structures in a thin, deformed foil: (a) region ahead of a crack tip and (b) region adjacent to another crack.

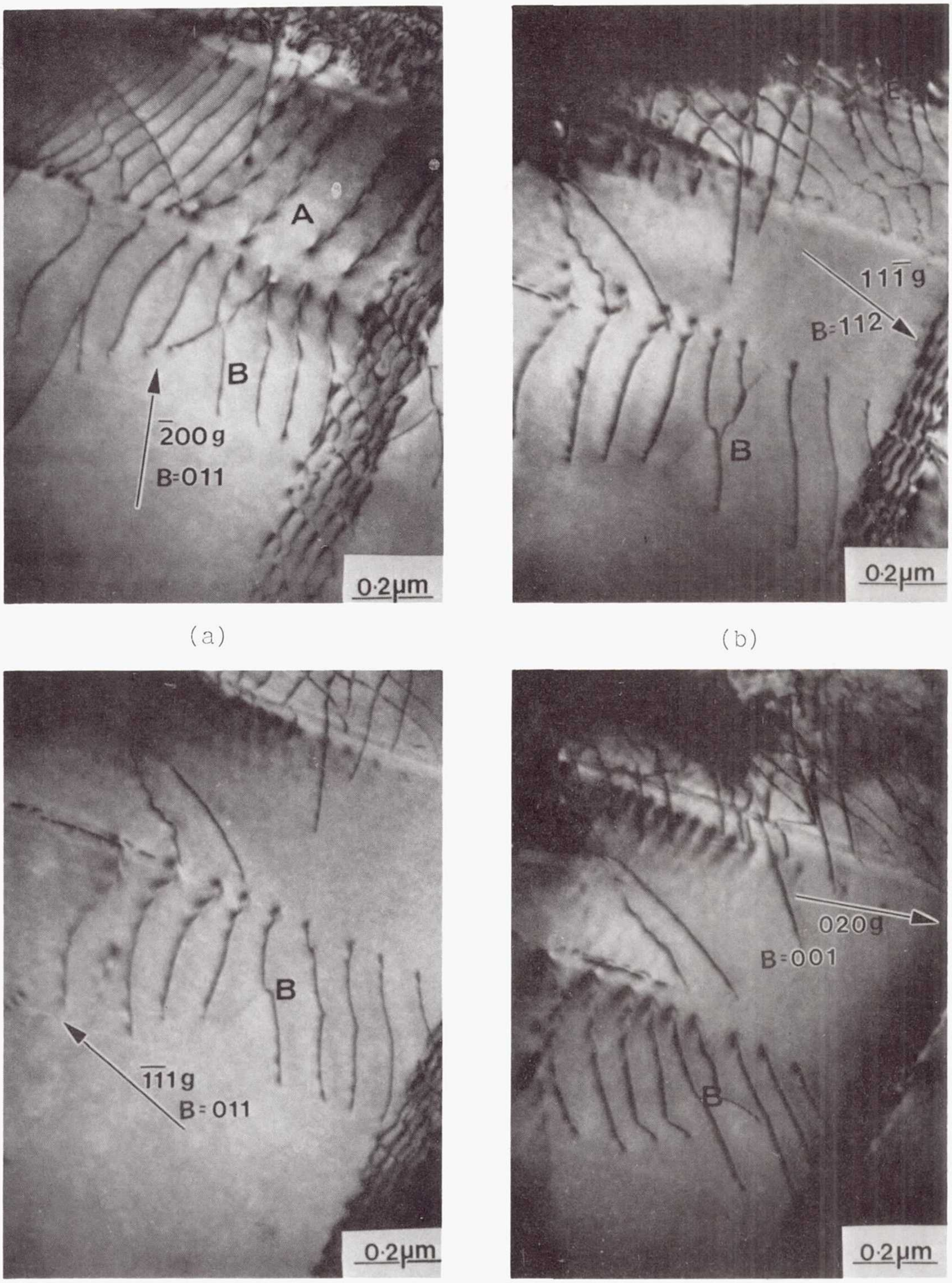

(a) (b)

(c) (d)

$$\vec{b} = [101]$$

$$\hat{u} = [2\bar{1}1]$$

$$\text{Slip Plane} = (\bar{1}\bar{1}1)$$

Figure 44. Dislocations in Fig. 43(b) viewed using various diffraction conditions: (a) B ~011 and **g** = $\bar{2}00$, (b) B ~112 and **g** = $11\bar{1}$, (c) B ~011 and **g** = $\bar{1}11$, and (d) B~001 and **g** = 020.

(a)

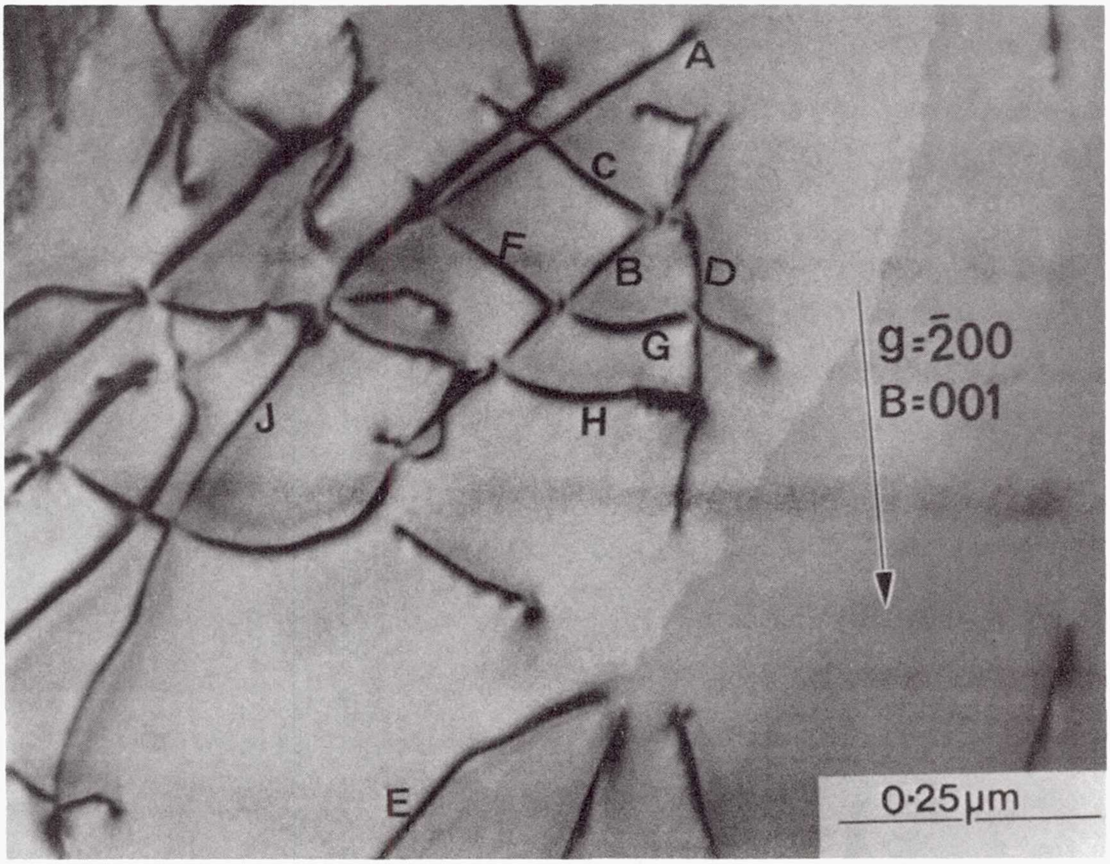

(b)

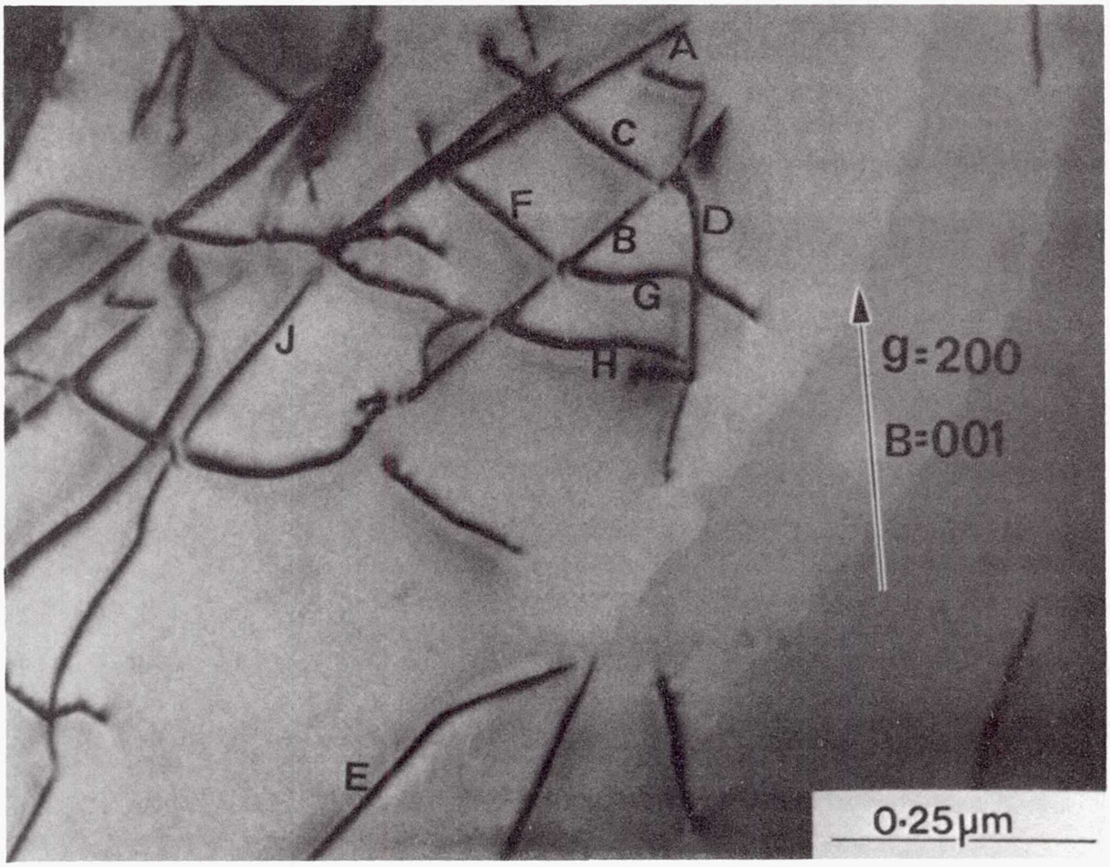

(c)

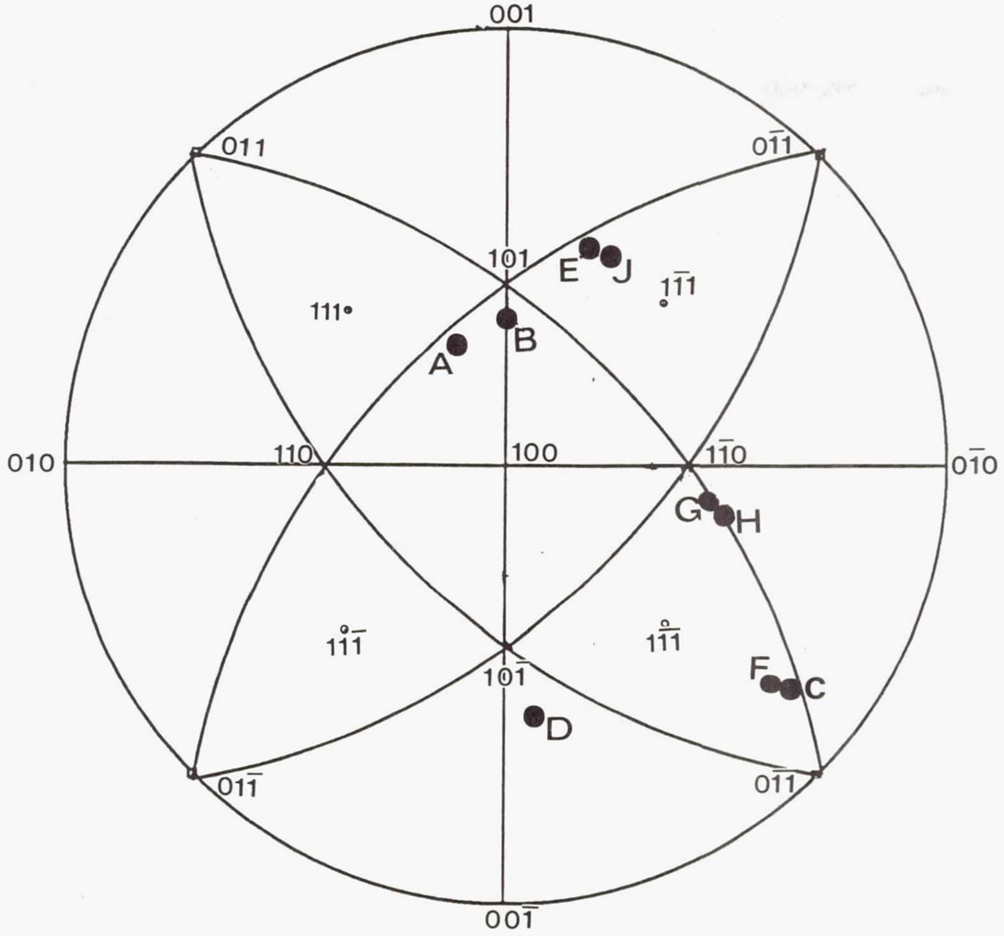

Tensile specimen deformed (1.3% plastic strain) at 623K

Dislocation	Burgers Vector $\vec{b}$	Slip plane(s)
A	$a_0[1\bar{1}0]$	$(11\bar{1})$
B	$a_0[1\bar{1}0]$	$(11\bar{1})$; -- (010) is not allowed
C	$a_0[110]$	$(1\bar{1}\bar{1})$
D	$a_0[10\bar{1}]$	(111), (010)
E	$a_0[1\bar{1}0]$	$(11\bar{1})$
F	$a_0[110]$	$(1\bar{1}\bar{1})$
G	$a_0[110]$	$(\bar{1}11)$
H	$a_0[110]$	$(\bar{1}11)$
J	$a_0[1\bar{1}0]$	$(\bar{1}\bar{1}1)$

Figure 45. Analysis of a dislocation network in the tensile specimen deformed at 623K: a) B ~001 and g = $\bar{2}00$, (b) B ~001 and g = 200, and (c) stereographic projection showing the line directions and slip systems for these dislocations.

(a)

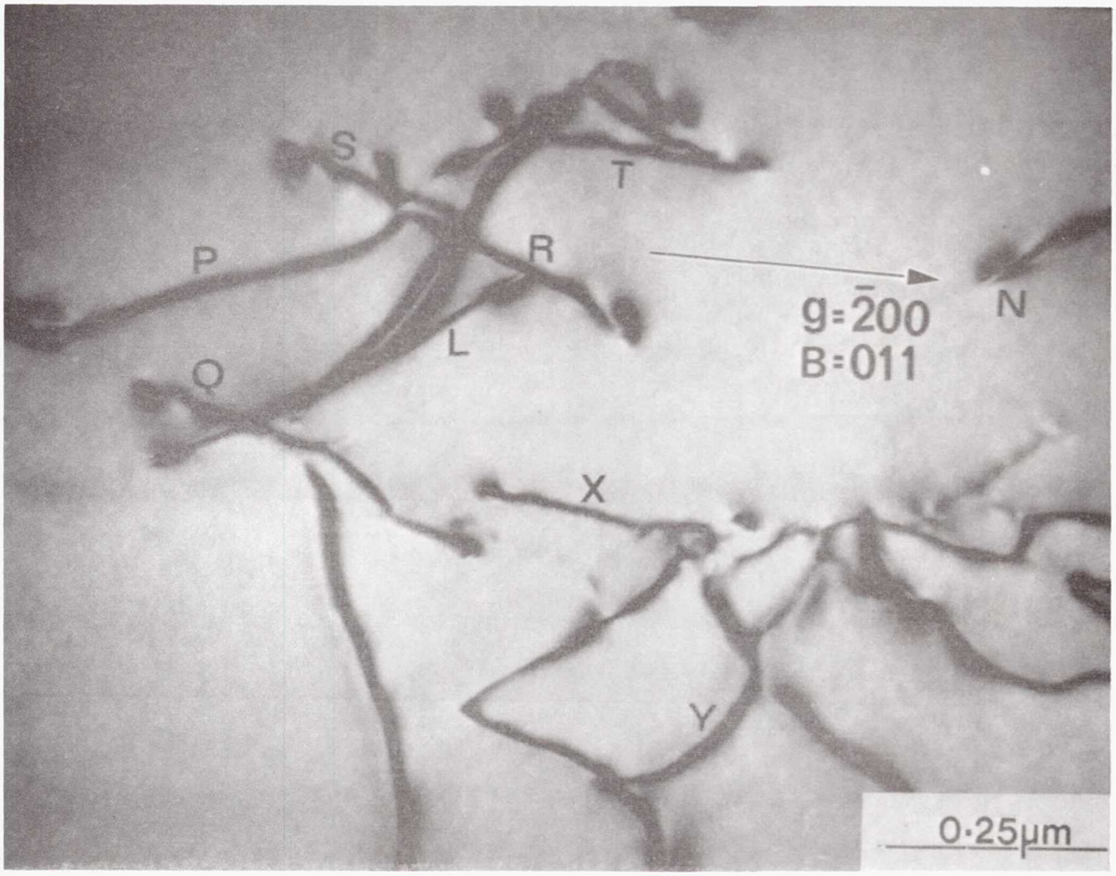
S
T
P
R
g=$\bar{2}$00
B=011
N
L
Q
X
Y
0·25μm

(b)

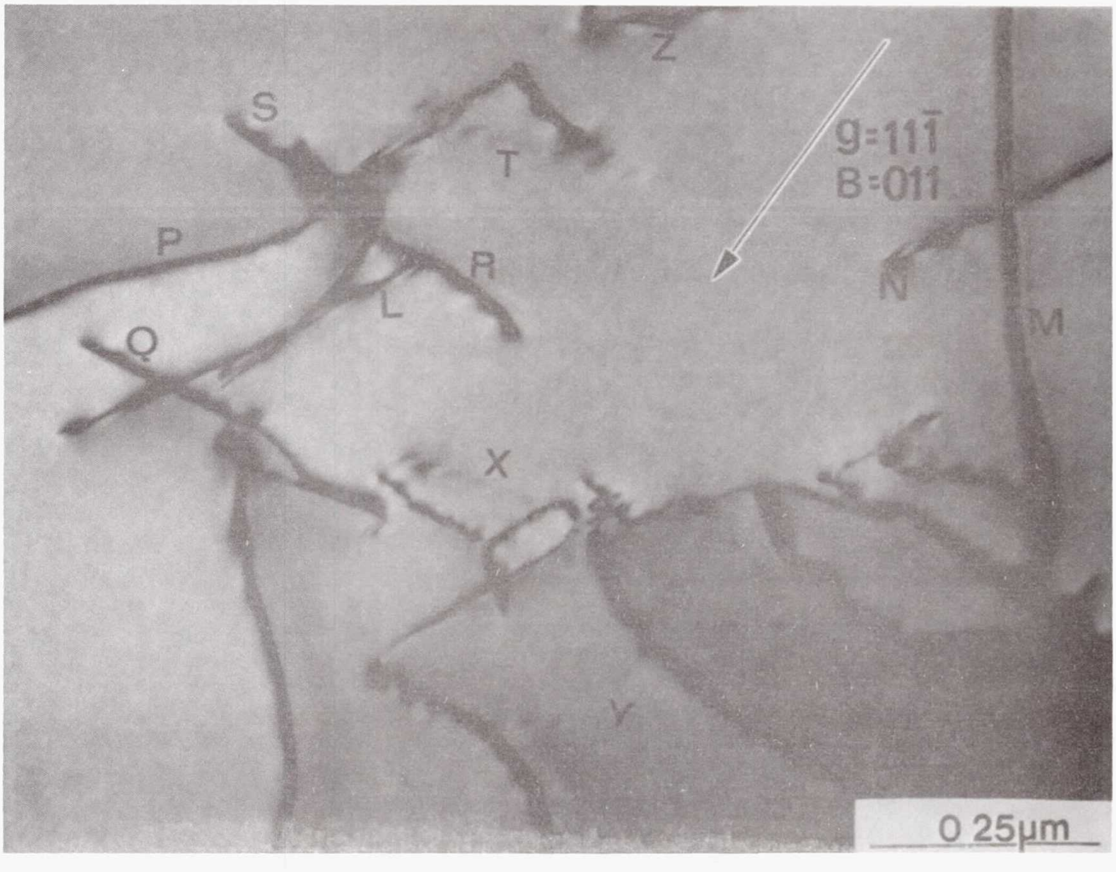
Z
S
T
g=11$\bar{1}$
B=011
P
R
L
N
M
Q
X
Y
0 25μm

(c)

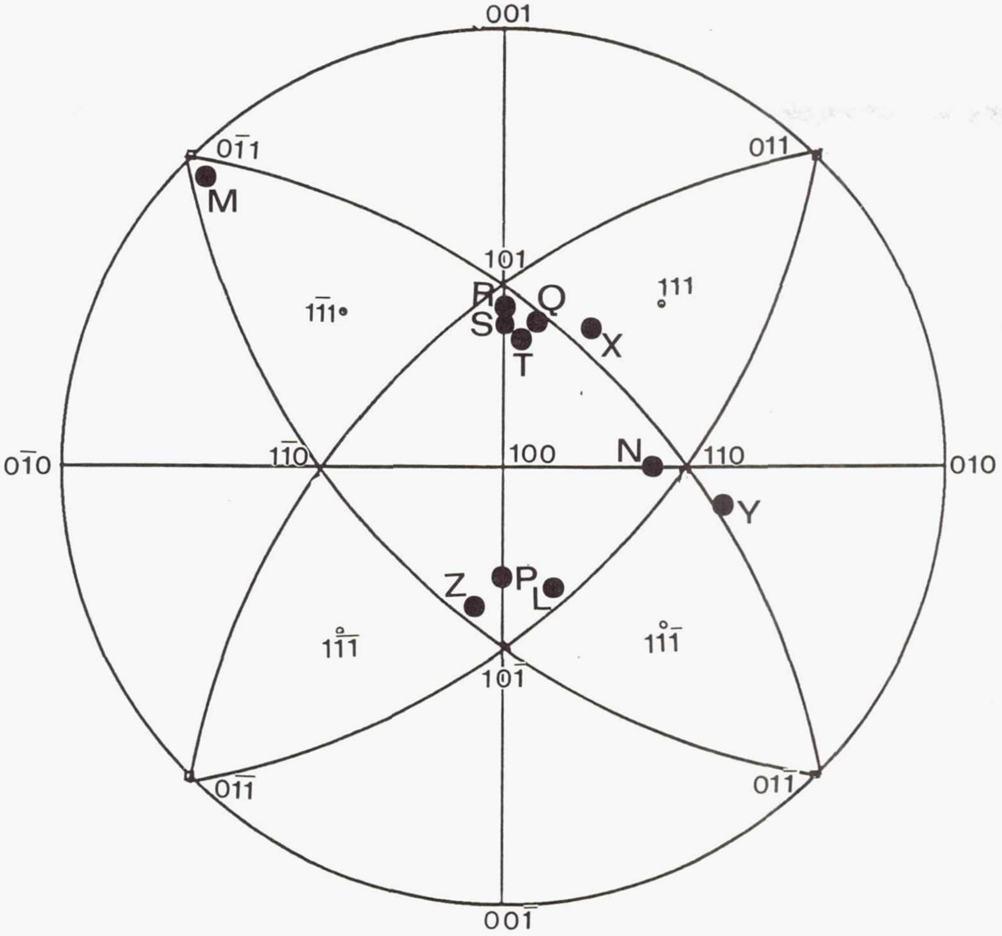

Tensile specimen deformed (1.2% plastic strain) at 923K

Dislocation	Burgers Vector $\vec{b}$	Slip plane(s)
L	$a_0[110]$	$(1\bar{1}1)$
M	$a_0[10\bar{1}]$	(111)
N	$a_0[110]$	$(1\bar{1}1)$, (001), $(1\bar{1}\bar{1})$
P	$a_0[10\bar{1}]$	(010)
Q	$a_0[110]$	$(1\bar{1}\bar{1})$
R, S	$a_0[110]$	$(1\bar{1}\bar{1})$
T	$a_0[101]$	(010)
X	$a_0[101]$	$(1\bar{1}\bar{1})$
Y	$a_0[101]$	$(1\bar{1}\bar{1})$
Z	$a_0[10\bar{1}]$	(111), (010)

Figure 46. Analysis of a dislocation network in the tensile specimen deformed at 923K: a) B ~011 and g = $\bar{2}00$, (b) B ~011 and g = $11\bar{1}$, and (c) stereographic projection showing the line directions and slip systems for these dislocations.

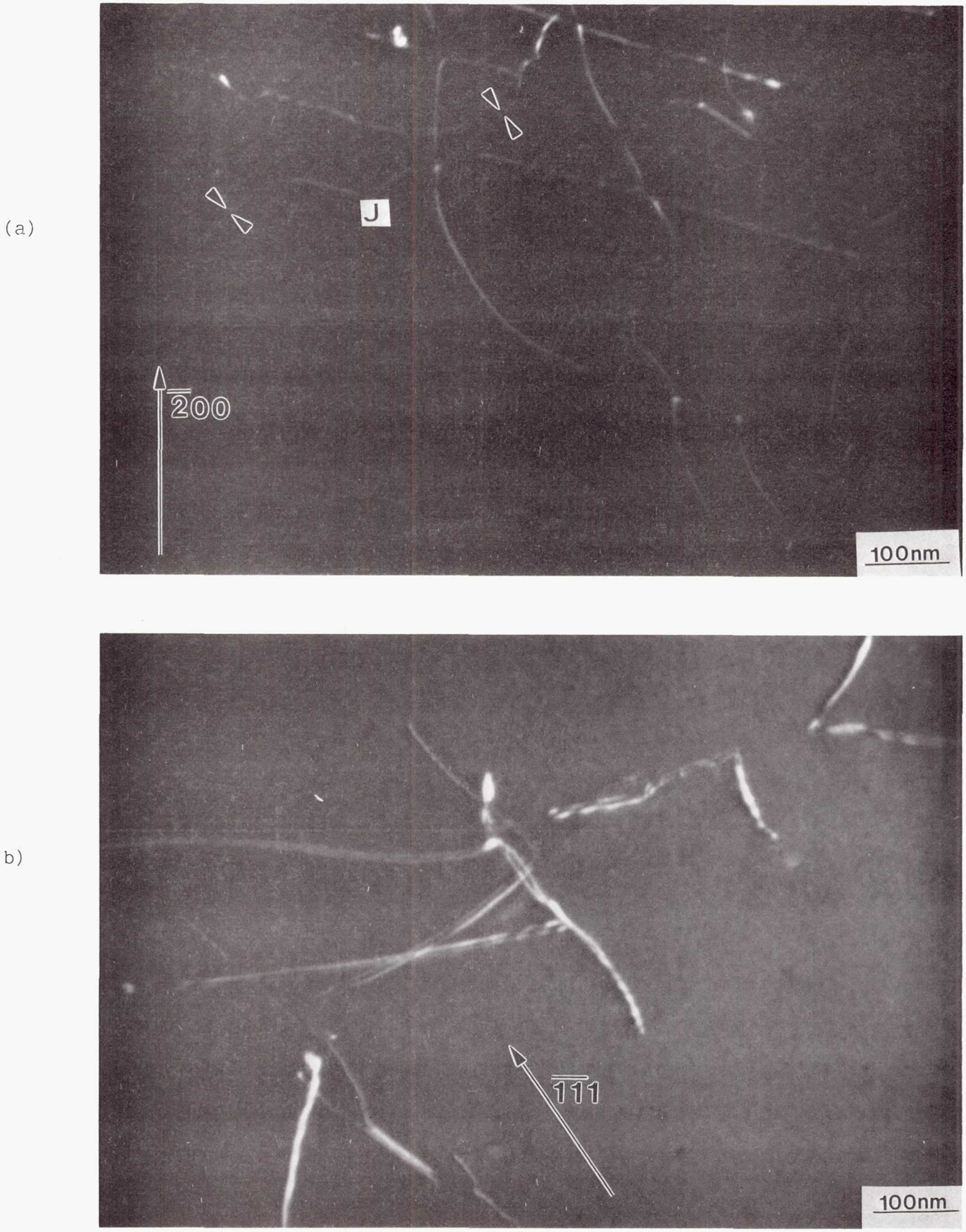

Figure 47. Weak-beam micrographs of dislocations in deformed tensile specimens: (a) at 623K (same network as in Fig. 45), and (b) at 923K (same network as in Fig. 46). In both cases, B ~011.

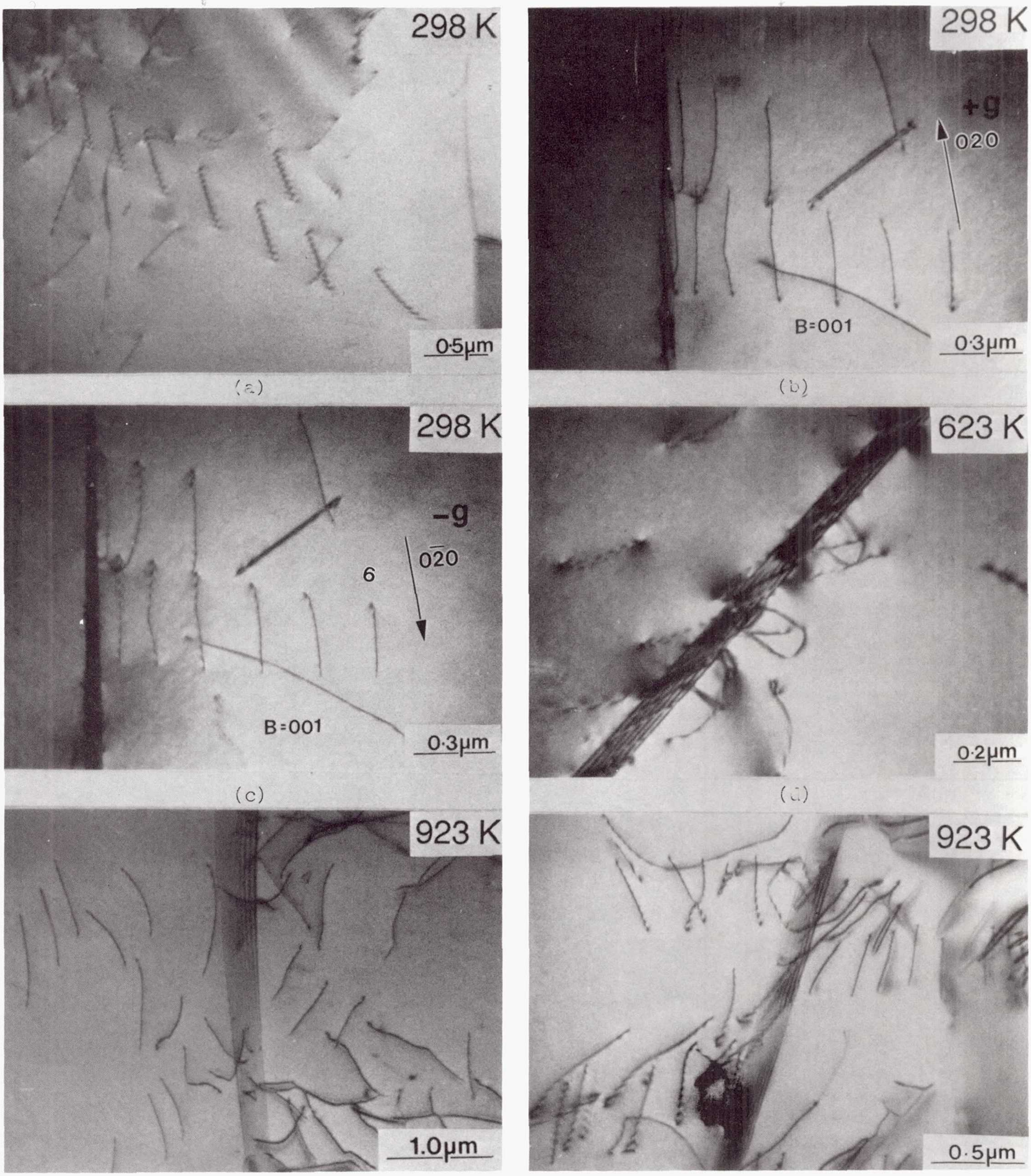

(a) (b)

(c) (d)

(e) (f)

Figure 48. Dislocations-grain boundary interactions in deformed tensile specimens: (a)-(c) 298K, (d) 623K, and (e,f) 923K.

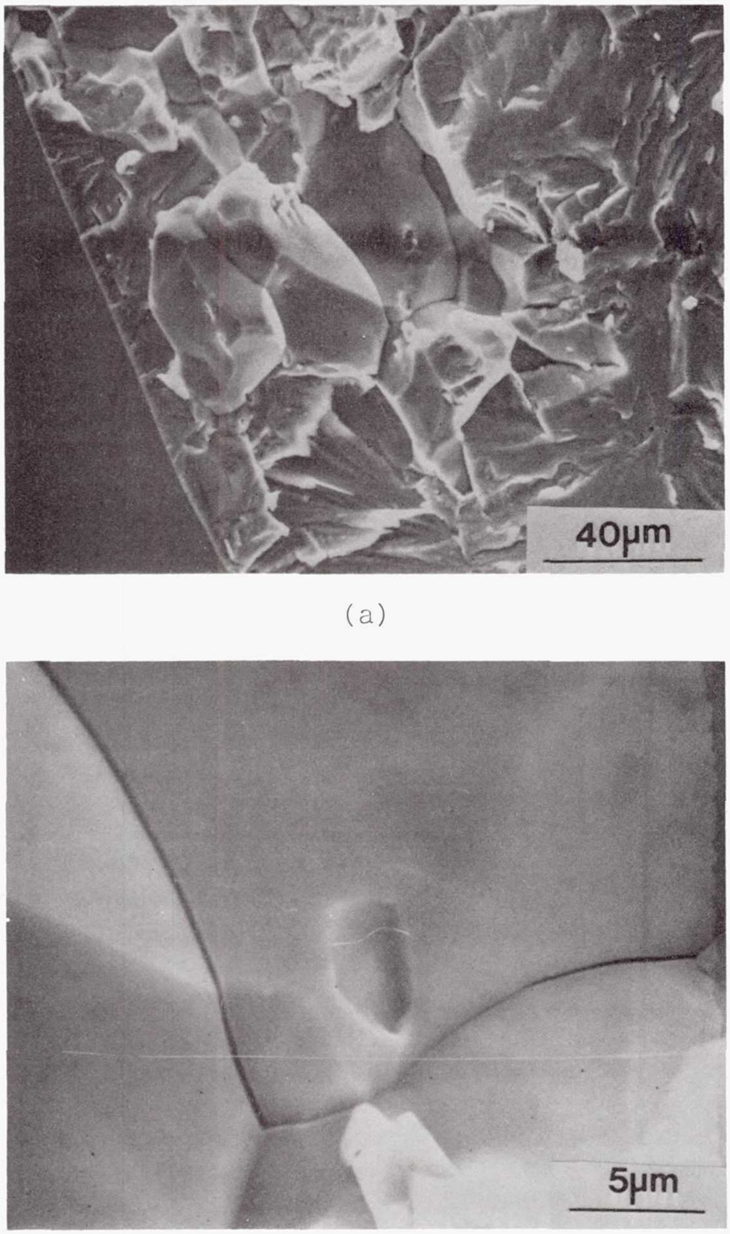

(a)

(b)

Figure 49. Fracture surface of the 437K tensile specimen: (a) grain-boundary failure at the circumference and (b) secondary grain-boundary cracking.

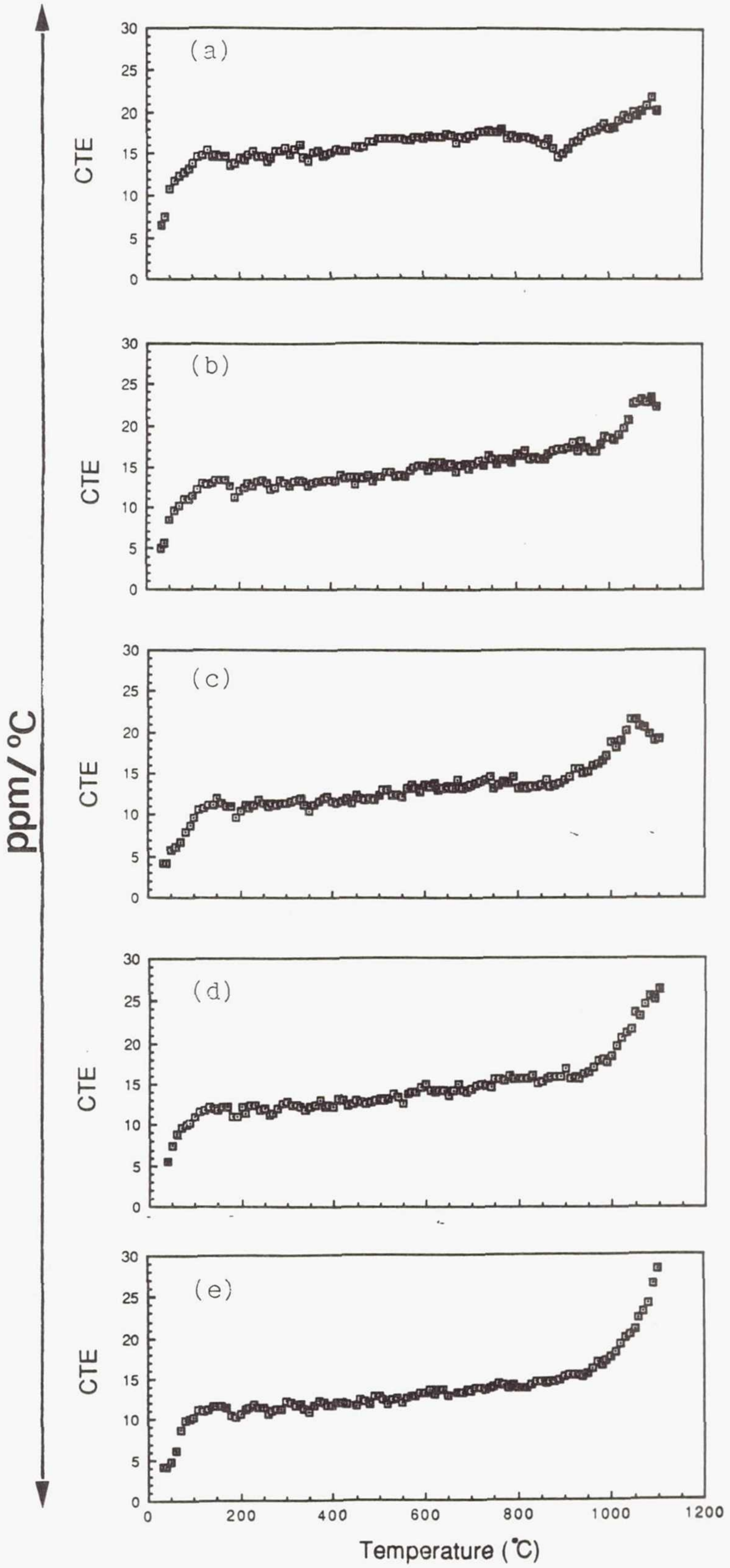

Figure 50. The change in CTE with temperature in the range 300K - 1373K for (a) $Al_{66}Ti_{25}Mn_9$, (b) $Al_{22}Ti_8Fe_3$ + 2Nb, (c) $Al_{22}Ti_8Fe_3$ + 2Nb + 20 vol.% TiB_2, (d) $Al_{22}Ti_8Fe_3$ + 10 vol.% TiB_2, and (e) $Al_{22}Ti_8Fe_3$ + 20 vol.% TiB_2.

NASA
National Aeronautics and
Space Administration

Report Documentation Page

1. Report No. NASA TM-103724	2. Government Accession No.	3. Recipient's Catalog No.

4. *Title and Subtitle*

Low-Density, High-Strength Intermetallic Matrix Composites by XD^{TM} Synthesis

5. Report Date

January 1991

6. Performing Organization Code

7. Author(s)

K.S. Kumar, M.S. DiPietro, S.A. Brown, and J.D. Whittenberger

8. Performing Organization Report No.

E-5955

10. Work Unit No.

510-01-01

9. Performing Organization Name and Address

National Aeronautics and Space Administration
Lewis Research Center
Cleveland, Ohio 44135-3191

11. Contract or Grant No.

13. Type of Report and Period Covered

Technical Memorandum

12. Sponsoring Agency Name and Address

National Aeronautics and Space Administration
Washington, D.C. 20546-0001

14. Sponsoring Agency Code

15. Supplementary Notes

K.S. Kumar, M.S. DiPietro, and S.A. Brown, Martin Marietta Corporation, Baltimore, Maryland 21227 (work funded under NASA Contract NAS3-25787); J.D. Whittenberger, NASA Lewis Research Center. Responsible person, K.S. Kumar, (301) 247-0700.

16. Abstract

Over the past year, a feasibility study was conducted to evaluate the potential of particulate composites based on low-density, $L1_2$ trialuminide matrices for high-temperature applications. The compounds evaluated included $Al_{22}Fe_3Ti_8$ (as a multiphase matrix), $Al_{67}Ti_{25}Cr_8$, and $Al_{66}Ti_{25}Mn_9$. The reinforcement consisted of $\sim 1\ \mu m$ TiB_2 particulates; the composites were produced by the XD^{TM} process. The monolithic and 5 vol.% TiB_2 composites were processed by both ingot and powder metallurgy approaches, but composites with higher volume fractions of reinforcements were processed only by powder metallurgy techniques since their melt viscosity was too high for casting. Powder metallurgy techniques were used for composites with up to 20 vol.% reinforcement. Microstructural characterization and mechanical testing were performed on the powder processed material in the hot-pressed and HIP'ed condition. The castings were sectioned and isothermally forged into pancakes. All the materials were tested in compression as a function of temperature, and at high temperatures (900-1200K) as a function of strain rate. In addition, three-point bend tests were conducted on the ingot- and powder-processed material as a function of temperature. A limited number of uniaxial tensile tests were performed as a function of temperature on the monolithic $Al_{66}Ti_{25}Mn_9$ forging. Microstructural examination (by optical, scanning, and transmission electron microscopy) of material in the hot-pressed or forged condition, and after deformation, revealed that the Mn-based $L1_2$ compound has the best low-temperature ductility but low strength and likely low oxidation resistance; the Fe-based multiphase monolithic material has high strength up to 1000K, but is brittle; and the Cr-based $L1_2$ compound is similar in strength to the Mn-based material, likely has good oxidation resistance, but lacks ambient ductility. The addition of TiB_2 particulates to these compounds significantly enhances room- and warm-temperature strength, although the composites are weaker than the monolithic material in the use-temperature range at strain rates of $\sim 10^{-4}s^{-1}$. At slow strain rates ($\sim 10^{-7}s^{-1}$), however, the composites are marginally stronger than their monolithic counterparts. It was also shown that minor quaternary substitutions (2 at.% Nb or 2 at.% Mn) in the Fe-based compound do not significantly influence the strength of the ternary multiphase compound.

17. Key Words (Suggested by Author(s)) $L1_2$ trialuminides; Forging; Powder metallurgy; Particulate composites; Microstructure; Mechanical behavior; XD^{TM} synthesis; Deformation; High temperature	18. Distribution Statement Unclassified – Unlimited Subject Category 24

19. *Security Classif. (of this report)* Unclassified	20. Security Classif. (of this page) Unclassified	21. No. of pages 100	22. Price* A05

NASA FORM 1626 OCT 86

*For sale by the National Technical Information Service, Springfield, Virginia 22161